UNIVERSITÀ
DEGLI STUDI
DI PADOVA

Università degli Studi di Padova
Dipartimento di Fisica ed Astronomia
Scuola di Dottorato di Ricerca in Fisica
Ciclo XXIX

Study of semitauonic and semimuonic $\Lambda_b^0 \to \Lambda_c^{*+} l^- \bar{\nu}_l$ decays at LHCb

Director of the Doctoral School: **Prof. Gianguido Dall'Agata**

Supervisor: **Dott. Marcello Rotondo**
Co-Supervisor: **Prof. Gabriele Simi**

Author: **Anna Lupato**

To my mother

Abstract

In this thesis the $\Lambda_b^0 \to \Lambda_c^{*+}\tau^-\bar{\nu}_\tau$ and $\Lambda_b^0 \to \Lambda_c^{*+}\mu^-\bar{\nu}_\mu$ decays have been investigated. In particular, the first measurement of the ratio $R(\Lambda_c^*) = \mathcal{B}(\Lambda_b^0 \to \Lambda_c^{*+}\tau^-\bar{\nu}_\tau)/\mathcal{B}(\Lambda_b^0 \to \Lambda_c^{*+}\mu^-\bar{\nu}_\mu)$ has been performed using a sample of LHC pp collision data corresponding to 2 fb^{-1} of integrated luminosity, recorded by the LHCb detector in the 2012. Only the excited state $\Lambda_c^+(2625)$ have been reconstructed, particularly in $\Lambda_c^{*+} \to \Lambda_c^+(\to pK^-\pi^+)\pi^+\pi^-$ decay mode and only the muonic decays of τ are considered, $\tau^- \to \mu^-\bar{\nu}_\mu\nu_\tau$.
This measurement is of great interest in order to confirm or disprove the discrepancies with respect to SM predictions found in analogue measurement performed on mesonic decays. Moreover it is the first measurement focused on baryonic decays.
The ratio is measured by fitting the output of the neural network distribution of the data based on the missing mass square, the energy of the lepton in the Λ_b^0 rest frame and a Fisher discriminant output build using the Λ_b^0 decay vertex informations. The fit has been performed simultaneously on transferred momentum and isolations bins. The last variable allows to select a sample enriched of double charmed Λ_b^0 decays.
The $R(\Lambda_c(2625))$ is measured to be consistent with the Standard Model expectation ($R_{exp}(\Lambda_c(2625)) = 0.151 \pm 0.014$) and equal to

$$R(\Lambda_c(2625)) = 0.238 \pm 0.108(stat) \pm 0.058(syst)$$

However, at the moment, it is dominated by statistical error. The run II LHC data (at least 5 fb^{-1} of integrated luminosity) will allow to have a statistical error competitive with the systematic one, assuming to perform the analysis using the same strategy.
Moreover, by using the fit result, the differential decay rate $(1/\Gamma)d\Gamma/dq^2(\Lambda_b \to$

$\Lambda_c^* \mu \bar{\nu}_\mu$), considering the unfolding of the raw spectrum for the q^2 resolution and the selection efficiency, has been determined.
Finally, it is presented a new method to determine the b-hadron momentum in a semileptonic decays of this one at a hadron collider. In fact, in this environment, due to the presence of one or more neutrinos, to unknown parton-parton collision energy and the busy hadronic environment, is not possible to reconstruct the b-hadron momentum in the laboratory rest frame using final particles. As a consequence, the decays kinematics can be solved only up to a quadratic ambiguity. To solve this problem in this thesis is also presented a new method, based on a multivariate regression algorithm developed exploits the informations that can be extracted by b-hadron flight vectors to infer its momentum. The improved resolutions may be exploited to measure the differential decay width $d\Gamma(H_b \to H \mu \bar{\nu}_\mu)/dq^2$ with high precision because of the reduced migrations between the q^2 bins.

Contents

Introduction

It is known that the Standard Model is not the ultimate description of elementary particle dynamics, but an effective field theory valid to the energy scale explored so far. Finding and identifying hints of New Physics in the quark flavour dynamics still represents a great challenge at the colliders. There are indeed already available evidences of phenomena that cannot be described within the Standard Model, like for instance neutrino oscillations. CP violation, required to explain the matter-antimatter asymmetry of the Universe, has been discovered and measured in the K and B system, in accordance to the Standard Model prediction. However, it is insufficient to explain the magnitude of the baryon asymmetry of the Universe, and therefore, further sources of CP violation must exist. It is possible that this new sources could be found in the lepton sector, or indeed in an extended gauge sector.

In the Standard Model, the couplings of the gauge bosons to the leptons are independent of the lepton flavour and then, the branching fractions of e, μ and τ can differ only by phase space and helicity-suppressed contributions. The Lepton Flavor Universality is enforced in the SM by construction and therefore any violation of lepton universality would be a clear sign of physics beyond the SM. Existing hints of non universality have already been observed in Electroweak Penguin processes ($B^{\pm} \rightarrow K^{\pm} l^+ l^-$ and recently $B^0 \rightarrow K^{*0} l^+ l^-$) and in the semi-tauonic B meson decays ($R(D^*) = \mathcal{B}(\bar{B}^0 \rightarrow D^{*+} \tau^- \bar{\nu}_\tau)/\mathcal{B}(\bar{B}^0 \rightarrow D^{*+} \mu^- \bar{\nu}_\mu)$. The semitauonic decays, in particular, are sensitive to contributions from non-Standard-Model particles that preferentially couple to the third generation of fermions. For example Higgs-like charges scalars, could contribute to these decays together

with the usual Standard Model W-emission amplitude and increase the semitauonic decays. The most recent HFAG combination, considering B factories and LHCb results of R(D) and R(D*) measurements, is 3.9σ from SM expectation. Several test has been performed using the B mesons decays and many NP scenarios have been hypothesized to explain the discrepancies with respect to SM predictions. The study of the analogous observables in the baryonic sector is crucial to both, confirm or disprove the discrepancy with the SM in completely different b-hadron, and constrain the possible source of new physics because of the different spin structure compared with the usual meson B decays. In particular, in this thesis, the Λ_b^0 semimuonic and semitauonic decays which involves excited Λ_c particles are studied and a measurement of the ratio $R(\Lambda_c^*) = \mathcal{B}(\Lambda_b^0 \to \Lambda_c^{*+}\tau^-\bar{\nu}_\tau)/\mathcal{B}(\Lambda_b^0 \to \Lambda_c^{*+}\mu^-\bar{\nu}_\mu)$ is presented. The first angular excited Λ_c states form a doublet, named $\Lambda_c(2595)$ and $\Lambda_c(2625)$, of well separated narrow states. Both decay in $\Lambda_c\pi^+\pi^-$ mode with a branching fraction of about 70%. The presence of the two further charged tracks make their reconstruction easy in LHCb. As first measurement of R in Λ_b^0 decays, it has been preferred to study the decay into exited states over the fundamental one, mainly because of the smaller contamination from the decays of other higher masses states. Moreover, with huge statistics, the decay of excited states allows to access further kinematics observables besides the ratio R. The measurement based on Λ_c ground state semileptonic will be an interesting following measurement.

The measurement is performed using a sample of pp collision data corresponding to 2 fb^{-1} of integrated luminosity, recorded by the LHCb detector in the 2012. Only muonic decays of τ are considered, $\tau^- \to \mu^-\bar{\nu}_\mu\nu_\tau$, the $\Lambda_c^+(2595)$ and $\Lambda_c^+(2625)$ baryons are reconstructed in the $\Lambda_c^{*+} \to \Lambda_c^+\pi^+\pi^-$ decay mode, and finally the Λ_c^+ is built according to its decay mode $\Lambda_c^+ \to pK^-\pi^+$. The $\Lambda_b^0 \to \Lambda_c^{*+}\mu^-\bar{\nu}_\mu$ channel is the largest physical background to the $\Lambda_b^0 \to \Lambda_c^{*+}\tau^-\bar{\nu}_\tau$ decays and it is also the normalization channel. They are extracted simultaneously from a fit, and the observables R is directly determined. The Form Factors of the $\Lambda_b^0 \to \Lambda_c^{*+}$ transitions have never been measured before, so both the signal and the normalization yields are

extracted in bins of the transferred momentum (q^2). In this way the impact of the Form Factors knowledge on the measurement of R is much reduced, and it is possible to extract informations about their shapes.
The study of b-hadron semileptonic decays at hadron colliders suffers of problems in the determination of the full decay kinematics, because the presence of the neutrinos and the large fluctuation in the parton-parton collision energy, does not allow to determine the b-hadron momentum event by event. In the LHCb acceptance region, thanks to the large forward boost, the b-hadrons fly on average by about 1cm. From the flight direction and the hypothesis of single neutrino missing, the b-hadron momentum for semileptonic decays, can be reconstructed up to a two-fold ambiguity. A multivariate algorithm that uses informations unrelated to the decay mode, has been developed.

Chapter 1

Theory of flavour violation in semileptonic decays

1.1 The Standard Model

The Standard Model describes the elementary particles and their interactions. Elementary particles are divided in two sets, fermions which have half-integer spin, and bosons, which have integer spin. The elementary fermions are quarks and leptons. They form the building blocks of matter. Bosons are the force-carriers, responsible for the interactions between the fermions. The Standard Model describes three among four fundamental interactions existing in nature: the electromagnetic, the weak and the strong interaction. The fourth and weakest force in nature, gravitation, is not included in the Standard Model. The fermions can be divided in three generations of increasing mass, with one pair of quarks (u,c,t,d,s,b) and one pair of leptons (e,v_e,μ,v_μ,τ,v_τ) in each of them:

$$\begin{pmatrix} e \\ v_e \end{pmatrix} \begin{pmatrix} \mu \\ v_\mu \end{pmatrix} \begin{pmatrix} \tau \\ v_\tau \end{pmatrix} \begin{pmatrix} u \\ d \end{pmatrix} \begin{pmatrix} c \\ s \end{pmatrix} \begin{pmatrix} t \\ b \end{pmatrix}$$

For each particle, there is an antiparticle characterized by same mass, spin and time decay but with every other quantum number different.

The electromagnetic force acts on all charged particles through the exchange of a (massless) photon. The weak force acts on all fermions through the exchange of a massive $W^\pm$ or Z^0. The strong force acts on quarks exchanging a gluon with another quark. Quarks are provided of a color charge

which can be exchanged when interacting with other quarks.

The Standard Model is a relativistic quantum field theory based on the local gauge invariance principle of the group

$$SU(3)_{color} \times SU(2)_L \times U(1)_Y$$

Here, Y and C represent the weak hyper-charge and the color charge generators, respectively, and L refers to the left-handed projection of chirality.

Moreover, besides the invariance for gauge transformations, SM, as every other quantum field theory, has to be invariant under the CPT transformation.

The charge conjugation operator C, interchanges particle and antiparticle. The parity operator P inverts the sign of spatial coordinates and then reverses the handedness, i.e the projection of chirality. The time-reversal operator T interchanges all directions of motion, including spin.

CPT conservation guarantees that mass, lifetime and magnetic moment of particle and antiparticle are equal.

In the SM the left-handed leptons and quarks are inserted as $SU(2)_L$ doublets, and the corresponding right-handed fields are inserted as $SU(2)_R$ singlets (Table 1.1), which means that the right-handed particles in the SM do not interact weakly. This description entails the parity violation of the weak interction, as discovered in Wu experiment [1].

Table 1.1: Left-handed doublets and right-handed singlets in the SM for the first (top), second (middle) and third (bottom) generations. The corresponding antiparticles are omitted for simplicity. Note the absence of right-handed neutrinos in the SM.

$\binom{\nu_e}{e^-}_L$	$\binom{u}{d}_L$	e^-_R	u_R	d_R
$\binom{\nu_\mu}{\mu^-}_L$	$\binom{c}{s}_L$	μ^-_R	c_R	s_R
$\binom{\nu_\tau}{\tau^-}_L$	$\binom{t}{b}_L$	τ^-_R	t_R	b_R

In the Standard Model the weak and electromagnetic forces arise from a $SU(2)_L \times U(1)_Y$ gauge symmetry of the Lagrangian which can be written as:

$$\mathcal{L}_{EW} = \bar{L}\ \gamma^\mu(i\partial_\mu - g^{'}\frac{1}{2}YB_\mu - g\frac{1}{2}\vec{\tau}\vec{W}_\mu\ )L + \bar{R}\ \gamma^\mu(i\partial_\mu - g^{'}\frac{1}{2}YB_\mu)R \quad (1.1)$$

where L denotes left-handed doublets and R the right-handed singlets of Table 1.1, B_μ is the U(1) gauge field, Y is the weak hyper-charge, $\vec{W}_\mu$ is the three-component SU(2) gauge field, $\vec{\tau}$ are the Pauli matrices, g and g' are the coupling constants.

The Lagrangian (1.1) does not include mass terms for bosons, fermions and quarks. Explicit fermion and quark mass terms ($m\bar{\psi}\,\psi$) are not permitted since the left-handed and right-handed components of the fermion and quarks fields transform differently under SU(2):

$$\begin{aligned} L &\xrightarrow{SU(2)} L' = e^{-i\frac{\vec{\theta}\cdot\vec{\tau}}{2}} L \\ R &\xrightarrow{SU(2)} R' = R \end{aligned} \tag{1.2}$$

Also gauge bosons mass terms are not invariant under gauge transformation since they have the form $\frac{1}{2}m^2 B^\mu B_\mu$ (where B is one of the quadrivectorial fields and m the mass). To generate particle masses it is necessary to spontaneously break the gauge symmetry. This mechanism is called Higgs mechanism.

The fermions acquire mass through the introduction of a scalar complex SU(2) doublet ϕ, the Higgs field, and its Hermitian conjugate [2]. These produce gauge invariant Yukawa interaction terms when the Higgs field acquire a vacuum expectation value ν, giving the fermions masses.

The Yukawa term for the lepton fields is

$$\mathcal{L}_{l\_mass} = \sum_{i=1}^{3} g_e^i \bar{e}_L^i \begin{pmatrix} \phi^+ \\ \phi^0 \end{pmatrix} e_R^i \tag{1.3}$$

where e_L are the three left-handed lepton doublets, e_R the three right handed leptons singlets and g_e^i the coupling constant. After spontaneous symmetry breaking :

$$\begin{aligned} \phi^+ &= 0 \\ \phi^0 &= \frac{1}{2}(\nu + H) \end{aligned}$$

$\mathcal{L}_{l\_mass}$ becomes:

$$\mathcal{L}_{l\_mass} = \sum_{i=1}^{3} \frac{g_e^i \nu}{\sqrt{2}} \bar{e}_L e_R^i + \frac{g_e^i}{\sqrt{2}} \bar{e}_L e_R^i H \tag{1.4}$$

Then the mass of e^i is equal to

$$m_{e^i} = \frac{g_e^i \nu}{\sqrt{2}} \tag{1.5}$$

The Yukawa term for the quarks fields is

$$\mathcal{L}_{q\_mass} = \sum_{i,j=1}^{3} Y_{ij} \bar{q}^{\ i}_{L} \begin{pmatrix} \phi^{0*} \\ -\phi^{-} \end{pmatrix} d_R^j + Y'_{ij} \bar{q}^{\ i}_{L} \begin{pmatrix} \phi^{+} \\ \phi^{0} \end{pmatrix} d_R^j + h.c \tag{1.6}$$

where q_L are the three left-handed quark doublets, d_R and u_R are the three right-handed down-type and up-type quark singlets, Y_{ij} and Y'_{ij} are the 3×3 Yukawa coupling matrix and its Hermitian conjugate. After spontaneous symmetry breaking :

$$\phi^+ = 0$$
$$\phi^0 = \frac{1}{2}(\nu + H)$$

$\mathcal{L}_{q\_mass}$ becomes:

$$\mathcal{L}_{q_m ass} = -\sum_{i,j=1}^{3} (m_{ij}^u \bar{u}^{\ i}_{L} u_{jR} + m_{ij}^d \bar{d}^{\ i}_{L} d_{jR} + h.c)[1 + \frac{1}{\nu} H] \tag{1.7}$$

where m_{ij}^u and m_{ij}^d are 3×3 matrices defined as :

$$m_{ij}^u = -\frac{\nu}{\sqrt{2}} Y_{ij}$$
$$m_{ij}^d = -\frac{\nu}{\sqrt{2}} Y'^{\ ij}$$

Physical fields are eigenstates of the mass matrix, so $m_{ij}^{u,d}$ must be diagonalized:

$$u_L^{phys} = U_L \begin{pmatrix} u_L \\ c_L \\ t_L \end{pmatrix}$$

$$d_L^{phys} = D_L \begin{pmatrix} d_L \\ s_L \\ b_L \end{pmatrix}$$

where U_L and D_L are unitary matrices. Similar relations hold for the R-handed quarks.

These unitary matrices allow us to find the relation between physical (eigenstates of mass) and non-physical (fields with definite transformation properties under gauge group) fields.

Thus, the charged current Lagrangian term becomes:

$$\begin{aligned}\mathcal{L}_{cc} &= -\frac{g}{2\sqrt{2}}(W^+_\mu \bar{u}_{\ L}\gamma^\mu d_L + h.c) = \\ &= -\frac{g}{2\sqrt{2}}(W^+_\mu \bar{u}^{\ phys}_{L}\gamma^\mu U_L D^\dagger_L\, d^{phys}_L + h.c) = \\ &= -\frac{g}{2\sqrt{2}}(W^+_\mu \bar{u}^{\ phys}_{L}\gamma^\mu V_{CKM} d^{phys}_L + h.c) = \\ &= W^+_\mu J^\mu_{cc} + h.c.\end{aligned} \tag{1.8}$$

where J^μ_{cc} is the charged current and $V_{CKM}d^{phys}_L = d^{EW}_L$. Therefore, the weak eigenstates are superpositions of the physical eigenstates and are related by the Cabibbo-Kobayashi-Maskawa (CKM) matrix [3] [4]:

$$\begin{pmatrix} d_{EW} \\ s_{EW} \\ b_{EW} \end{pmatrix} = V_{CKM} \begin{pmatrix} d \\ s \\ b \end{pmatrix}$$

The structure of the charged-current weak interaction therefore allows mixing between the different quark generations and is referred to as flavour changing. V_{CKM} is a 3×3 unitary matrix which may be written as

$$V_{CKM} = U_L D^\dagger_L = \begin{pmatrix} V_{ud} & V_{us} & V_{ub} \\ V_{cd} & V_{cs} & V_{cb} \\ V_{td} & V_{ts} & V_{tb} \end{pmatrix}$$

where each (complex) element is proportional to the amplitude for a particular weak transition. In general, a 3×3 complex matrix has 18 independent parameters (nine complex numbers, each with a real and imaginary part). The unitarity of the CKM matrix reduces this to nine and a further five are absorbed by relative phase changes between the quark fields. This leaves four independent parameters: three mixing angles and a complex phase. The

fact that elements of the CKM matrix may be complex allows Charge-Parity (CP) violation to occur within the framework of the Standard Model.

One of the possible parameterizations of the CKM matrix is

$$V_{CKM} = \begin{pmatrix} c_{12}c_{13} & s_{12}c_{13} & s_{13}e^{-i\delta} \\ -s_{12}c_{23} - c_{12}s_{23}s_{13}e^{i\delta} & c_{12}c_{23} - s_{12}s_{23}s_{13}e^{i\delta} & s_{23}c_{13} \\ s_{12}s_{23} - c_{12}c_{23}s_{13}e^{i\delta} & -c_{12}s_{23} - s_{12}c_{23}s_{13}e^{i\delta} & c_{23}c_{13} \end{pmatrix} \quad (1.9)$$

where $c_{ij} = \cos\theta_{ij}$ and $s_{ij} = \sin\theta_{ij}$ and δ is the phase responsible for all CP-violating phenomena in the Standard Model.

It is known experimentally that $s_{13} << s_{23} << s_{12} << 1$, that $s_{12} \approx 0.22$ and, defining $s_{12} = \lambda$, that the CKM elements are of the following order of magnitude with respect to λ:

$$|V|_{CKM} \sim \begin{pmatrix} 1 & \lambda & \lambda^3 \\ \lambda & 1 & \lambda^2 \\ \lambda^3 & \lambda^2 & 1 \end{pmatrix} \quad (1.10)$$

Therefore, it is possible to redefine the four CKM parameters using the Wolfenstein [5] parametrization, based on a power series of λ:

$$\begin{aligned} s_{12} = \lambda &= \frac{|V_{us}|}{\sqrt{|V_{ud}|^2 + |V_{us}|^2}} \\ s_{23} = A\lambda^2 &= \lambda \left| \frac{V_{cb}}{V_{us}} \right| \\ s_{13}e^{i\delta} = V_{ub}^* &= A\lambda^3(\rho + i\eta) \\ with \;\; \rho \;\; and \;\; \eta \;\; &\sim O(1) \end{aligned} \quad (1.11)$$

So the CKM matrix becomes:

$$|V|_{Wolfenstein} = \begin{pmatrix} 1 - \frac{\lambda^2}{2} + \frac{\lambda^4}{8} & \lambda & A\lambda^3(\bar{\rho} + i\bar{\eta}) \\ -\lambda + A\lambda^5(\frac{1}{2} - \bar{\rho} - i\bar{\eta}) & 1 - \frac{\lambda^2}{2} + \frac{\lambda^4}{8}(1 - 4A^2) & A\lambda^2 \\ A\lambda^3(1 - \bar{\rho} - i\bar{\eta}) & -A\lambda^2 + A\lambda^4(\frac{1}{2} - \bar{\rho} - i\bar{\eta}) & 1 + \frac{1}{2}A^2\lambda^4 \end{pmatrix} \quad (1.12)$$

where

$$\bar{\rho} = \rho(1 - \frac{\lambda^2}{2}) \qquad \bar{\eta} = \eta(1 - \frac{\lambda^2}{2}) \quad (1.13)$$

The unitarity of the CKM matrix imposes:

$$\sum_i V_{ij}V_{ik}^* = \delta_{jk} \qquad \sum_j V_{ij}V_{kj}^* = \delta_{ik} \tag{1.14}$$

The six vanishing combinations can be represented as triangles in the complex plane.The triangles obtained by applying the unitarity condition to neighboring columns are nearly degenerate.
According to the experimental measurements [6], the magnitude of CMK matrix elements are:

$$V_{CKM} = \begin{pmatrix} 0.97434^{+0.00011}_{-0.00012} & 0.22506 \pm 0.00050 & 0.00357 \pm 0.00015 \\ 0.22492 \pm 0.00050 & 0.97351 \pm 0.00013 & 0.04111 \pm 0.0013 \\ 0.00875^{+0.00032}_{-0.00033} & 0.0403 \pm 0.013 & 0.99915 \pm 0.00005 \end{pmatrix} \tag{1.15}$$

The transition between different quark families does not take place in the neutral currents. In fact, due to the unitarity of CKM matrix a fermion can interact only with its antiparticle or with an identical fermion. So the SM does not foresee Flavour-Changing Neutral Currents (FCNC) at tree-level [7].

Finally, in the Standard Model the strong interactions between quarks and gluons, explained by quantum chromodynamics theory, arise from a $SU(3)_{color}$ local gauge symmetry of the Lagrangian which can be written as:

$$\mathcal{L}_{QCD} = \sum_F \bar{\psi}_F(i\gamma^\mu\partial_\mu - g_s\gamma^\mu\frac{\lambda^C}{2}A_\mu^C - m_F)\psi_F - \frac{1}{4}A^{C\mu\nu}A_{\mu\nu}^C \tag{1.16}$$

where ψ_F is a triplet in the SU(3) space of quarks spinors of flavour F and mass m_F, A_μ^C the massless gluon fields with $C\ in[1,8]$, $A_{\mu\nu}^C$ the gluon field strength tensors, λ^C the 8 Gell-Mann matrices generators of SU(3) group and g_s the strong coupling constant. The last one g_s, depends on the transferred momentum q^2 an it is equal to:

$$g_s = \frac{8\pi^2}{(11 - \frac{2}{3}n_f)log\frac{q}{\Lambda_{QCD}}} \tag{1.17}$$

where n_f is the number of flavours and Λ_{QCD} the energy scale of strong interactions experimentally evaluated $\Lambda_{QCD} \simeq= 200MeV$.

1.2 Test of Lepton Flavour Universality

Lepton flavour Universality (LFU) implies equality of coupling between the gauge bosons and the three families of leptons. It implies that the branching fractions of e, μ and τ differ only by phase space and helicity-suppressed contributions. Lepton Flavour Universality is enforced in the Standard Model (SM) by construction and therefore, any violation would be a clear sign of New Physics (NP).
Over the years, the LFU has been tested but has been proven to be an accurate description in several systems. Recent hints of lepton non-universal effects have been seen measuring the ratio of dielectron to dimuon branching ratio of $b \to s l^+ l^-$ rare transitions and in the $R(D^{(*)}) \equiv \mathcal{B}(\bar{B}^0 \to D^{(*)+}\tau^-\bar{\nu}_\tau)/\mathcal{B}(\bar{B}^0 \to D^{(*)+}\mu^-\bar{\nu}_\mu)$ ratios.

1.2.1 R(K) and $R(K^{0*})$

The rare decays involving $b \to s l^+ l^-$ transitions are allowed only at loop level due to the absence of flavour changing neural currents at tree level in SM. Then, they are highly sensitive to virtual particle and interaction, such Z$\prime$ boson mediating the transition from b to s quarks [8]. In particular, by comparing decays with different leptons in final state, it is possible to probe NP involving the flavour universality violation among the different generations.
The ratio of

$$R(K) = \frac{\mathcal{B}(B^+ \to K^+\mu^-\mu^+)}{\mathcal{B}(B^+ \to K^+ J/\psi(\to \mu^-\mu^+))} \Big/ \frac{\mathcal{B}(B^+ \to K^+e^-e^+)}{\mathcal{B}(\bar{B}^0 \to K^+ J/\psi(\to e^-e^+))}$$

branching fractions is predicted to be the unity within an uncertainty of $\mathcal{O}(10^{-3})$, but the LHCb measurement (performed to an integrated luminsity of about $3fb^{-1}$) results to be $R(K) = 0.745^{+0.090}_{-0.074} \pm 0.036$, compatible with this SM value at 2.6σ [9]. In figure 1.1 the available measurements, which include also the current BaBar [10] and Belle [11] results, as a function of q^2 are presented.

The ratio of

$$R(K^{0*}) = \frac{\mathcal{B}(B^+ \to K^{*0}\mu^-\mu^+)}{\mathcal{B}(B^+ \to K^{*0}J/\psi(\to \mu^-\mu^+))} \Big/ \frac{\mathcal{B}(B^+ \to K^{*0} + e^-e^+)}{\mathcal{B}(\bar{B}^0 \to K^{*0}J/\psi(\to e^-e^+))}$$

is update recently thank to a LHCb measurement. It results to be compatible with the SM expectation at level of 2.2-2.3 and 2.4-2.5 standard deviations in the low and central q^2 regions respectively, as shown in figure 1.1 The figure reports also the other analogue measurements done at Belle [11] and Babar [10] .

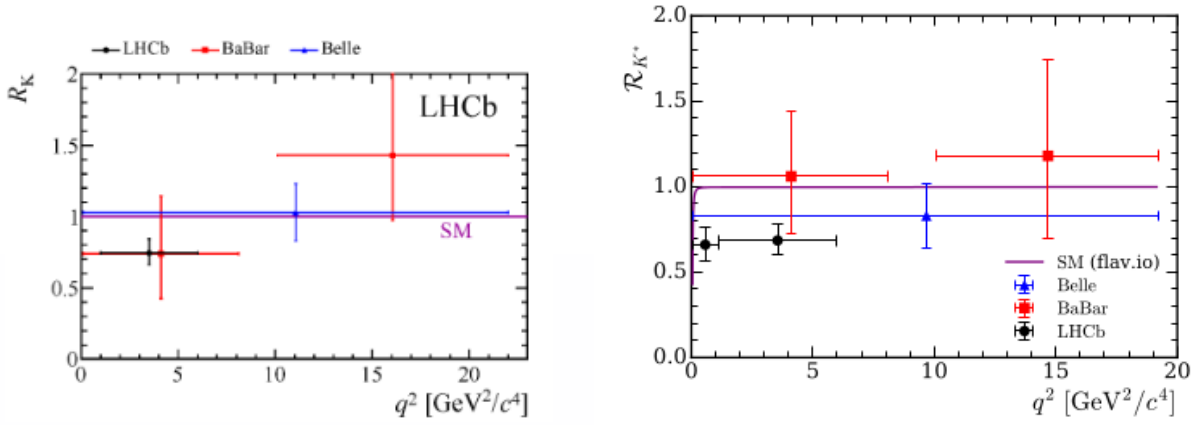

Figure 1.1: Summary of R(K) [9] (left) and R(K^{0*}) [12] (right) measurements.

1.2.2 R(D^*) and $R(D)$

A large class of models extending the SM contain additional interaction involving enhanced couplings to the third generation which would violate the universality. Therefore, semileptonic decays of b hadrons to the third generation provide a sensitive probe for such effects. In particular, the B meson decays with tau lepton in the final state can show NP contributions not present in the processes with light leptons, since the tau mass can reduce the helicity suppression of certain semileptonic decay amplitudes which are unobservables in decays with light leptons in the final state [13] [14]. Therefore many measurements of $\mathcal{B}(\bar{B}^0 \to D^{(*)+}\tau^-\bar{\nu}_\tau)$ are performed. In order to simplify the reconstruction efficiencies the measurements are done normalized to $\mathcal{B}(\bar{B}^0 \to D^{(*)+}\mu^-\bar{\nu}_\mu)$. Many NP model can be tested using this decay, such

as the 2HDM of type II and III, the leptoquark model and Minimal Supersymmetric Model (MSSM) [13,14]. In the 2HDM model of type II, two Higgs doubled are expected: the first one couples to down quarks and charged leptons, while another one gives the masses to the up quarks. In the 2HDM model of type III both of doublets couples to up and downs quarks. The leptoquarks model predicts new particles, the leptoquarks, which decay into a lepton and a quark. Finally, in MSSM the fermions have a bosonic superpartners called sfermions and the boson conversely. Many measurements of $R(D^{(*)}) \equiv \mathcal{B}(\bar{B}^0 \to D^{(*)+}\tau^-\bar{\nu}_\tau)/\mathcal{B}(\bar{B}^0 \to D^{(*)+}\mu^-\bar{\nu}_\mu)$ has been performed. In spring 2015, this quantity has been measured from LHCb Collaboration 2.1 σ far from SM expectations [13], confirming a discrepancy with respect of SM prediction, already measured by Babar [15] and Belle [16]. In 2016 Belle has published a measurement using a semileptonic tagging method, different from the previous one in which an hadronic method was utilized, obtaining a valued compatible with the SM at 1.6σ level [17]. A further improvement realized by Belle Collaboration performing a simultaneous measurement of $R(D^*)$ and the τ polarization [18], has allowed to define an average value for $R(D^*)$ compatible with SM at 3.4σ. At the B factories have been performed also the $R(D)$ measurements [15] [16]. In figure 1.2 the prospect of all $R(D^*)$ and of $R(D)$ measurements and in figure 1.3 the HFAG plot combining the two quantities, are shown.

1.2.3 R(Λ_c^*)

This thesis presents the first measurement of

$$R(\Lambda_c^*) = \frac{\mathcal{B}(\Lambda_b^0 \to \Lambda_c^*\tau^-\bar{\nu}_\tau)}{\mathcal{B}(\Lambda_b^0 \to \Lambda_c^*\mu^-\bar{\nu}_\mu)} \tag{1.18}$$

where

- $\Lambda_c^* \equiv \Lambda_c^+(2625)$,
- $\Lambda_c^{*+} \to \Lambda_c^+\pi^+\pi^-$,
- $\Lambda_c^+ \to pK^-\pi^+$,

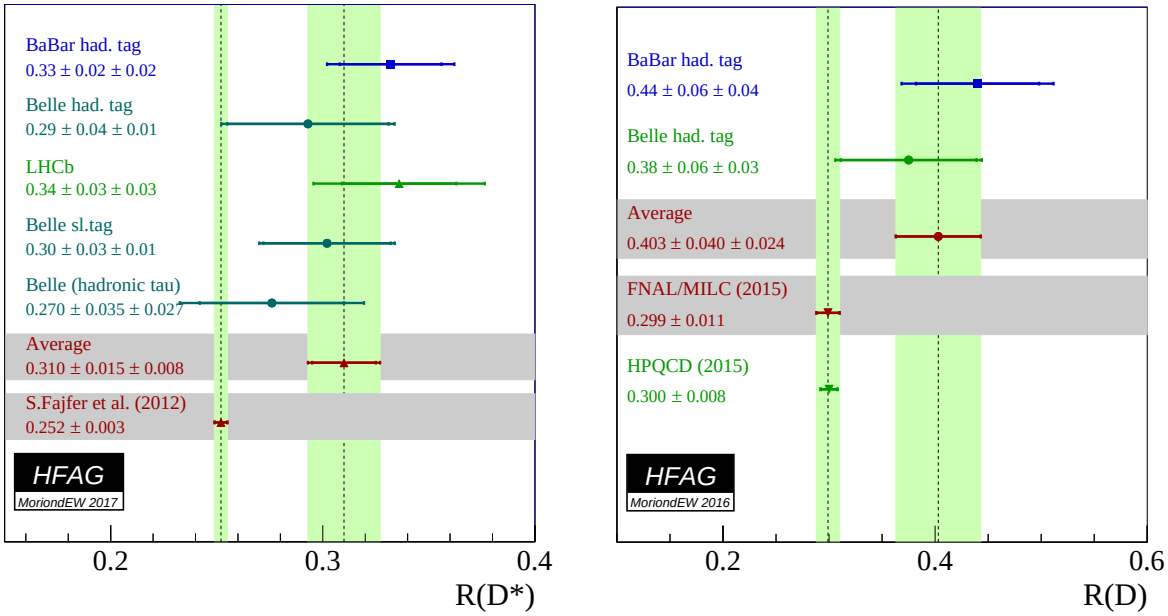

Figure 1.2: HFAG summary of R(D^*) (left) and R(D) (right) measurements.

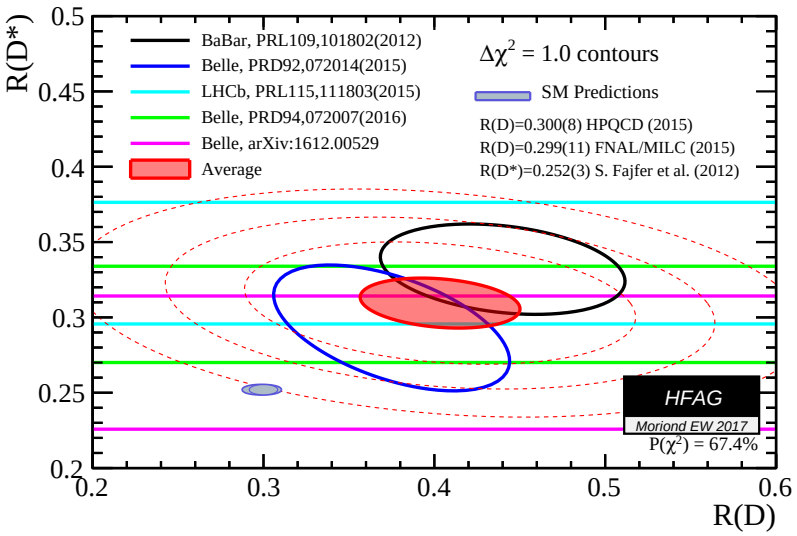

Figure 1.3: HFAG average of R(D^*) and R(D) measurements.

- and $\tau^- \to \mu^- \bar{\nu}_\mu \nu_\tau$.

As it is described in the previous sections, there are new physics hints appearing as a consequence of flavour universality violations which can be probed using the R measurements. Several test has been performed using the B mesons decays and many NP scenarios have been hypothesized to explain the discrepancies with respect to SM predictions. The study of the ana-

logue observables in the baryonic sector allows, or not, to confirm this discrepancy with respect to the SM expectations. Moreover, the presence of baryonic measurements gives the possibility to the theorists of inserting also the baryon decays behaviors in their models or to develop others aimed. In particular, in this thesis, the Λ_b^0 semimuonic and semitauonic decays which involves excited Λ_c particles are studied. It has been preferred to choose the excited states, and not the fundamental one to avoid the contamination to the studied channels due to unknown excited decays. The measurement based on Λ_c ground state semileptonic will be an interesting following measurement.

1.3 The Theory of Baryon Semileptonic Decays $b \to c l \nu_l$

1.3.1 Matrix Elements

In this thesis, the $\Lambda_b^0 \to \Lambda_c^+(2625) l^- \bar{\nu}_l$ decays are searched where $l^- = \mu^- \tau^-$. Moreover, some presented studies involve also the $\Lambda_b^0 \to \Lambda_c^+(2595) l^- \bar{\nu}_l$. The Feynman diagram for these decays is shown in figure 1.4. $\Lambda_c^+(2625)$ and $\Lambda_c^+(2595)$, are two excited state of the Λ_c^+ baryon, characterized respectively by $J^P = \frac{3}{2}^-$ and $J^P = \frac{1}{2}^-$.

The transition matrix element for the semileptonic decay of a baryon B_{bq}

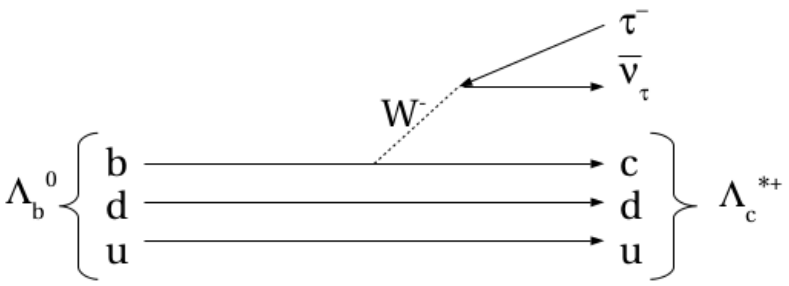

Figure 1.4: Feynman diagram of $\Lambda_b^0 \to \Lambda_c^{*+} \tau^- \bar{\nu}_\tau$.

into a state containing another baryon B_{cq} can be written as a term proportional to the product of a leptonic current L^μ and of a hadronic current H^μ

which are mediated by a W boson:

$$\mathcal{M} = -i\frac{G_F}{\sqrt{2}} V_{bc} L^\mu H_\mu \tag{1.19}$$

where:

- $\frac{G_F}{\sqrt{2}} = \frac{g^2}{8M_W^2}$ is the Fermi coupling constant;
- V_{bc} is the CKM matrix element;
- $L^\mu = \bar{u_l}\gamma^\mu(1-\gamma_5)u_{\nu_l}$ is the lepton current;
- $H^\mu = \langle \Lambda_c^*(p',s')|J_\mu|\Lambda_b(p,s)\rangle$ is the hadronic current
  in which J_μ is the weak current operator which couples to the W boson: $J_\mu = \bar{c}\gamma_\mu(1-\gamma_5)b$, p,p' are the momenta and s,s' the spin polarization vector of the two baryons .

Since the two baryon interacts strongly, and in particular since the quarks are confined, the hadron current will contain some term that parametrizes the non perturbative behavior of the QCD called form factors. They depends on initial and final state and they are measurable experimentally.
The hadronic matrix elements of the vector and axial current for a Λ_b^0 decays to daughter Λ_c^* baryion with $J^P = \frac{3}{2}^-$ and $J^P = \frac{1}{2}^-$ are respectively:

- $\langle \Lambda_c^{\frac{3}{2}^-}(p',s')|V_\mu|\Lambda_b(p,s)\rangle =$

$$= \bar{u}^\alpha(p',s')\left[\frac{p_\alpha}{m_{\Lambda_b}}(F_1(q^2)\gamma_\mu + F_2(q^2)\frac{p_\mu}{m_{\Lambda_c}} + F_3(q^2)\frac{p'_\mu}{m_{\Lambda_c^{\frac{3}{2}^-}}}) + F_4 g_{\alpha\mu}\right]u(p,s) \tag{1.20}$$

$\langle \Lambda_c^{\frac{3}{2}^-}(p',s')|V_\mu|\Lambda_b(p,s)\rangle =$

$$= \bar{u}^\alpha(p',s')\left[\frac{p_\alpha}{m_{\Lambda_b}}(G_1(q^2)\gamma_\mu + G_2(q^2)\frac{p_\mu}{m_{\Lambda_c}} + G_3(q^2)\frac{p'_\mu}{m_{\Lambda_c^{\frac{3}{2}^-}}}) + G_4 g_{\alpha\mu}\right]\gamma_5 u(p,s) \tag{1.21}$$

in which the spinor $\bar{u}^\alpha(p',s')$ satisfies the conditions:
$p'_\alpha \bar{u}^\alpha(p',s') = 0, \quad p'_\alpha \bar{u}^\alpha(\not{p}',s')\gamma_\alpha = 0, \quad \bar{u}^\alpha(p',s')\not{p}' = m_{\Lambda_c^{\frac{3}{2}^-}}\bar{u}^\alpha(p',s').$

- $\langle \Lambda_c^{\frac{1}{2}-}(p',s')|V_\mu|\Lambda_b(p,s)\rangle =$

$$= \bar{u}^\alpha(p',s')\left[F_1(q^2)\gamma_\mu + F_2(q^2)\frac{p_\mu}{m_{\Lambda_c}} + F_3(q^2)\frac{p'_\mu}{m_{\Lambda_c^{\frac{1}{2}-}}}\right]u(p,s) \quad (1.22)$$

$\langle \Lambda_c^{\frac{1}{2}-}(p',s')|V_\mu|\Lambda_b(p,s)\rangle =$

$$= \bar{u}^\alpha(p',s')\left[G_1(q^2)\gamma_\mu + G_2(q^2)\frac{p_\mu}{m_{\Lambda_c}} + G_3(q^2)\frac{p'_\mu}{m_{\Lambda_c^{\frac{1}{2}-}}})\right]\gamma_5 u(p,s) \quad (1.23)$$

where F_i and G_i are the baryons form factors.
Weak decays of hadrons involving one or more heavy quarks, $m_Q >> \Lambda_{QCD}$ have an additional symmetry in the effective Lagrangian, the heavy quark symmetry [19]. This symmetry arises because one a quark becomes sufficiently heavy, its mass becomes irrelevant to the non perturbative light quarks and gluons. In this situation the heavy quarks motion will fluctuate only slightly about the light quarks and they will behave like a stationary sources of color field. The QCD Lagrangian becomes symmetric for exchange of b with c quarks in the limit of $m_b \to \infty$ and $m_c \to \infty$, but the magnitude of color field and the heavy quark mass difference are unchanged. As a consequence of the heavy quark symmetry, the previous shown form factors resulted correlated each other, reducing the quantities which are necessary to study to one, the Isgur-Wise function $\xi(q^2)$, and it is known the value of the form factor when the momentum of final state hadron containing c is null with respect to hadron in the initial state containing b. This configuration is called at zero recoil and corresponds to the maximum transferred momentum q^2:

$$q^2 = m_{W*}^2 = (p^\mu_{\Lambda_b^0} - p^\mu_{\Lambda_c^*})^2 = m^2_{\Lambda_b^0} + m^2_{\Lambda_c^*} \quad (1.24)$$

Since the mass of b and c quarks are not infinite, the symmetry is broken and corrections has to be estimated in a $1/m_Q$ expansion (Heavy Quark Effective Theory).
The form factor can be expressed also as a function of w, the scalar product

of four velocity transferred:

$$w = v_{\Lambda_b^0} \cdot v_{\Lambda_c^*} = \frac{m_{\Lambda_b^0}^2 + m_{\Lambda_c^*}^2 - q^2}{2 m_{\Lambda_b^0} m_{\Lambda_c^*}} \tag{1.25}$$

and therefore, by construction $\xi(1) = 1$. Heavy quark symmetry predicts the relations among factors but not the kinematic dependence.
The baryon matrix elements can be rewritten [20] as

$$H^\mu = \langle \Lambda_c^*(v', s') | \bar{c} \gamma_\mu (1 - \gamma_5) b | \Lambda_b(v, s) \rangle = \xi(w) \bar{u}(v') \bar{c} \gamma_\mu (1 - \gamma_5) b u(v) \tag{1.26}$$

And then,

$$\begin{aligned} F_i &= C_i(m_b, m_c, w) \xi(w) \\ G_i &= C_i^5(m_b, m_c, w) \xi(w) \end{aligned} \tag{1.27}$$

where C_i are evolution coefficients and $\xi(w)$ is the Isgur-Wise function.

1.3.2 Decay Rates

The decay rate that arises from any transition matrix elements is [21]:

$$d\Gamma = \frac{1}{2 m_{\Lambda_b^0}} \frac{G_F^2}{2} |V_{bc}|^2 \left(\prod_f \frac{d^3 p_f}{8 \pi^3 2 E_f} L^{\mu\nu} H_{\mu\nu} (2\pi)^4 \delta^{(4)} (p_{\Lambda_b^0} - \sum p_f) \right) \tag{1.28}$$

where

- f refers to the final state particles;
- $L^{\mu\nu}$ is the leptonic tensor:

$$L^{\mu\nu} = 8 [p_l^\mu p_{\nu_l}^\nu + p_{\nu_l}^\mu p_l^\nu - g^{\mu\nu} p_l \cdot p_{\nu_l} + i \epsilon^{\mu\nu\alpha\beta} p_{l\alpha} p_{\nu_l \beta}]$$

- $H^{\mu\nu}$ is the hadronic tensor:

$$H^{\mu\nu} = \sum_{spin} \langle \Lambda_c^* | J_\nu^\dagger | \Lambda_b^0 \rangle \langle \Lambda_c^* | J \mu | \Lambda_b^0 \rangle$$

  This tensor has to have the Lorentz structure with coefficients α,β_{+-}, β_{-+}, β_{++}, β_{--},γ expressed in term of the form factors.

Defining $x = E_{lepton}/m_{\Lambda_b^0}$ and $y = q^2/m^2_{\Lambda_b^0}$, the complete expression for the differential rate results:

$$\frac{d^2\Gamma}{dxdy} = \frac{G_F^2 m^5_{\Lambda_b^0}|V_{bc}|^2}{64\pi^3}[\alpha C_\alpha + \beta_{++}C_{\beta_{++}} + \beta_{+-}C_{\beta_{+-}} + \beta_{-+}C_{\beta_{-+}} + \beta_{--}C_{\beta_{--}} + \gamma C_\gamma] \tag{1.29}$$

where

$$C_\alpha = \frac{2}{m^2_{\Lambda_b^0}}\left(y - \frac{m_l^2}{m^2_{\Lambda_b^0}}\right),$$

$$C_{\beta_{--}} = \frac{m_l^2}{m^2_{\Lambda_b^0}}\left(y - \frac{m_l^2}{m^2_{\Lambda_b^0}}\right),$$

$$C_{\beta_{-+}} = C_{\beta_{+-}} = \frac{m_l^2}{m^2_{\Lambda_b^0}}\left[4(x - x_m) - y - \frac{m_l^2}{m^2_{\Lambda_b^0}}\right],$$

$$C_{\beta_{++}} =$$

$$8[x(2x_m + y) - 2x^2 - y/2] - \frac{m_l^2}{m^2_{\Lambda_b^0}}\left(\frac{m_l^2}{m^2_{\Lambda_b^0}} - \frac{4m^2_{\Lambda_c^*}}{m^2_{\Lambda_b^0}} - 8x - 3y\right),$$

$$C_\gamma = \mp 2y\left[2x_m - 4x + y + \frac{m_l^2}{m^2_{\Lambda_b^0}}(2x_m + y)\right]$$

in which $x_m = (m^2_{\Lambda_b^0} - m^2_{\Lambda_c^*})2m^2_{\Lambda_b^0}$ and the sign of C_γ is in according to the lepton sign.

1.4 $\Lambda_b^0 \to \Lambda_c^*$ Form Factors in a Quark Model

At this moment, the only form factor calculation of $\Lambda_b^0 \to \Lambda_c^*$ which allows to estimate the decay rate for the $\Lambda_b^0 \to \Lambda_c^* \tau^- \bar{\nu}_\tau$ is performed in the framework of constituent quark model [21]. It has high hopes that this thesis persuades to perform new lattice QCD, HQET or model quark calculations.
A constituent quark model is based on the assumption that the constituent of the hadrons are only the constituent quarks, that is the valence quarks surrounded by a cloud of virtual quarks and gluons. A quark model calculation estimates the baryon wave function and used it in order to compute the

matrix elements which appears in the hadronic current. The quarks interactions are instantaneous and therefore it can be described by time independent Schroedinger equation, defined by a potential which takes in account of the asymptotic freedom and confinement QCD characteristics. In particular, the Hamiltonian according the used model used takes the form:

$$H = \sum_{i=1}^{3} K_i + \sum_{i<j=1}^{3} (V_{conf}^{ij} + H_{hyp}^{ij}) \tag{1.30}$$

where

- K_i is the semi-relativistic kinetic energy of the i^{th} quark;

$$K_i = \sqrt{p_i^2 + m_i^2}$$

- V_{conf}^{ij} is the spin independent semi harmonic oscillator confining potential used by Capstick and Isgur [22]

$$V_{conf}^{ij} = C_{qqq} + \frac{br_{ij}}{2} - \frac{2\alpha_{Coul}}{3r_{ij}}$$

  where $r_{ij} = |r_i - r_j|$.

- H_{hyp}^{ij} is the hyperfine interaction assumed to have the form:

$$H_{hyp}^{ij} = \frac{2\alpha_{hyp}}{2m_i m_j} \left\{ \frac{8\pi}{3} S_i \cdot S_j \delta^3(r_{ij}) + \frac{1}{r_{ij}^3} \left[\frac{3(S_i \cdot r_{ij})(S_j \cdot r_{ij})}{r_{ij}^2} - S_i \cdot S_j \right] \right\}$$

  The first term is a contact term, while the second one is a tensor. The spin orbit interaction is neglected. $\alpha_{Coul}, \alpha_{hyp}, b, C_{qqq}$ and m_i, listed in table 1.2, are not fundamental but phenomenological parameters obtained from a fit to the spectrum of baryon states.

The values are evaluated expanding the baryon wave function int the harmonic oscillator basis.

In table 1.3 the form factors of $\Lambda_b^0 \to \Lambda_c^* \tau^- \bar{\nu}_\tau$ calculated at recoil point are listed.

The Isgur-Wise function obtained using this model is [21]:

$$\xi(w) = e^{\left[-\frac{3m_\sigma^2}{\alpha^2}(w-1)\right]} \tag{1.31}$$

Parameter	Fitted Value
m_σ (GeV)	0.38
m_s (GeV)	0.59
m_c (GeV)	1.83
m_b (GeV)	5.17
b $(\mathrm{GeV})^2$	0.17
α_{Coul}	0.09
α_{hyp}	0.26
C_{qqq} (GeV)	-1.45

Table 1.2: Hamiltonian parameters obtained from fit to the baryon states in which the baryon wave function is built in the harmonic oscillator basis.

J^P	F_1	F_2	F_3	F_4	G_1	G_2	G_3	G_4
$\frac{1}{2}^-$	0.15	-0.95	0.09	-	1.01	-0.82	0.04	-
$\frac{3}{2}^-$	-1.13	0.15	0.12	-0.05	-0.87	0.15	-0.12	0.05

Table 1.3: $\Lambda_b^0 \to \Lambda_c^*$ form factors calculated at recoil point in the HOSR model (harmonic oscillator semi relativistic).

It has the same functional dependence for $\Lambda_c^+(2625)$ and $\Lambda_c^+(2595)$, but different parameters, listed in table 1.4.

The Isgur Wise function may be expanded as

Parameter	Value
m_σ (GeV)	0.38
$\alpha_{\frac{3}{2}^-}$	0.47
$\alpha_{\frac{1}{2}^-}$	0.55

Table 1.4: Parameters of the Isgur-Wise function in the model HOSR [21].

$$\xi(w) = 1 - \rho^2(w-1) + \frac{\sigma}{2}(w-1)^2 + ...$$

where ρ^2 is the slope of the form factor at not recoil point and σ^2 is the curvature. Expanding 1.31 for $w = 1$, it is possible to find the ρ^2 value equal to:

$$\rho^2 = \frac{3m_\sigma^2}{\alpha^2}$$

Finally in figure 1.5 the differential rates $d\Gamma/dq^2$ calculated using the model the $\Lambda_b^0 \to \Lambda_c^* \tau^- \bar{\nu}_\tau$ and $\Lambda_b^0 \to \Lambda_c^* \mu^- \bar{\nu}_\mu$ decays [21] are shown.

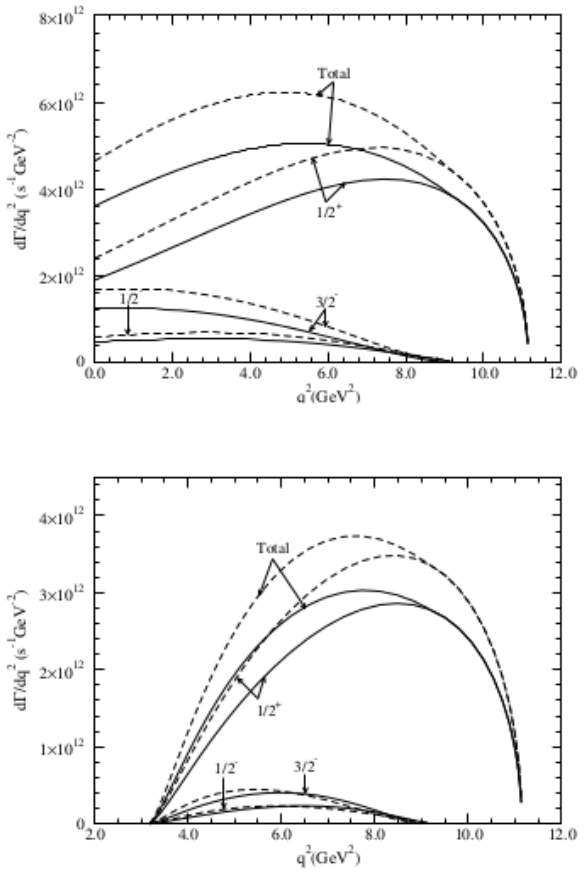

Figure 1.5: The differential rates $d\Gamma/dq^2$ calculated using the model the $\Lambda_b^0 \to \Lambda_c^* \tau^- \bar{\nu}_\tau$(top) and $\Lambda_b^0 \to \Lambda_c^* \mu^- \bar{\nu}_\mu$ decays (bottom) [21].

1.5 Standard Model Expectation for $\mathcal{B}(\Lambda_b^0 \to \Lambda_c^* \tau^- \bar{\nu}_\tau)/\mathcal{B}(\Lambda_b^0 \to \Lambda_c^* \mu^- \bar{\nu}_\mu)$

Measurements of the $\Lambda_b^0 \to \Lambda_c^*$ Form Factors are not available yet so the Standard Model predictions for the ratios $R(\Lambda_b^*)$ have to fully rely on calculations. The only existing calculation for both $\Lambda_b^0 \to \Lambda_c^* \mu^- \bar{\nu}_\mu$ and $\Lambda_b^0 \to \Lambda_c^* \tau^- \bar{\nu}_\tau$ decay widths are available in [21] and reported in table 1.5 for both the semirelativistic (SR) and non-relativistic (NR) heavy-quark treatment considered by the authors.

Table 1.5 reports for comparisons also the prediction obtained considering only the differences in the phase-space due to the large τ mass. The corresponding Dalitz plot is shown in figure 1.6 for illustration.

It is not easy to assign a reliable uncertainty to the estimations of R re-

Table 1.5: $(\Lambda_b^0 \to \Lambda_c^* \ell^- \bar{\nu}_\ell)$ decay width (in units of $10^10\ s^{-1}$) predictions with the quark model in Ref. [21] with the NR and SR approximations. For completeness we report also the decay Branching Fraction using $\tau_{\Lambda_b} = (1.466 \pm 0010)\ ps$, [?], and for comparison, the existing measurements. In the last rows we report the predicted R for Λ_c, $\Lambda_c(2595)$ and $\Lambda_c(2625)$ final states in the quark model and considering only the differences in the phase space.

Λ_c	J^P	$\Gamma(NR)$	$\Gamma(SR)$	BF(NR)	BF(SR)	Experiment [6]
	$\mathcal{B}(\Lambda_b^0 \to \Lambda_c^* \mu^- \bar{\nu}_\mu)$					
Λ_c	$1/2^+$	4.60	5.39	6.7%	7.9%	$6.2^{+1.4}_{-1.3}$%
$\Lambda_c(2595)$	$1/2^-$	0.45	0.52	0.7%	0.8%	$0.79^{+0.40}_{-0.35}$%
$\Lambda_c(2625)$	$3/2^-$	0.95	0.90	1.4%	1.3%	$1.3^{+0.6}_{-0.5}$%
	$\mathcal{B}(\Lambda_b^0 \to \Lambda_c^* \tau^- \bar{\nu}_\tau)$					
Λ_c	$1/2^+$	1.90	2.09	2.8%	3.1%	
$\Lambda_c(2595)$	$1/2^-$	0.10	0.11	0.15%	0.16%	
$\Lambda_c(2625)$	$3/2^-$	0.15	0.13	0.22%	0.19%	
R		R (NR)	R (SR)	Phase Space		
Λ_c	$1/2^+$	0.41	0.39	0.273		
$\Lambda_c(2595)$	$1/2^-$	0.22	0.21	0.214		
$\Lambda_c(2625)$	$3/2^-$	0.158	0.144	0.206		

ported in table 1.5. Both model approximations predict BF for the muonic decay mode, consistent with the existing measurements, but the experimental uncertainties exceed the 20%. Just to set a reference value, the average between the NR and SR calculations has been taken as central value and assigned as uncertainty due to the model, the total difference between the two calculation. The resulting predictions are:

$$\begin{aligned} R(\Lambda_c) &= 0.40 \pm 0.020 \\ R(\Lambda_c(2595)) &= 0.215 \pm 0.010 \\ R(\Lambda_c(2625)) &= 0.151 \pm 0.014 \end{aligned} \tag{1.32}$$

The predicted $R(\Lambda_c) = 0.40 \pm 0.020$ is higher than the existing calculation based on Lattice, [23] that gives $R(\Lambda_c) = 0.3328 \pm 0.0074 \pm 0.0070$. It would be important to have further lattice calculations even for the excited Λ_c^* states.

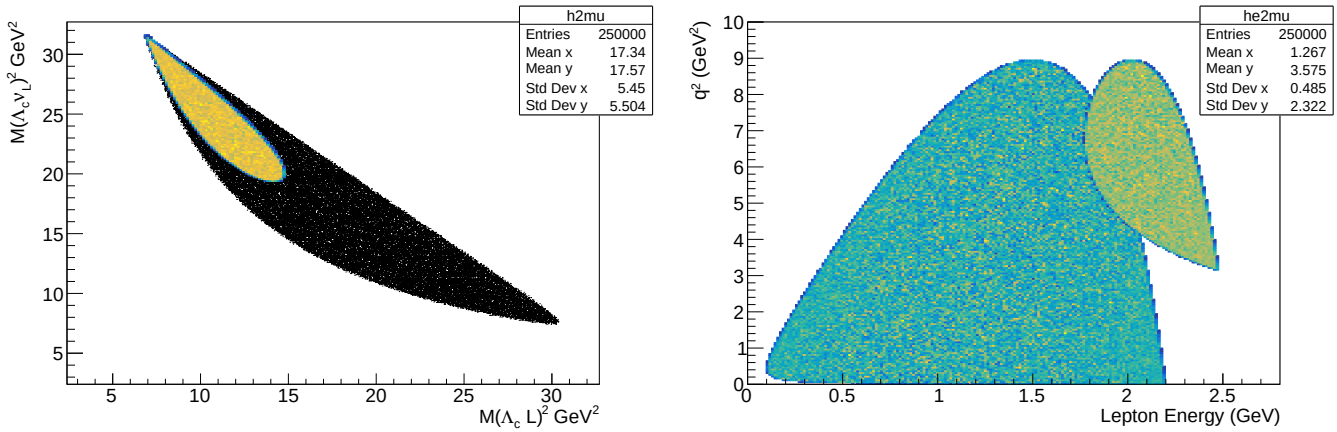

Figure 1.6: Left: Dalitz plot for the $\Lambda_b^0 \to \Lambda_c(2625)\mu^-\bar{\nu}_\mu$ (black) and $\Lambda_b^0 \to \Lambda_c(2625)\tau^-\bar{\nu}_\tau$ (yellow). Right: similar distribution in the $q^2 - E_\ell$ plane. The effect of the large masses of the τ is clearly visible in these plots.

Chapter 2

The LHCb Experiment

This chapter describes the LHC Beauty experiment, LHCb, which has been designed and built to check the consistency of the Standard Model through precision measurements of the sides and angles of the Cabibbo-Kobayashi-Maskawa triangle, and to search for new physics in decays that are rare, or forbidden, in the Standard Model.

2.1 The Large Hadron Collider

The LHC is a circular collider of 26.66 Km circumference colliding two proton beams rotating in opposite directions. It is designed to collide protons onto protons at a center of mass energy of 14 TeV at an unprecedented luminosity of $10^{34} cm^{-2} s^{-1}$. In 2011 the centre of mass energy was kept at 7 TeV, whereas in 2012 it was kept at 8 GeV.

Bunches of 10^{11} protons each are obtained from hydrogen gas and are firstly accelerated to 50 MeV with a linear accelerator called LINAC2. They are then passed to the Proton Synchrotron Booster where their energy is increased to 1.4 GeV. Following this, they are injected into the Proton Synchrotron, accelerated to 25 GeV and transmitted to the Super Proton Synchrotron (SPS). The SPS accelerates the bunches to 450 GeV and finally injects them clockwise and counter-clockwise into the LHC ring. A total of about seven minutes is needed to fill both LHC rings. When the rings are filled the LHC further accelerates the protons in a ramp phase.

The four main detectors at the LHC: ATLAS, CMS, ALICE and LHCb,

are located at the four collision points. ATLAS and CMS are general purpose detectors and ALICE is designed to analyze lead-ion collisions that may also take place at the LHC. Figure 2.1 shows a schematic view of the SPS, the LHC ring and the detectors.

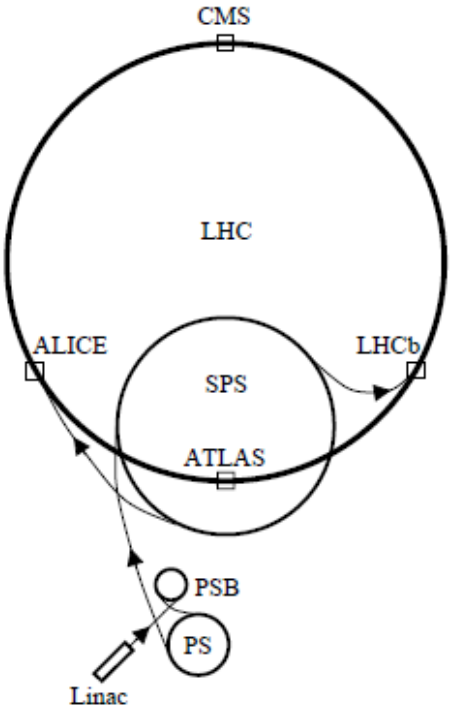

Figure 2.1: Schematic layout of the accelerator complex at CERN

2.2 The LHCb Detector

The LHCb detector is a forward arm spectrometer centered around the LHC beam pipe, 100 m underground.

At the interaction point, a proton-proton deep inelastic scattering occurs, producing a highly boosted virtual gluon and breaking up the incoming protons at a primary vertex. The main production mechanism for heavy quark production involves two initial gluons as shown in Figure 2.2. In general, at the LHC energy the two incoming partons have dissimilar momenta which boost the outgoing $b\bar{b}$ system. As a result, in the majority of events, both B hadrons originating from the same $b\bar{b}$ pair are located in the same forward

region, as we can note in Figure 2.3. This explains the choice of detector geometry.

LHCb measures particles which appear within its angular acceptance of 10 mrad to 250 mrad vertically, and 10 mrad to 300 mrad horizontally [24]. A large dipole magnet, producing a field in the vertical direction, breaks the symmetry between the vertical and horizontal planes. Approximately, one third of B hadrons lie within the LHCb acceptance. In terms of pseudo-rapidity $\eta = \ln\tan(\theta/2)$, where θ is the polar angle with respect to the beam axis, the acceptance is $1.8 < \eta < 4.9$.

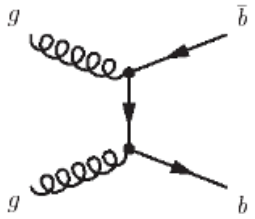

Figure 2.2: Feynman diagram of the dominant production mechanism of heavy quarks at the LHC.

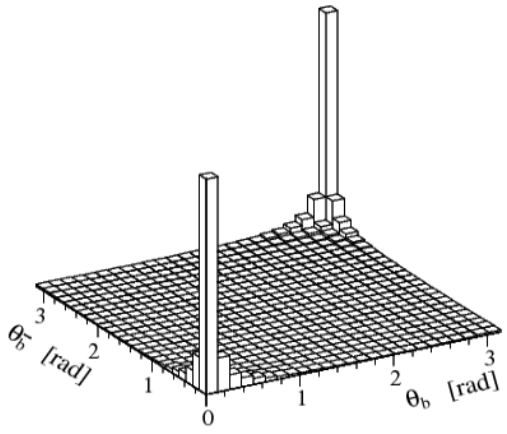

Figure 2.3: Angular distribution of $b - \bar{b}$ pairs at LHC. The axes show the polar angle θ of b and $\bar{b}$ with respect to the beam axis.

B hadrons are unstable and decay after travelling a mean path of 10 mm in the lab frame. Around fourty other particles are also producted at the primary vertex.

LHCb operated at luminosities of 2 (4) $\times 10^{32} cm^{-2} s^{-1}$ in 2011 (2012) [25]. These values are not the maximum allowed by LHC but they provide

good trigger performance and manageable detector occupancy. Running at a lower luminosity results in lower event multiplicity, thus simplifying time-dependent measurements and reduces the radiation damage to the detector. The measured cross section for $b\bar{b}$ events is $\sigma_{b\bar{b}} = (284 \pm 20 \pm 49)\mu b$ at center of mass energy of 7 TeV [24].

LHCb provides precise vertexing resolution and a precise momentum resolution which entails a high proper time ($[30, 50]\, fs$) and mass resolution($\sigma(m) \in [10, 25]\, MeV/c^2$ for fully reconstructed hadronic B decays). Moreover, it is characterized by a high trigger efficiency for the reconstruction of B meson decays and background suppression, and an excellent particle identification.

In order to minimize the interactions of particles with inactive detector material, which would lower the detection efficiency and degrade the momentum resolution, special care has been taken to reduce the amount of detector material.

The LHCb detector is shown in Figure 2.4. Starting form the left side, the VErtex LOcator [26] is built around the proton interaction region. Directly after it, a Ring Imaging CHerenkov detector, RICH-1 [27], is located. Then, there are the dipole magnet [28],the tracking system [**?**] [29] composed by stations TT, T1 and T2 and another Cherenkov detector, RICH-2 [27] . Afterwards the electromagnetic (ECAL [30]) and hadronic (HCAL [30]) calorimeters are present and finally there is a muon detector made of five stations (M1 - M5) [31]) . The beam-pipe has a conical shape and is made out of an aluminium-beryllium alloy.

LHCb uses a right-handed coordinate system with y pointing upwards, x horizontal and pointing to the outside of the LHC-ring and the z-axis along the beam. The proton-proton collisions take place around z=0, located at the left side in the figure.

2.3 The VeLo Detector

The Vertex Locator (VeLo) is placed around the interaction point and measures particle trajectories close to the interaction region. The high resolution

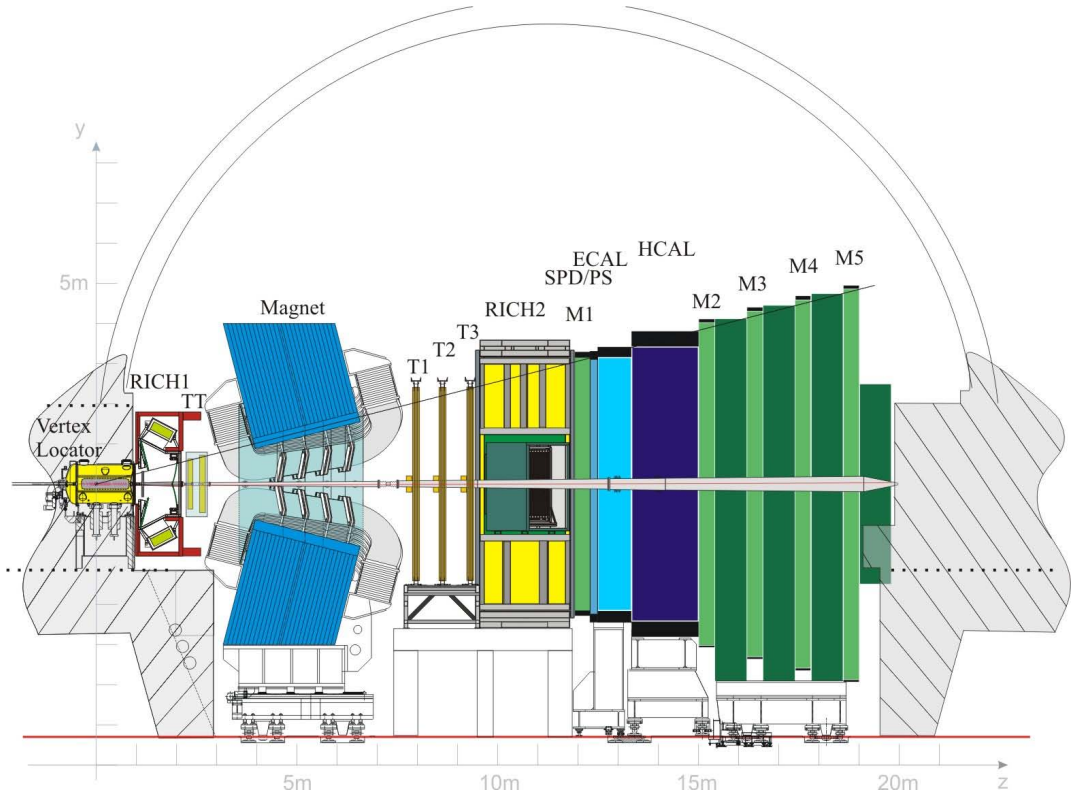

Figure 2.4: Schematic of the LHCb detector and its subdetectors.

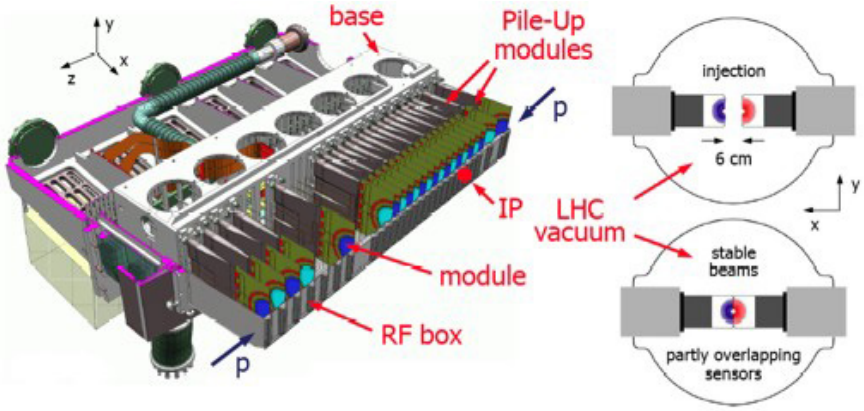

Figure 2.5: VeLo detector.

of the coordinate measurements of the tracks allows the reconstruction and separation of the primary interaction vertex from secondary decay vertexes of bottom and charmed mesons. These are essential for time dependent measurements and to determine the impact parameters of the decay products with respect to the primary vertex. These information are also relevant for the trigger, as described in next paragraphs.

The Velo detector consists of silicon modules, 300 μm thick, placed perpendicular to the beam, covering a pseudorapidity range of 1.6 $<\eta<$4.9. Charged particles produced by proton collisions traverse the silicon and generate electron-hole pairs; these are sensed using specific electronics.

This system comprises a silicon vertex detector and a pile-up veto counter. The pile-up veto counter is used in the L0-trigger to suppress events containing multiple pp interactions in a single bunch-crossing, by counting the number of primary vertex. It consists of two disks made of circular silicon strips to measure radial coordinate.

The silicon vertex detector consists of 25 station of silicon strips. Each station is split in an upper and lower half. This enables the retraction of the detectors by 3.0 cm from their operation position to allow a safe injection and acceleration of a new fill of proton bunches in the LHC. Each upper and lower station contains two half-disc detectors separated by 2 mm. One disc has radial strips measuring the ϕ coordinate, the other disc has circular strips measuring the radial coordinate (see figure 2.5).

To achieve the highest possible precision, the detector must be placed as close as possible to the interaction point. To reduce the distance and the material between the point of interaction and sensors, hence minimizing the outgasing phenomenon and multiple scattering, the Velo is placed in a foil vacuum vessel. The VeLo detectors are used in the high level trigger (see next subsections) to select b hadrons decays by detecting displaced secondary vertices. The higher trigger levels use the full vertex detector information to reconstruct and precisely measure a full decay chain.

The VeLo detector allows for a spatial resolution on vertexes of about 60 μm along the z axis and 10 μm along x and y. The resolution on impact parameter, e.g the distance of closest approch between a track and the reconstructed primary vertex, is about 20 μm for high transverse momentum tracks. The resolution on the decay length, the distance between the interaction point and the secondary vertex is within the range of 200-370 μm, depending on the decay channel.

2.4 Tracking Detectors

The tracking detector provides efficient reconstruction of charged tracks and precise measurement of their momentum and direction. The latter is also needed to reconstruct Cherenkov rings in the RICH detectors. The tracking detector also provides information for High level trigger (see next paragraphs). It is composed of four tracking stations: the Trigger tracker located between RICH-1 and the LHCb dipole magnet and T1-T3 located over 3 metres between the magnet and RICH-2.

The tracker system is schematically drawn in Figure 2.6.

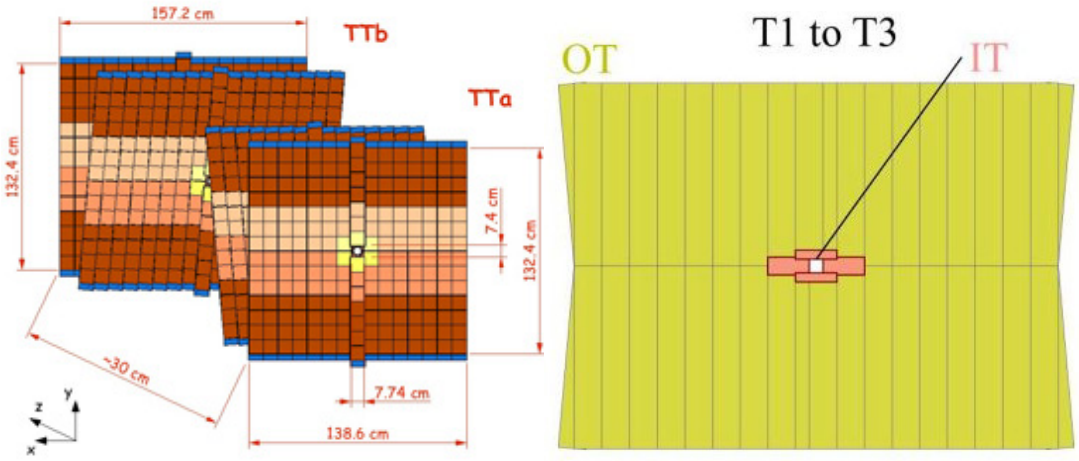

(a) TT (b) T1-T3

Figure 2.6: Tracking system. a) TT b) T1-T3 stations

TT consists of four layers of silicon micro-strip detectors arranged in pairs. Charged particles interacts with silicon atoms, creating hole-electron pairs and a localized electric current, which follows the path of the original particle. The first and the last layer have vertically-arranged readout strips, whereas the second and the third are rotated by ± 5 degrees in order to obtain a 3D reconstruction of the tracks.

Each T1, T2, T3 station, is divided into inner and outer parts.

The inner tracker (IT) is placed close to the beam pipe, and uses silicon microstrip detectors, the same as TT.

The outer tracker (OT) is located further from the beam pipe and is made up of thousands of gas-filled straw tubes. Whenever a charged particle passes

through, it ionizes the gas molecules, producing electrons. The position of the track is found by timing how long the electrons take to reach an anode wire situated in the center of each tube.

The IT and OT are built as complementary shapes and slightly offset in z-position.

The momentum resolution from the tracking system is about $\frac{\delta p}{p} = 0.4\%$ for momenta up to 200 GeV/c.

2.5 The magnet

The LHCb magnet is a dipolar magnet whose field is oriented along the y direction. Therefore, charged particles are deflected in the x-z plane in order to determine their momentum.

The maximum intensity of the magnetic field is 1.1 T and has overall bending power is $\int Bdl = 4T$. The magnet weights 1600 tonnes with an excitation current of 2.6 MA. Acceptances in the horizontal and vertical planes are 300 mrad and 200 mrad respectively.

2.6 RICH Detectors

The LHCb detector uses two Ring Imaging CHerenkov (RICH) detectors. RICH-1 is placed directly downstream of the Velo and before the main tracking system. RICH-2 is positioned after the tracking stations and in front of the calorimeters. The RICH detectors measure the Cherenkov angle of light emitted when a charged particle traverses a medium with a velocity higher than the speed of light in that medium. The RICH system is schematically drawn in Figure 2.7. Measurements of Cherenkov angles are used, together with momentum measurements by the main tracking system, to perform particle identification of charged tracks.

RICH detectors are based on the Cherenkov effect: when a charge track traverses a medium with a velocity v higher than the speed of light in that medium a cone of electromagnetic radiation, Cherenkov radiation, is emitted along the trajectory. Such radiation is emitted coherently at an angle θ_C with

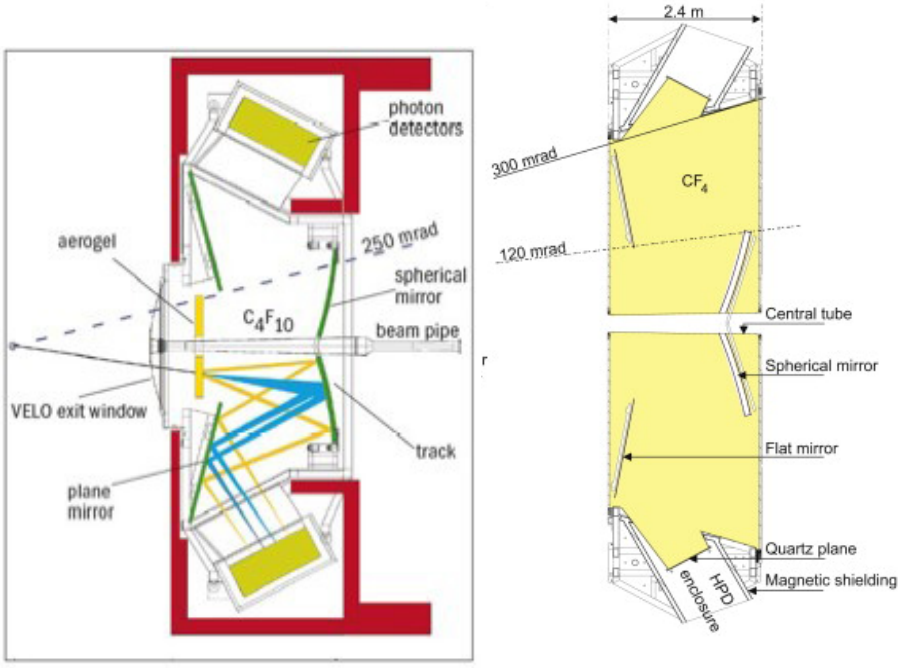

(a) RICH1 (b) RICH2

Figure 2.7: RICHes system.

respect to the direction of the motion such as:

$$\cos\theta_C = \frac{1}{\beta n}$$

where n is the refractive index. Particles can therefore be identified when their momentum and the opening angle of the Cherenkov radiation cone are known.

The Ring Imaging CHerenkov (RICH) detectors of LHCb measure θ_C by focusing the emitted light with spherical mirrors on a plane of photo-detectors (hybrid photodetectors). The photons emitted along the trajectory of the traversing particle form a ring on the photo-detector plane, with the radius proportional to θ_C.

The LHCb RICH detectors have to provide identification of charged particles over momentum range from 1 GeV/c up 150 GeV/c. In order to achieve this, several radiator materials with different refractive indices are used.

RICH-1 performs particle identification for momentum less than 60 GeV/c, over the full LHCb angular acceptance. There are two radiators in RICH-1. The first one is a 5 cm-thick aerogel layer with a refractive index n = 1.03.

It provides pion-kaon separation up to about 10 GeV/c. The second radiator is a volume filled with C_4F_{10} gas, refractive index n = 1.0014.

The RICH-2 detector is used to perform particle identification of high momentum tracks. This requires a lower refractive index, but a longer path length for the particles in order to manage to collect sufficient Cherenkov light, since the number of photons emitted is proportional to $N_\gamma = \sin^2\theta_C$. It has a reduced angular acceptance because high momentum tracks are produced at small angles. RICH-2 contains CF_4 gas providing 167 cm path length with refractive index n = 1.0005. It provides pion-kaon separation up to about 100 GeV/c.

To reduce the material in the LHCb acceptance, both RICH1 and RICH2 employ a combination of spherical and flat mirrors allowing the photon detector planes to be placed outside the detector acceptance. To further minimize the material, RICH-1 spherical mirrors are made of coated carbon-fiber composite material and the gas enclosure is mounted directly on the VELO exit window.

2.7 Calorimeters

The LHCb calorimetry consists of an electromagnetic (ECAL) and a hadron (HCAL) calorimeter. There are also two additional subsystems, the SPD (Scintillating Pad Detection) and PS (PreShower), which allow to improve spatial and energy resolution of electromagnetic showers. The main purpose of the LHCb calorimeter system is to trigger on electrons, photons and hadrons. It provides energy and position measurements of the particles produced in their angular acceptance, which are used in offline event analysis. Furthermore, the electromagnetic calorimeter measures photons and neutral pions in association with the hadronic calorimeter.

The LHCb calorimeters are segmented in a sequence of layers of passive absorbing material alternated by active detection layers. An incident particle is stopped in the calorimeters by a cascade of decays and interactions into progressively lower energy particles. These excite the molecules of active

plates which emit ultraviolet light proportional to the energy of the impinging particles. Scintillating plastics interwoven by wavelength-shifting (WLS) fibres are used as active material. The fibers collect the light emitted in the scintillators and transfer it to photomultiplier tubes. The passive absorption material is different for the two calorimeters: lead in ECAL and steel in HCAL.

The pad/pre-shower detector consists of a 12 mm thick lead radiator sandwiched between two scintillator layers. The SPD is used to trigger charged particles. In lead electrons radiate causing an early shower that can be detected by the pre-shower(PS) layer. This is used for the identification of photons.

ECAL consists of cells partitioned in 2 mm lead and 4 mm thick scintillator pads.

ECAL, in combination with SPD and PS, allows the measurement of energy and the discrimination of electrons, photons and π^0. The ECAL energy resolution is given by

$$\frac{\sigma(E)}{E} = \frac{10\%}{\sqrt{E}} \oplus 1.5\%$$

with E in GeV.

HCAL consists of 16 mm thick iron sheets, interspersed with 4 mm scintillator region. Almost all hadrons interact with the HCAL. Muons emerge from HCAL and are detected by the muon chambers. The ECAL energy resolution is

$$\frac{\sigma(E)}{E} = \frac{80\%}{\sqrt{E}} \oplus 10\%$$

with E in GeV.

2.8 Muon Chambers

Muon triggering and identification are fundamental requirements of the LHCb experiment. Muons are present in the final states of many CP-sensitive B decays and in particular are crucial in the measurements with semileptonic

decays studied in this thesis. Moreover, muon identification allows to determine the production flavour of neutral b hadron because a positive muon can only result from a b decay and a negative one from a $\bar{b}$ decay.

The main requirement of the muon detector is to provide high p_T tracks to the level 0 muon trigger and muon identification for the high-level trigger (HLT) and offline analysis. The system is composed of five stations (M1-M5) of rectangular shape, covering the whole acceptance of the LHCb detector. M1 is placed in front of the scintillating pad detector/pre-shower to avoid that trasversal momentum be affected by multiple scattering due to active material in the calorimeters. M2-M5 follow the hadron calorimeter (HCAL) and are separated by iron filters. The stations cover an area of 435 m^2. Each station is divided into four regions, R1 to R4, with increasing distance from the beam axis and therefore with decreasing density of particle expected. The granularity of the readout is higher in the horizontal plane, in order to give an accurate measurement of the track momentum and p_T. The muon chambers are composed of two types of detectors: in the outer region there are Multi Wire Proportional Chamber (MWPC) detectors, whereas in M1 there are triple GEM detectors because the expected particle rate exceeds the safe MWPC ageing limit. The muon system is schematically drawn in Figure 2.8.

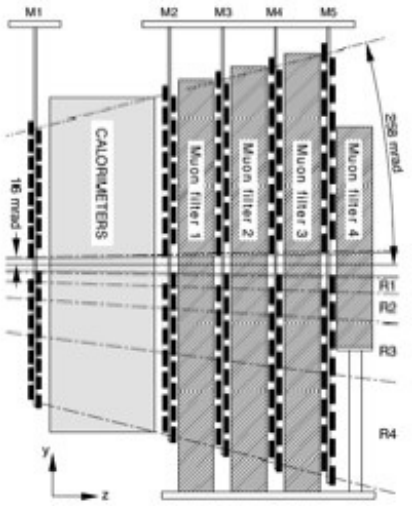

Figure 2.8: Muonic system.

Twelve GEMs are placed in the higher track density region, while the total system comprises 1392 chambers. The MWPCs are subdivided in four tungsten gaps 5 mm thick and filled with a gas composed by a mixture of Ar(50%), $CO_2(40\%)$ and $CF_4(10\%)$. Inside the gaps, wires with a diameter of 30 μm are placed at a distance of 2 mm from each other.

2.9 Trigger

b-Quark hadron decays can be distinguished from other inelastic pp interactions, by the presence of a secondary vertex and particles with high transverse momentum p_T. However, interesting events are a small fraction of the total sample, due to low branching fractions and limited detector acceptance. Therefore the trigger system must be very selective and efficient in extracting them. The LHCb trigger is composed of two levels: L0 (Level 0) and HLT (High Level Trigger). The first operates at hardware level synchronously with the 40MHz LHC bunch crossing frequency whereas the HLT is run asynchronously on a computer farm of about 16000 CPU cores.

The interaction producing a minimum of two reconstructible particles within the detector acceptance, therefore visibile events, occurs at a rate of 10MHz. The L0 reduces the rate of visible interactions from 10 MHz to 1 MHz. The HLT then reduces this to 3kHz. Figure 2.9 and 2.10 show the scheme of the LHCb trigger.

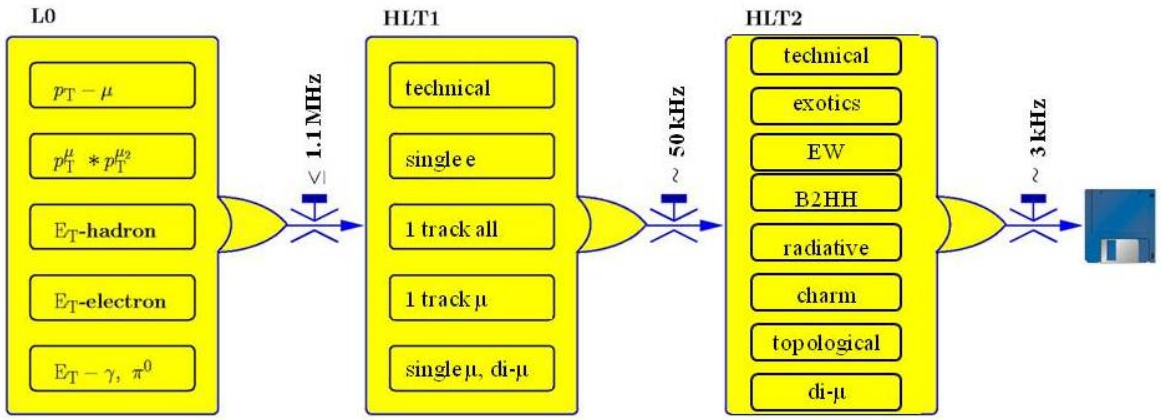

Figure 2.9: LHCb trigger scheme

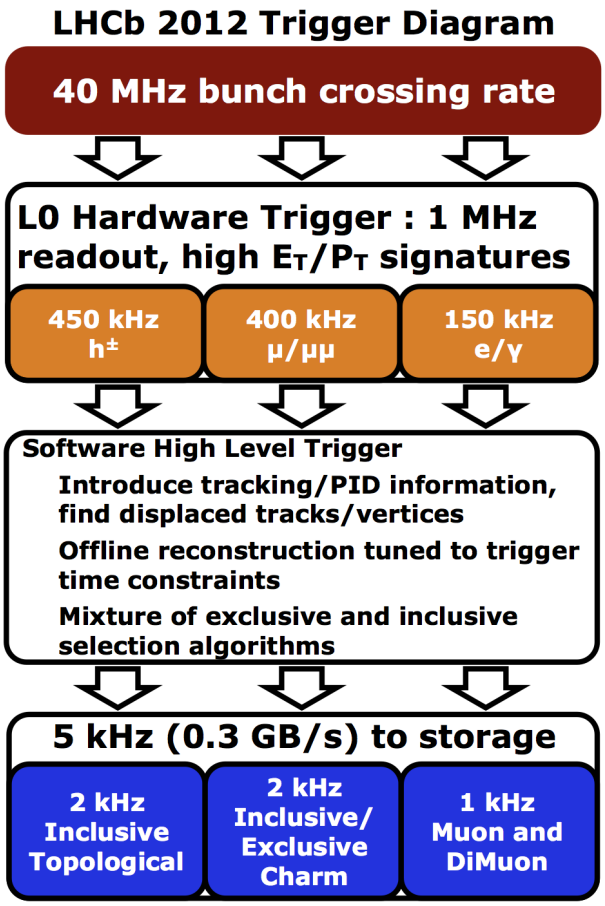

Figure 2.10: LHCb trigger rates

2.9.1 L0 trigger

B mesons regularly decay into particles with large transverse momentum p_t and energy E_t. The L0 trigger makes use of information from VeLo pile-up, Calorimeters and muon chamber to reconstruct the highest E_t photon, electron, hadron and muon.

Particles that meet the following requirements are triggered [19]:

- at least one cluster in the HCAL with $E_t > 2.5$ GeV;
- at least one cluster in the ECAL with $E_t > 2.5$ GeV;
- a muon candidate in the muon chambers with $p_t > 1.48$ GeV/c or two muons (dimuon trigger) with $p_t^{\mu_1} + p_t^{\mu_2} > 1.3 GeV/c$ [32]

In addition to this, to avoid reconstruction of events with a large number of tracks and primary vertices, events with a certain number of hits in the

SPD are rejected. In the 2011 run, the L0 global event cut was set to < 900 hits for the dimuon trigger and < 600 hits for all other triggers [32].

The pile-up system estimates the number of primary proton-proton interactions in each bunch crossing. If multiple interactions are detected the data capture is suppressed. The pile-up system, the calorimeter trigger and the muon trigger are all connected to the Level-0 Decision Unit (DU) which collects all the information for the final decision.

Typically the L0 is greater than 80% efficient for events containing a muon from a B-decay, $\sim 50\%$ efficient for events containing B decays and around $\sim 30\%$ for events with electrons from B decays.

2.9.2 High Level Trigger

The High Level Trigger (HLT) runs only on events passing the L0 trigger. It is divided in two steps: HLT1 and HLT2.

HLT1 reconstructs particles in the VeLo and determines the position of the primary vertex in the event. Moreover, it seeks to confirm the high p_t tracks identified by L0, by searching for them in the tracking system. HLT1 selects events with at least one track which satisfies minimum requirements in IP, p, p_t and track quality.

HLT2 searches for secondary vertices, and applies decay length and mass cuts to reduce the rate to the level at which the events can be written to storage and processed offline. It first performs a complete pattern recognition to find all tracks in the event, using VELO tracks as seeds. Then, a set of different selections are applied. Some of them are inclusive, aiming for generic B decays or resonances like $J\psi \to \mu^+\mu^-$ or $D^* \to D\pi$ and some of them are exclusive, aiming to provide the highest possible efficiency on specific B decay channels.

2.10 From Trigger to stripping

There are several phases in the processing of event data.

The first step is to collect data, triggering on events of interest. This pro-

cedure involves processing data coming from sub-systems using sophisticated and highly optimized algorithms in the High Level Trigger. The output of this step is written to storage in a *RAW* data format.

The *RAW* data are then used to perform event reconstruction, i.e the process which provides physical quantities such as particle trajectories, energy and momentum determinations, particle identification and so on, starting from detector hits.

The event reconstruction results in the generation of new data, DST, "Data Summary Tape". Actually, reduced DST, rDST, are written, i.e only necessary quantities, which allow the physics pre-selection algorithms to be run at a later stage, are written. The rDST is then analyzed according to the selection criteria, grouped in several streams. For each stream the rDST information is used to determine the four momentum corresponding to the measured particles, to locate primary and secondary vertices and reconstruct composite particles such as B and D candidates. A preselection algorithm is provided for each channel of interest (stripping line).

The events that pass the selection criteria will be fully re-reconstructed, recreating the full information associated with an event. The output of the stripping stage will be referred to as the (full) DST and contains more information than the rDST.

Finally, data are further reduced by using *DaVinci* software package whose output is stored in nTuples, containing all the highest-level physics objects, and observables, which are needed to perform the final analysis.

2.11 Events Reconstruction

Particles trajectories, identification of the vertices, and identification of the type of the particles involved are the fundamental information to perform the final measurement.

2.11.1 Tracks Reconstruction

Track reconstruction starts by connecting the hits left by charged particles in the tracking subdetectors (VeLo, TT, IT and OT) to reconstruct their trajectory. By taking into account the effects of the magnetic field, it is also possible to estimate the momentum p of a particle, with charge q, through the bending (bend radius R) in the magnetic field according to:

$$R = \frac{p}{qB}$$

A track reconstructed in a subdetector is extrapolated in the other subdetectors and finally it is possible to link the resulting track to the calorimeter. Different type of tracks are distinguished in LHCB according to the subdetectors crossed, as shown in Figure 2.11:

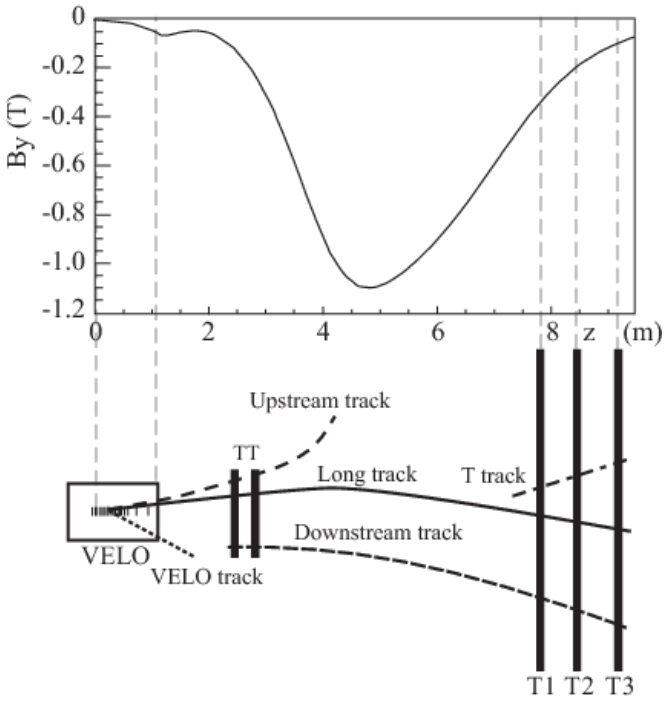

Figure 2.11: *Top* The magnetic field strength along the y-axis as function of z coordinate. *Bottom* Illustrator of the different type of tracks distinguished in LHCb [33].

- *VELO tracks* are tracks with only VELO hits. They are used in the primary vertex reconstruction and as seeds for reconstructing long and upstream tracks.

- *Upstream tracks* are low momentum tracks that transversed only the VELO and TT since they are bent out the LHCb acceptance by the magnetic field.
- *T tracks* are formed only using hits into the T-stations. They are used to form downstream and long tracks.
- *Downstream tracks* are reconstructed only in the TT and in the T-stations. They are useful to reconstruct the decays of long lived resonances that decay after the VELO.
- *Long tracks* require particles traversing the full tracking system. They are reconstructed combining hits from the VELO and the T-stations, and when possible hits from TT are added.

In our studies we considered data reconstructed using only *Long tracks*, *i.e.* tracks which cross all the tracking detectors, thus having the most precise momentum resolution and giving precise secondary vertices.

To reconstruct tracks, first of all the so-called seeds are searched, separately for Velo and a T station. Then seeds are associated to hits in the other tracking subsystems, to form tracks.

The magnetic field in the VeLo region is low enough to treat VeLo tracks as straight lines. Aligned clusters of hits in the VeLo sensors are used to reconstruct straight track segments that will be used as *VeLo seeds* in the pattern recognition algorithms. Moreover, particles which cross outer tracking stations are weakly bent by magnetic field, and using parabolic parametrization determined by MC studies it is possible to identify tracks derived from clusters of hits as *T seeds*.

Afterwards, a VeLo seed and, one by one, a hit in a T station are chosen. So it is possible to define a trajectory, and therefore other hits are looked for in the other T stations around the track candidate trajectory, including TT tracks. These hits are then fit by using the LHCb standard track parametrization. If the fit quality is good ($\chi^2/ndof < 5$), the sum of hits then is classified as a Long track. Finally, the hits already associated with tracks are removed from the list of hits on which the algorithm has to run.

This algorithm reconstructs about 90% of Long tracks. Another 5% of Long tracks are reconstructed by trying to match pairs of VeLo and T seeds, extrapolating hits in the magnet and requiring that the resulting fit has a good quality. It is of course possible for a physical track to be reconstructed by more than one algorithm, resulting in two clone tracks. In that case, only the best out of the two tracks is kept.

The momentum resolution depends on particle momentum ifself and varies from $\frac{\delta p}{p} = 0.35\%$ for low momentum tracks to $\frac{\delta p}{p} = 0.45\%$ for track having a momentum of the order of 100 GeV (Figure 2.12).

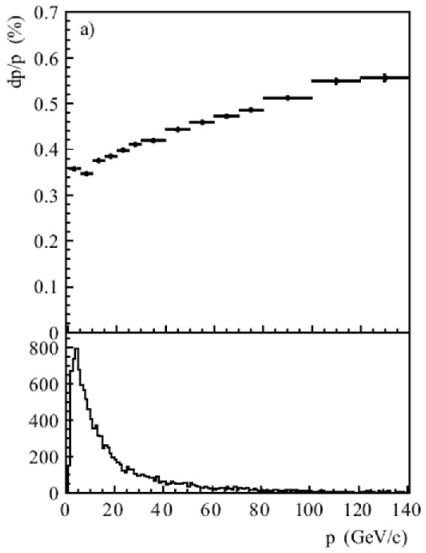

Figure 2.12: Momentum resolution (top) and momentum spectrum (bottom) for tracks from B decays.

2.11.2 Particles Identification

Neutral particles (π^0,γ,n,K^0_L) are trackless and are identified solely from their interaction in the calorimeters. Muons are identified from their interaction in the calorimeters and hits in muon chambers. Electrons are separated from hadrons by combining their calorimetric information. Finally, RICHs allow to separate $\pi^{\pm}$ and $K^{\pm}$.

In the analysis presented in this thesis, it is essential to unambiguously identify muons, charged pions, proton and kaons.

To determine the identity of a particle it is necessary to know its mass,

its charge and how it interacts with matter. The energy, the momentum and the charge of a particle can be measured with calorimeters and tracking (previous sections). However, to recover its mass, it is needed to know its velocity. In a particle physics experiment, it is very difficult to determine the velocity of a particle, since, typically, it is a large fraction of the speed of light and time-of-flight measurements would require sub-nanosecond time resolution. Thus, the Cherenkov effect is used.

The LHCb RICH detectors measure the angle θ_C of the Cherenkov cone by focusing the emitted light with a spherical mirror on the plane of photo-detectors. Then, the photons emitted along the trajectory of traversing particles will form a ring on photo-detector plane with the radius proportional to θ. The number of Cherenkov photon detected is proportional to $\sin\theta_C{}^2$. A ring on photo-detector is approximately elliptical with a degree of distorsion that depends on the track position and direction.

Pattern recognition algorithms are used to reconstruct the Cherenkov rings, and particularly they are based on maximum likelihood approach. In the first iteration, this method assumes a pion hypothesis for each reconstructed track since it is the most common particle type. A likelihood is calculated by comparing the expected pattern of photons to the observed pattern. Then, the particle hypotheses are varied one-by-one and the likelihood is recalculated, until the observed pattern matches best with the expected pattern. Figure 2.13 displays for both RICH detectors the observed photons with the reconstructed rings in a typical event. The muon detector is described in section 6.3.2. The muon system is used both in the Level-0 trigger (2.9.1) to select muons with a high transverse momentum p_T and in the offline reconstruction, *i.e.* through pattern recogniton algorithms, to identify muons. In the trigger algorithm, p_T muons are found by a fast and standalone track reconstruction, selecting particles which traverse all five muons stations. The slope of the track between M1 and M2 is used to estimate the momentum assuming that the particle originated from the interaction point. In the offline reconstruction, the muon system is used to identify the muons in the sample of tracks found in the tracking stations. The muon information

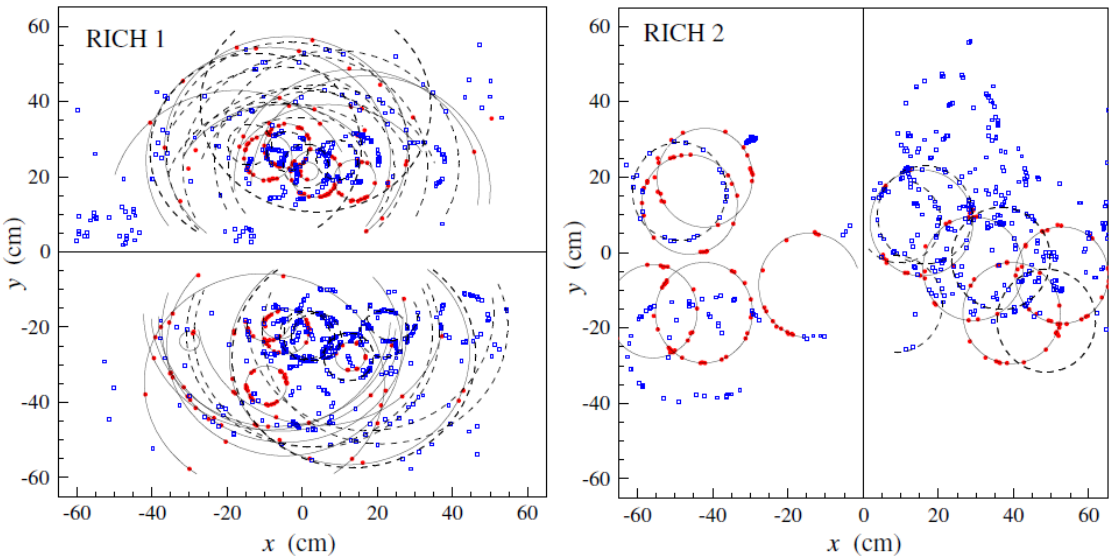

Figure 2.13: A typical event in the detection planes of RICH1 (left) and RICH2 (right). The horizontal (vertical) line separates the two detection planes in RICH1 (RICH2). Superimposed are the reconstructed rings for tracks which extend from the VELO up to the last T station(solid) and all other tracks(dashed).

is added using track segments from a T station that are propagated to the muon subdetector. The muon hypothesis is confirmed, if a $\chi^2/ndof < 5$ is obtained after fitting hits with the standard LHCb parametrization for a μ track.

The information is combined to provide the best achievable separation between the charged particles type (e, μ, K, π, p). A likelihood information for a particle hypothesis x is produced by each sub-system and added linearly in a combined likelihood $\mathcal{L}(x)$. Usually it is calculated relatively to the pions hypotesis, since pions are the most abundant species produced and detected at LHCb. At LHCb, a way to separate particle types and to improve the purity of the sample, is applied a cut on the logarithm of the likelihood ratio (DLL) between different hypotheses:

$$\Delta \ln \mathcal{L}_{x\pi} = \ln \mathcal{L}(x) - \ln \mathcal{L}(\pi) = \ln \frac{\mathcal{L}(x)}{\mathcal{L}(\pi)} \tag{2.1}$$

An efficient $\pi - K$ separation is achieved by using this method. To calculate the identification efficiency and mis-identification probability pure sam-

ples of pion and kaons are required. In figure 2.14 it is possible to observe different efficiencies for different DLL cuts.

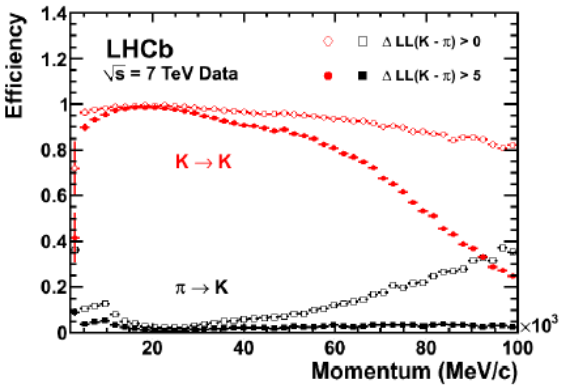

Figure 2.14: Identification and misidentification efficiencies for kaons as a function of momentum. The solid markers are for DLL$>$ 0 and the hollow markers are for DLL$>$ 5.

The other way to separate the particles types is by means of ProbNN variables. They are the outputs of neural network based classifiers that additionally take into account other track properties such as the tracking performance or the track kinematics. Apart from better performance, also offer the practical advantage of being defined as an absolute probability, as opposed to the log-likelihoods which always compare two competing hypothes 2.15

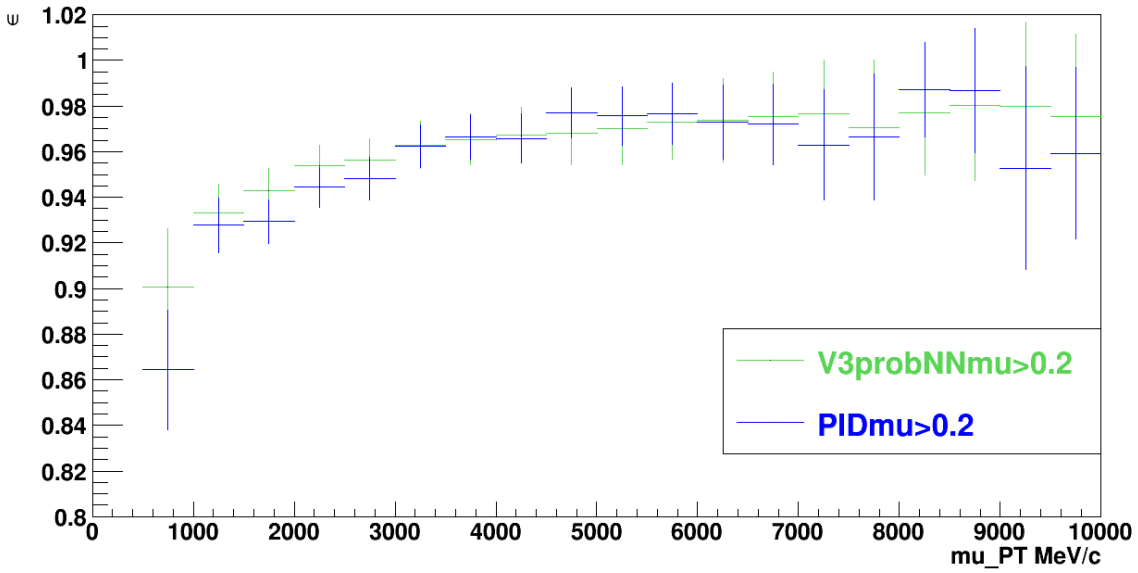

Figure 2.15: Efficiency of $PID\mu$ and $ProbNN\mu$ cut calculated on MC($\Lambda_b^0 \to \Lambda_c \mu^- \bar{\nu}_\mu$).

Chapter 3

Samples and selections

This chapter introduces the data and simulation samples used for the $R(\Lambda_c^*)$ measurement.

3.1 Topology of signal and normalization decays

The $R(\Lambda_c^*)$ analysis presented in this thesis used a sample of proton-proton collision data corresponding to $2fb^{-1}$ of integrated luminosity, recorded by LHCb during 2012 at the center of mass energy of $\sqrt{s} = 8$ TeV. During the data taking the polarity of LHCb magnet was flipped several time, in order to minimize possible systematic biases due to detector asymmetries.
The aim of this analysis is the measurement of the ratio $R(\Lambda_c^*) \equiv \frac{\mathcal{B}(\Lambda_b^0 \to \Lambda_c^* \tau^- \bar{\nu}_\tau)}{\mathcal{B}(\Lambda_b^0 \to \Lambda_c^* \mu^- \bar{\nu}_\mu)}$ and therefore the $\Lambda_b^0 \to \Lambda_c^* \tau^- \bar{\nu}_\tau$ and the $\Lambda_b^0 \to \Lambda_c^* \mu^- \bar{\nu}_\mu$ decay modes, where $\Lambda_c^* \equiv \Lambda_c^+(2595, 2625)$, are searched.
Only muonic decays of τ are considered, $\tau^- \to \mu^- \bar{\nu}_\mu \nu_\tau$, the $\Lambda_c^+(2595)$ and $\Lambda_c^+(2625)$ baryons are reconstructed in the $\Lambda_c^{*+} \to \Lambda_c^+ \pi^+ \pi^-$ decay mode, and finally the Λ_c^+ is searched according to its predominantly decay mode $\Lambda_c^+ \to pK^-\pi^+$. As you can see in Fig.3.1 the Λ_c^{*+} decay can occur also through the $\Lambda_c^{*+} \to \Sigma_c(2455)^{++}(\to \Lambda_c^+ \pi)\pi^-$ or $\Lambda_c^{*+} \to \Sigma_c(2455)^0(\to \Lambda_c^+ \pi)\pi^+$. Charge-conjugated decay modes are implied throughout the thesis, unless otherwise specified. The signal decays, $\Lambda_b^0 \to \Lambda_c^{*+} \tau^- \bar{\nu}_\tau$, and the normalization channel, $\Lambda_b^0 \to \Lambda_c^{*+} \mu^- \bar{\nu}_\mu$, produce identical visible particles in the final states, therefore the relative efficiencies of the two channels depends only on the differing kinematics and the reconstruction; particles identification and tracking effi-

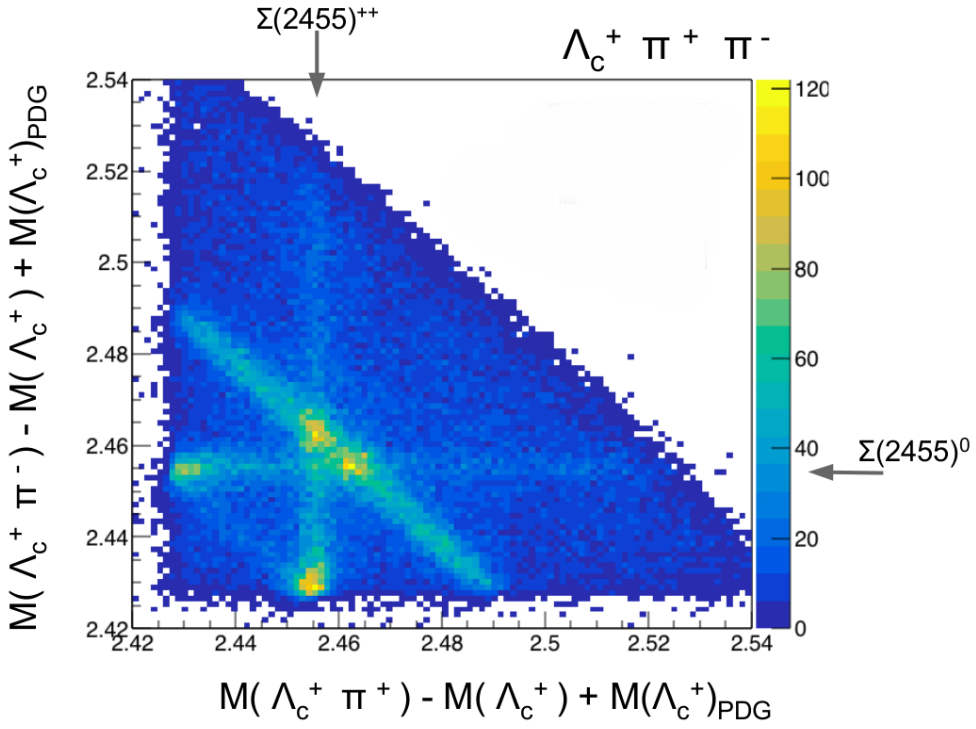

Figure 3.1: Dalitz plot of $\Lambda_c^{*+} \to \Lambda_c^+ \pi^+ \pi^-$ decay.

ciencies cancel to first order.

In high-energy collisions, the produced b or $\bar{b}$ quarks can hadronize with different probabilities into the full spectrum of b-hadrons, either in their ground or excited states, in particular, their hadronization fraction in Λ_b^0 about 14%. The signal decays, $\Lambda_b^0 \to \Lambda_c^{*+} \tau^- \bar{\nu}_\tau$, and normalization channel decays, $\Lambda_b^0 \to \Lambda_c^{*+} \mu^- \bar{\nu}_\mu$, exploit the excellent capabilities of the LHCb detector concerning momentum, impact parameter resolution and particles identification.

In Fig.3.2 the topology of the these decays is shown. The main feature of these channels is that they decay semileptonically, and so, due the lack of neutrino tracks, the reconstructed Λ_b^0 momentum doesn't point back to the Primary Vertex (PV). Therefore, the b hadron kinematics can not be con-

strained, also due to unknown parton-parton collision energies. A estimation of b hadron momentum can be obtained through approximations or multivariate technique approaches, as described in the following chapter. With respect to other channels, like $\bar{B}^0 \to D^{*+}\tau^-\bar{\nu}_\tau$, the advantage of our channel is that, thanks to resonance Λ_c^{*+} which decays hadronically, the Λ_b^0 vertex can be found with a very good quality.
The lifetime of Λ_b^0 baryons lifetime is large enough to allow them to fly on average about 1 cm before decaying. Also τ and Λ_c^+ decay displaced with respect to Λ_b^0 vertex, unlike $\Lambda_c^+(2625)$ and $\Lambda_c^+(2595)$ resonances. These peculiarities help us to identify the searched channel: large impact parameters (IP) of the reconstructed tracks, displaced vertices with good qualities and a long track associated with a candidate in the muon station.
Finally, b hadrons are identified using LHCb PID system, section 2.11.2.
As the neutrinos can not be reconstructed, the $\Lambda_b^0 \to \Lambda_c^*\tau^-\bar{\nu}_\tau$ and $\Lambda_b^0 \to \Lambda_c^*\mu^-\bar{\nu}_\mu$ decays can only be selected along with all other Λ_b^0 decays producing $\Lambda_c^*\mu^-\bar{X}$ final state, where X is any combination of particles. A number of Λ_b^0 decays can therefore generate a background, in particular $\Lambda_b^0 \to \Lambda_c^* D^{(*)}$ and $\Lambda_b^0 \to \Lambda_c^* D_s^{(*)}$. In contrast with single neutrino in $\Lambda_b^0 \to \Lambda_c^*\mu^-\bar{\nu}_\mu$, the combination of the multiple neutrinos in the $\Lambda_b^0 \to \Lambda_c^*\tau^-\bar{\nu}_\tau$ can have large masses. This state can occur also in the Λ_b^0 decays producing $\Lambda_c^*\mu^-\bar{X}$ decay, and therefore an other challenge about this measurement is to separate double charm from semitauonic decays.

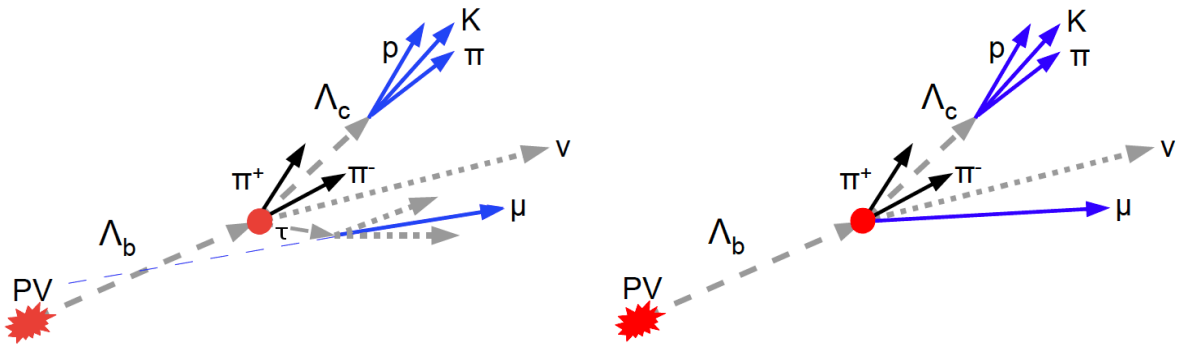

(a) $\Lambda_b^0 \to \Lambda_c^*\tau^-\bar{\nu}_\tau$ (b) $\Lambda_b^0 \to \Lambda_c^*\mu^-\bar{\nu}_\mu$

Figure 3.2: $\Lambda_b^0 \to \Lambda_c^*\tau^-\bar{\nu}_\tau$ (Left) and $\Lambda_b^0 \to \Lambda_c^*\mu^-\bar{\nu}_\mu$(Right) decay topology

3.1.1 Relevant quantities

It is useful to define some relevant quantities used in the analysis. All quantities are calculated in the laboratory frame, and in general, can be applied to each particle in the decay.

- Primary vertex (PV): the point of the space where the primary pp interaction is reconstructed;
- Secondary decay vertex (SV): the point in the space where the decay of long-lived particles occurs. The displacement vector $\vec{d}$, defined as the spatial vector from primary to second vertex, is equal to $\vec{d} = \gamma\vec{\beta}ct = (\vec{p}/m)ct$, where c is the speed of light, m the mass, $\vec{p}$ is momentum and t the proper time decay of the decay particle.
- Impact Parameter (IP): given a vertex $\vec{v}$, the impact parameter is the vector formed by the nearest point of a track to $\vec{v}$. The muons frOm $\Lambda_b^0 \to \Lambda_c^{*+}\tau^-\bar{\nu}_\tau$ tend to have a large impact parameter with respect to Λ_b^0 decay vertex.
- DIRA: the cosine of angle between the momentum of the particle $\vec{p}$ and the displacement vector, $DIRA = \vec{p}\cdot\vec{d}/|\vec{p}||\vec{d}|$. For a fully reconstructed particle its total momentum tends to be aligned to the displacement vector resulting into a DIRA close to unit, differently for one partially reconstructed, like semileptonic decay.
- χ^2-distance: the distance between two spatial points in χ^2 units.
- MIN(χ^2_{PV}): requires the minimum χ^2 distance of a particle to PV. MIN(χ^2_{PV})$>$ 9 corresponds to require that the particle is 3σ away from any PV.
- χ^2_{IP}: the χ^2_{IP} for a particle is defined as the difference in χ^2 of the primary vertex fit with and without considering the particle in the fit.
- χ^2_{track}: the track is reconstructed by minimizing the χ^2 of the fit from the hints in the detectors. Small χ^2_{track} ensures an agreement between the track model and the reality.

- χ^2_{vtx}: it applies a χ^2 cut to the vertex of the particle.
- P(ghost): the ghost probability is a multivariate classifier based on kinematics variables and track reconstruction parameters as input, to identify reconstructed tracks which not correspond to a real particle.
- Δm: is the absolute difference between the measured mass and the PDG reference value.
- DOCA,χ^2_{DOCA}: it is the distance of closest approach in unit of χ^2 between the trajectories of two particles. Particles coming from a decay of a common mother particle are likely close to each other translating into a small DOCA.

3.2 Central Offline Selection

The events reconstruction and a loose preselection of candidates, named "stripping" inside the LHCb collaboration, are centrally done in order to reduce the datasets to manageable size. According to the signal of interest, different sets of cuts are applied and grouped in the so called, stripping lines. The relevant stripping lines for the measurement reported in this thesis is b2LcMuXB2DMuNuXLine, whose requirements are summarized in Table 3.1. This line allows us to identify the $\Lambda_b^0 \to \Lambda_c \mu^- \bar{\nu}_\mu$ decays but for R(Λ_c^*) measurement it is necessary to reconstruct the Λ_b^0 channels which decays in $\Lambda_c^+(2625)\mu^-\bar{\nu}_\mu$ final states, therefore, in own offline selection, two pions are added to Λ_c vertex in order to form the $\Lambda_c^{*+} \to \Lambda_c^+ \pi^+ \pi^-$ decay candidates. The cuts cited in the following rows are described in sub-sec 3.1.1.

In the b2LcMuXB2DMuNuXLine to identified proton, pion and kaon, it is required a good quality of tracks ($\chi^2_{track}/\text{ndf} < 5$), a momentum threshold ($p_T > 300$ MeV/c and p>2 GeV/c) and that their vertex is displaced with respect to PV (MIN(χ^2_{PV}) > 9). Similar cuts are also applied to identify a muonic track, in particular $p > 3$ GeV/c,p_T>800 MeV/c and MIN(χ^2_{PV}) > 4 is required. The P(ghost)<0.5 guarantees to identify tracks which corresponds to real particles. Finally, to suppress mis-reconstructed backgrounds, particles

identification (PID) requirements are applied to the the p,π,K tracks through the $DLL_{K\pi}$ variable and to the muon through the $DLL_{\mu\pi}$. As described in subsection 2.11.2, positively larger values of the $DLL_{particle\pi}$ corresponds to an higher probability to be a that particle, and viceversa, negatively lower values to a pion. Moreover, for a proton candidate $DLL_{p\pi} - DLL_{K\pi} > 10^{-10}$ is required.

Λ_c candidates are then formed combining three charged particles identified as a proton, pion and K.The Λ_c candidates are then combined with muons to form the Λ_b^0. It is required the mass of reconstructed particle is different from PDG reference value of less that 80 MeV, a cut on the sum of transverse momentum of daughters (> 1800 MeV/c), a good quality vertex ($\chi^2_{vtx}/\text{ndf} < 6$ and $\chi^2_{distance-PV} > 10$ and DOCA < 9) and finally, since it is a fully reconstructed decay the DIRA is required to be close to unit.

The Λ_c candidates are then combined with muons to form the Λ_b^0 in the mass interval [2.5,6] GeV. A good distance of closest approach between the trajectories of two candidates is asked (DIRA > 0.999), together requirements on vertex quality ($\chi^2_{vtx}/\text{ndf} < 6$, $z(\Lambda_c^{\pm}) - z(\Lambda_b^0) > 0$ mm).

3.3 Trigger Selection

The trigger system decides whether an event is interesting for physics analysis and in that case, all detector hits and informations are saved. Each trigger line refers to a sequence of reconstructed and selection algorithms to trigger an event. According the specific signature, an event can be acquired because of the positive trigger decision of a trigger line of another. Selected signal event can be classified as:

- Triggered On Signal (TOS), if the signal candidate or its daughters cause the event to be triggered;
- Triggered Independently of Signal (TIS), when a positive trigger decision is due to tracks in the event independent of signal decay chain;

Table 3.1: Summary of the stripping requirements

Candidate	Requirement
$\mu^{\pm}$	$\chi^2_{track}/\text{ndf} < 5$ $p_T > 800$ MeV/c $p > 3$ GeV/c $P(ghost) < 0.5$ MIN$(\chi^2_{PV}) > 4$ $DLL_{\mu\pi} > 0$
$K^{\pm}$	$\chi^2_{track}/\text{ndf} < 4$ $p_T > 300$ MeV/c $p > 2$ GeV/c $P(ghost) < 0.5$ MIN$(\chi^2_{PV}) > 9$ $DLL_{K\pi} > 4$

Candidate	Requirement
$\pi^{\pm}$	$\chi^2_{track}/\text{ndf} < 4$ $p_T > 300$ MeV/c $p > 2$ GeV/c $P(ghost) < 0.5$ MIN$(\chi^2_{PV}) > 9$ $DLL_{K\pi} < 10$
$p^{\pm}$	$\chi^2_{track}/\text{ndf} < 4$ $p_T > 300$ MeV/c $p > 2$ GeV/c MIN$(\chi^2_{PV}) > 9$ $DLL_{p\pi} > 4$ $DLL_{p\pi} - DLL_{K\pi} > 10^{-10}$

Candidate	Requirement
$\Lambda_c^{\pm}$	$\Delta m < 80$ MeV $\sum p_T$ daughters > 1800 MeV/c $\chi^2_{vtx}/\text{ndf} < 6$ DOCA < 9 DIRA > 0.99 $\chi^2_{distance-PV} > 10$
Λ_b^0	M $\subset [2.5, 6]$ GeV $\chi^2_{vtx}/\text{ndf} < 6$ $z(\Lambda_c^{\pm}) - z(\Lambda_b^0) > 0$ mm DIRA > 0.999

- TIS & TOS simultaneously.

The LHCb trigger as described in section 2.9 consists of a L0 hardware trigger, which is subdivided into Muon, Dimuon, Electron, Hadron and Photon lines, and a software-based HLT trigger divided in HLT1 and HLT2, comprising selections of decay channels or classes of decay. The trigger selection used in this analysis is:

- **L0 level**:
  Λ_b^0_L0HadronDecision_TOS or Λ_b^0_L0HadronDecision_TIS
  or Λ_b^0_L0MuonDecision_TOS or Λ_b^0_L0MuonDecision_TIS;

- **HLT1 level**:
  Λ_b^0_Hlt1TrackMuonDecision_TOS or Λ_b^0_Hlt1TrackMuonDecision_TIS
  or Λ_b^0_Hlt1TrackAllL0Decision_TOS or Λ_b^0_Hlt1TrackAllL0Decision_TIS;

- **HLT2 level**:
  Λ_b^0_Hlt2TopoMu2BodyBBDTDecision_TOS
  or Λ_b^0_Hlt2TopoMu3BodyBBDTDecision_TOS
  or Λ_b^0_Hlt2TopoMu4BodyBBDTDecision_TOS
  or Λ_b^0_Hlt2SingleMuonDecision_TOS;
  or Λ_b^0_Hlt2CharmHadLambdaC2PiPKDecision_TOS;

The Λ_b^0_Hlt2CharmHadLambdaC2PiPKDecisionLine, has been written during 2011 data taking, and therefore, was not applicable to 2011 dataset. For this reason, the analysis is performed only on 2012 dataset. Other lines have not been changed during 2011 and 2012 data taking.
All Λ_b^0 candidates anayzed are required to fulfill the previous trigger conditions.

3.3.1 Low Level Lines

For every Λ_b^0 candidate in this analysis is required to pass one of Λ_b^0_L0Hadron Decision_TOS line, Λ_b^0_L0HadronDecision_TIS line, Λ_b^0_L0MuonDecision_ TOS line or Λ_b^0_L0MuonDecision_TIS line. These lines triggers on high transverse momentum muons (L0Muons) and on large transverse energy deposition (L0Hadron) in the calorimeters. A relative momentum resolution of about 20 % can be reached in the L0 muon reconstruction. In Table 3.2 are given the threshold applied in L0 level to give a positive trigger.

Table 3.2: L0 thresholds in 2011 and 2012 [34]

L0MuonDecision	1.76 GeV
L0HadronDecision	3.7 GeV

3.3.2 High Level Trigger, first Stage

In the first stage of high level trigger a partial event reconstruction and inclusive selection of signal are performed. The recostruction starts by track segments in the vertex detector. High IP track segments and track segments that can be matched with hints in the muon chambers are then extrapolated into the main tracked. A Λ_b^0 candidate in this analysis, has to exceed the

HLT1TrackMuonDecision or Hlt1TrackAllL0Decision lines (TIS,TOS). The Hlt1TrackAllL0Decision is designed to select hadron decays which are significantly displaced from a PV and for which al least one decay particle is characterized by $p_T < 1.6$ GeV . The HLT1TrackMuonDecision, then, accepts events with a muon candidates that have an $IP > 0.1$ mm with respect to all PVs, and with a $p_T > 1$ GeV.

3.3.3 High Level Trigger, second Stage

The second level trigger stage, HLT2, performs a full event reconstruction for all tracks with a minimum p_T of 500 MeV [34].

3.3.3.1 The HLT2 topological trigger lines

The so called topological trigger lines are designed to trigger on partially reconstructed b-hadrons, with al least two charged particles in the final state and with a displaced vertex. They are formed using a multivariate inclusive selection based on two, three or four prong vertices. A Boost Decision Tree classifier is used. Input particles are selected by applying IP and track quality cuts to reconstructed tracks. From these input particles two body combinations are created and used as input to multivariate selection. Three and four body combinations are created by incrementally adding tracks to the two body combinations. The variable used in the BDT are: the sum of the absolute p_T of all decay tracks, the minimum momentum, the invariant mass, the Distance Of Closest Approach (DOCA), the impact parameter (IP) and flight distance χ^2 of the candidates, and finally the corrected mass. The latter is given by [35]

$$M_{corr} = \sqrt{M^2 + |p_{T,miss}|^2} + |p_{T,miss}| \tag{3.1}$$

where m is the invariant mass of the reconstructed n-body system and $p_{T,miss}$ is the missing momentum transverse to the flight direction of b-hadron candidate (see Fig.3.3).

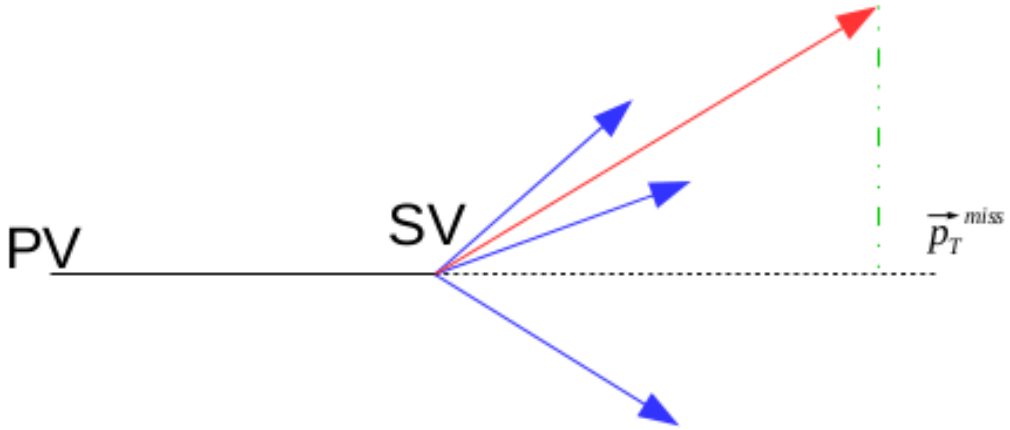

Figure 3.3: The definition of p_T^{miss}.

3.3.3.2 Hlt2SingleMuon Trigger Line

The purpose of the Line Hlt2SingleMuon is to select one identified muon combined with one or more additional tracks. Semileptonic decays can be triggered with a detached single muon trigger without imposing a bias on the hadronic part of the events. To reduce the amount of single muon events, it requires that the trigger candidate itself had triggered HLT1TrackMuon selection. Additionally a very good track quality, a reasonable high p_T and a large muon IP are requested (see Table 3.3) . The p_T is kept low not to introduce a bias on the hadronic part of semileptonic decays.

3.3.3.3 Hlt2CharmHadLambdaC2PiPK Trigger Line

The Hlt2CharmHadLambdaC2PiPK aim is to select $\Lambda_c^{*+} \to \Lambda_c^+\pi^+\pi^-$. Λ_c candidates are built without particle identification information extracted from RICHEes and, after a sizable amount of events have been filtered by this first selection, also the RICH reconstruction is triggered. The final candidates are then built according the selection shown in Table 3.4.

Applying the topological trigger appears a shift in the visible mass and corrected mass distribution of $\Lambda_b^0 \to \Lambda_c^{*+}\tau^-\bar{\nu}_\tau$, without the same correspondence for $\Lambda_b^0 \to \Lambda_c^{*+}\mu^-\bar{\nu}_\mu$. In fact, the topological triggers places a requirement on the output of the MVA which gives higher output values for

Table 3.3: Hlt2SingleMuon trigger requirements [36]

Quantity	Requirement
μ p_T	$>$ 1.3 GeV/c
μ χ^2_{track}	$<$ 2
μ IP	$>$0.5 mm
μ χ^2_{IP}	$>$ 200

Table 3.4: Hlt2CharmHadLambdaC2PiPK trigger requirements [36]

Candidate	Quantity	Requirement
$K^{\pm}, \pi^{\pm}$	χ^2_{track}/ndf	$<$ 3
	p_T	$>$ 500 MeV/c
	χ^2	$>$ 9
$p^{\pm}$	χ^2_{track}/ndf	$<$ 3
	p_T	$>$ 1500 MeV/c
	largest child χ^2_{IP}	$>$ 15
	M	[2211,2361] MeV/c^2
$\Lambda_c^{\pm}$	χ^2_{vtx}/ndf	$<$ 15
	χ^2_{SV}	$>$ 49
	SV	$<$4 mm
	DIRA	$>$ 0.99985
	lifetime	$<$ 0.02 ps
	HLT1 TOS	Hlt1track
	p	$>$ 10000 MeV/c
	χ^2_{IP}	$>$ 9
	PIDp	$>$ 0
$h^-p^+h^+$ combination	$\sum p_T$	$>$ 2500 MeV/c
	largest child χ^2_{IP}	$>$ 15
	M	[2211,2361] MeV/c^2
$\Lambda_c^{\pm}$	χ^2_{vtx}/ndf	$<$ 15
	χ^2_{SV}	$>$ 49
	SV	$<$4 mm
	DIRA	$>$ 0.99985
	lifetime	$<$ 0.02 ps
	HLT1 TOS	Hlt1track

candidates with higher visible mass, corrected mass, and track traverse momentum. However, we decided to use a combination of the previous described trigger lines to increase the statistic of our simulated samples, since using only the Charm trigger configuration, it decreased by half (see Table 3.4).

3.4 Further Offline selection

The b2LcMuXB2DMuNuXLine stripping, described in sub-sec.3.2, allows us to identify the $\Lambda_b^0 \to \Lambda_c \mu^- \bar{\nu}_\mu$ decays, but for R(Λ_c^*) measurement it is necessary to reconstruct the Λ_b^0 channels which decays in $\Lambda_c^+(2625)\mu^-\bar{\nu}_\mu$ final states, therefore, two pions have been added to Λ_c vertex in order to form the $\Lambda_c^{*+} \to \Lambda_c^+ \pi^+ \pi^-$ decay candidates. To the latter a minimum transverse momentum ($\pi^\pm\_p_T > 250$ MeV/c) and to form a good Λ_c^* vertex have been required.
The loose stripping selection has to be refined with a group of tighter requirements in order to reconstruct the $\Lambda_b^0 \to \Lambda_c^{*+}\mu^-\bar{\nu}_\mu$ and $\Lambda_b^0 \to \Lambda_c^{*+}\tau^-\bar{\nu}_\tau$ decays, minimizing the backgrounds.
In particular, the Λ_c decay distance is required to have a χ^2 >100 and a impact parameter with respect to Λ_c^* vertex < 7.4 mm, considering that this baryon decays after about 1 cm with respect to the Λ_b^0. Moreover, it is required a Λ_c mass in the range [2.25,2.335] GeV/c^2, and characterized by a mass within 50 MeV/c^2 of the nominal mass. The sum of the transverse momentum of Λ_c daughters, p,K,π has to be greater than 2100 MeV/c and each one has to have a impact parameter χ^2 with respect mother greater than 9. To further suppress the contamination from misidentified events a ProbNNk > 0.2 and ProbNNghost < 0.6 cuts are also applied to p,K,π from Λ_c (sec.2.11.2). In Figure 3.4, it is shown the Λ_c mass distribution after the offline selection.

To reconstruct the Λ_c^*, a Λ_c and two charged pions are fitted to a common vertex which is required to have χ^2_{vtx}/ndf < 7. Moreover, it is required a Λ_c^* mass in the range [2.3,2.8] GeV/c^2, and characterized by a mass within 400 MeV/c^2 of the nominal mass. Then, a cut on $\pi^\pm$_ProbNNe < 0.4 and $\pi^\pm$_ProbNNghost < 0.6, to reduce the probability to misidentify a pion with an electron or with a non real track. The Figure 3.4 shows the distribution of $\Delta m = M(\Lambda_c^*) - M(\Lambda_c)$, before and after the offline selection. It is possible to notice two peaks which correspond respetively to Λ_c^* resonances defined

by a mass of 2595 MeV/c^2 and 2625 MeV/c^2. In this thesis, only the decays of $\Lambda_c(2625)$ has been considered due to statistics, but in all fits to Δm in the following chapters both of resonances are considered, in order to perform a correct evaluation of combinational background shapes.

Finally, to reconstruct a Λ_b^0, Λ_c^* and a muon has to form a vertex with $\chi^2_{vtx}/\text{ndf} < 16$ and a mass less than 6.5 GeV/c^2. A cut to decrease the muon misidentification is applied (μ_ProbNN$\mu > 0.2$) and the Λ_b^0 is required to point to the primary vertex with a DIRA > 0.999. The fully list of requirements is reported in Table 3.5.

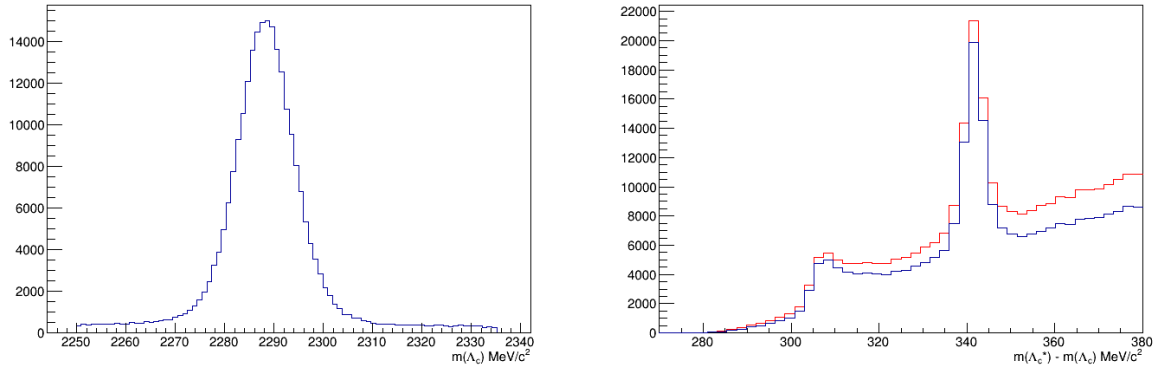

(a) (b)

Figure 3.4: (a) Λ_c mass distribution after the offline selection, (b)The distribution of $\Delta m = M(\Lambda_c^*) - M(\Lambda_c)$, before(red) and after(blu) the offline selection.

3.5 Monte Carlo Simulations

Numerical simulations are indispensable to take into account for predicting the complex effects associated to the detector response and to estimate the efficiencies. The algorithm used involve random sampling to simulate processes and are collectively called Monte Carlo (MC) simulation. The simulation involves several steps in order to describe the *pp* collisions, decay precesses, detector response and data processing and selection. The PYTHIA package [37] models the *pp* collision environment, the outgoing quarks and gluon collision products. Moreover it simulates the fragmentation and hadroniza-

Table 3.5: Summary of offline selection requirements, h= p,K,π derived by Λ_c decay

Candidate	Requirement
$\Lambda_c^{\pm}$	M $\subset [2.25, 2.335]$ GeV/c^2
	M(Λ_c^+)$_{reco}$ - M(Λ_c^+)$_{PDG}$ $<$ 50 MeV/c^2
	$\chi^2_{FlightDistance} > 100$
	IP wrt Λ_c^* vtx $<$ 7.4 mm
	$\sum p_T$ daughters $>$ 2100 MeV/c
	h_ProbNNk $>$ 0.2
	$\pi^{\pm}$_ProbNNghost $<$ 0.6
	h_ProbNNghost $<$ 0.6
	h_χ^2_{track}/ndf $<$ 5
	h_$\chi^2_{IPwrt\Lambda_c vtx} > 9$
Λ_c^*	M $\subset [2.3, 2.8]$ GeV/c^2
	M(Λ_c^*) - M(Λ_c^+) $<$ 400 MeV/c^2
	$\pi^{\pm}$_ProbNNe $<$ 0.4
	$\pi^{\pm}$_ProbNNghost $<$ 0.6
	$\pi^{\pm}$_p_T $>$ 250 MeV/c
	$\pi^{\pm}$_MIN(χ^2_{PV}) > 9
	χ^2_{vtx}/ndf $<$ 7
Λ_b^0	M $<$ 6.5 GeV/c^2
	μ_ProbNNμ $>$ 0.2
	χ^2_{vtx}/ndf $<$ 16
	DIRA $>$ 0.999

tion which produce hadrons and jets. EVTGEN package [38] simulates the time evolution and the decay of hadrons. Afterward, GEANT4 toolkit [39] is responsible to model the interaction of decay products with the material. Finally, the detector response is determined from the interaction of detector with the material and used as input for the trigger decision, track reconstruction, central offline analysis and selection. In this analysis, MC samples which reproduce $\Lambda_b^0 \to \Lambda_c^* \mu^- \bar{\nu}_\mu$, $\Lambda_b^0 \to \Lambda_c^* \tau^- \bar{\nu}_\tau$, $\Lambda_b^0 \to \Lambda_c^* D_s$ and $\Lambda_b^0 \to \Lambda_c^* D_{(s)}^{(*)}$ decays are generated. Events corresponding to LHCb environment and detector conditions in 2012 are simulated. The samples and the number of events generated are listed in Table 3.6.

As described in chapter 1, the form factors which allow to describe the hadron current of $\Lambda_b^0 \to \Lambda_c^* l^- \bar{\nu}_l$, have never been measured. In order to generate MC samples it has been used the non relativistic quark model calculation performed by Pervin et al, described in [21]. In the early stages of analysis, we produced small size MC samples simulating all decays of $\Lambda_b^0 \to \Lambda_c^* D_s$,

$\Lambda_b^0 \to \Lambda_c^* D_s^*$. From these productions we estimated that, after applying the online and offiline selection the fraction of muon derived by D_s semileptonic decays was about the 90%, that the one from tauonic decays was about the 8% and that the residual were produced from decay of pions and kaons. Therefore, since in this thesis, the background due to muons misidentification is studied on a wrong charge data sample, we produced double charm MC samples decaying only as semileptonic channel. Thanks to first MC samples, we studied also the $\Lambda_b^0 \to \Lambda_c^* D^{(*)}$ decays. It is expected that they occur 20 time less than D_s corresponding decays, due to Cabibbo suppression. The most important variables used in this analysis, and described in chapter 4, are the missing mass square, the transferred momentum and energy of muon calculated in the Λ_b^0 center of mass energy. The distributions of these variables for the $\Lambda_b^0 \to \Lambda_c^* D_s^*$ and $\Lambda_b^0 \to \Lambda_c^* D^*$ decays, resulted overlapped, so we decided to simulate only the strange decays.

Table 3.6: number of MC generated events (magnet polarity up and down)

Sample	Data size
$\Lambda_b^0 \to \Lambda_c^* \mu^- \bar{\nu}_\mu$	10M
$\Lambda_b^0 \to \Lambda_c^* \tau^- \bar{\nu}_\tau$	7.5M
$\Lambda_b^0 \to \Lambda_c^* D_s$	15M
$\Lambda_b^0 \to \Lambda_c^* D_s*$	15M

3.5.1 MC reweighting: Particle Identification

The simulation of the detectors devoted to PID is non-trivial. Indeed, computing the response of these detectors to a traversing particle requires modeling of the kinematics of the particle, the occupancy of the detectors which may be different from event to event and sensitive to beam conditions, and the experimental conditions such as alignments,temperature, and gas pressure which may modify the response of detectors from run to run [40]. Therefore, the distributions of the particles identification variables are not simulated to a sufficient precision. This leads to wrong result when measuring the efficiency of PID cuts on simulated data ad obviously to different distributions of PID variables calculated using the MC samples compared with data.

Because of this, a data driven method is used to optimize the selection and calculate the efficiencies, using a calibration data sample. These methods make use of the fact that in a simulated sample, where the true particle ID of a track is known and the same for all events, the distribution of the PID response can be approximated as a function of the true particle type, the track rapidity (η) , the track momentum (p) and the event multiplicity. The calibrations of pions and kaons come from a sample of $D^* \to D^0(\to K\pi)\pi$, that one of protons form $\Lambda \to p\pi$ decays and finally the ones of muons are derived by $J/\psi \to \mu\mu$. Practically, the PID efficiency for every PID requirement as a function of kinematic variables pseudorapidity and track momentum is calculated. The track multiplicity is not considered since it is know that MC does not correctly reproduce the correspondent distribution. In figure 3.5 it is possible to see the 2D plot for each pid cut applied in selection.

3.5.1.1 MCTuneV2 and MCTuneV3

As said in section 2.11.2, the ProbNN variables are the output of a neural network based on classifiers that additionally take into account other track properties such as the tracking performance or the track kinematics. The training is done using MC inclusive B events and the performance depends on the tuning, the blending of MC, used. For general purposes MCTuneV2 and MCTuneV3 are available. The main difference is that the ghosts in the second one has been removed from the background of all the networks excluding the ghost itself. In our analysis it is fundamental to have the maximum performance for muon identification, so both of tuning are tested for $ProbNN\mu$ variables. Moreover, different cuts are evaluated as a function of μ_p_T to determine the configuration which allows to obtain higher cuts efficiencies as shown in Figure 3.6. It corresponds to ProbNNμ_MCTuneV3 > 0.2.

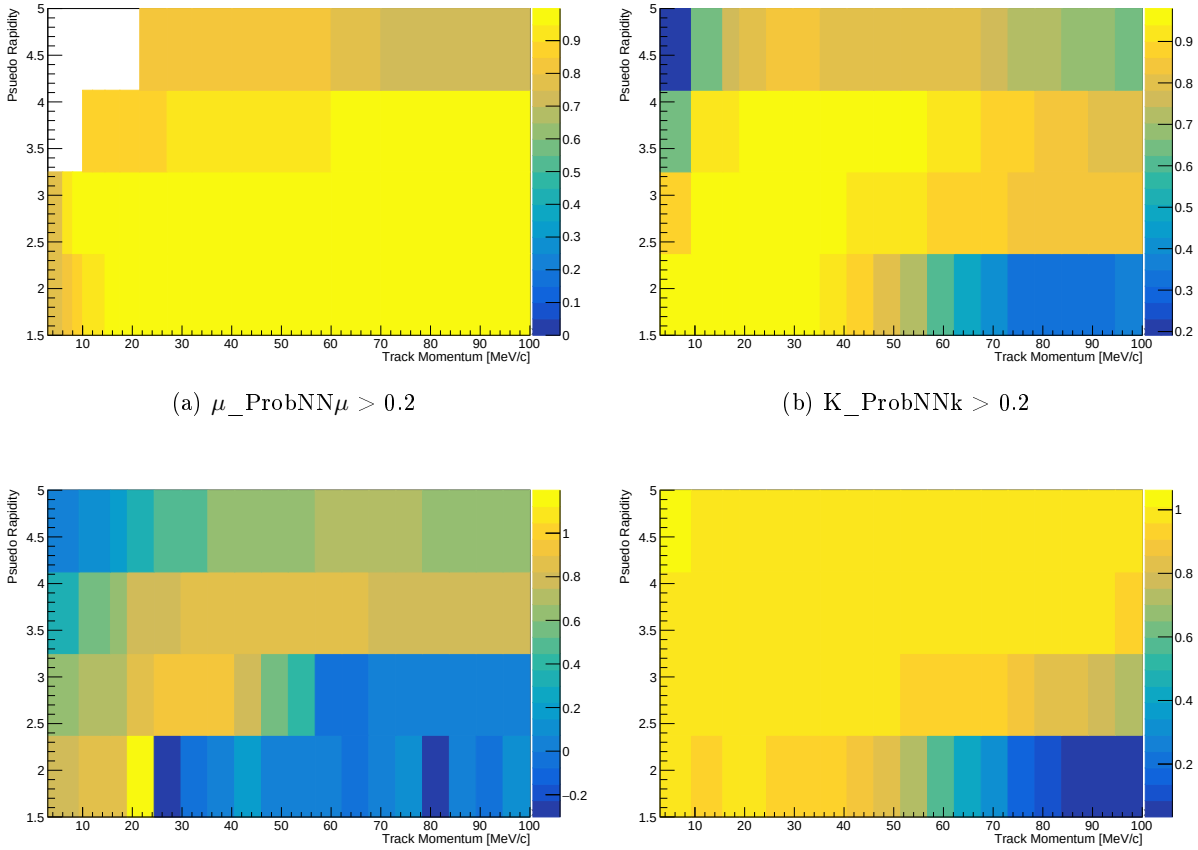

(a) μ_ProbNN$\mu > 0.2$

(b) K_ProbNNk > 0.2

(c) p_ProbNNp > 0.2

(d) π_ProbNN$\pi > 0.2$ and π_ProbNNe<0.4

Figure 3.5: Calibration Histograms to reweight MC PID variables.

3.6 Combinatorial background

The contribution to combinatorial background due to Λ_c^* fake has been modeled using the data sideband in the Δm ($\Delta m = M(\Lambda_c^*) - M(\Lambda_c)$) interval $\Delta m \in [360, 380]$.

The background due to Λ_c^* true associated with fake muon, contribution derived by muon misidentification, is instead modelled using a "wrong charge" data sample of $\Lambda_c^{*+}\mu^+$. Both of combinatorial background contribution are described in detail in chapter 5.

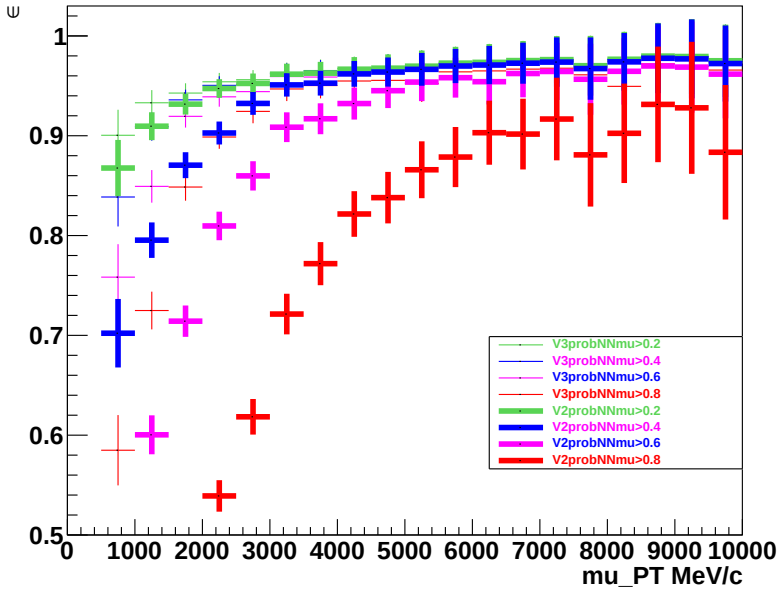

Figure 3.6: $ProbNN\mu$ variables as a function of μ_p_T.

3.7 Multivariate isolation

One of challenge of $R(\Lambda_c^*)$ measurement analysis consists into distinguish $\Lambda_b^0 \to \Lambda_c^* D_s^{(*)}$ from $\Lambda_b^0 \to \Lambda_c^* \tau^- \bar{\nu}_\tau$, since the charmed hadrons, as much as the tau, can can fly a potentially measurable distance before decaying. The decays including D_s or D_s^* contain always at least one additional reconstructible particle with respect to the tauonic decay. This feature can be used to reduce their contribution to the signal candidates. In this thesis ia new approach, developed for the $R(D^*)$ LHCb measurement [41], is used. It is a multivariate algorithm aimed to determine whether a given track originates from the same Λ_b^0 as the Λ_b^0 candidate (referred to as 'associated tracks'), or from anywhere else from the rest of the event (referred to as 'unassociated tracks'). All type of LHCb tracks are considered to maximize the number of associated tracks. Input variables to the multivariate analysis (MVA) are listed in Table 3.7, and include the properties of the track and the properties of the candidate decay with the vertex refitted to include the track that is considered. This MVA is applied to each track in the event, and the tracks with the highest (most associated-track like) MVA output are considered for

further analysis. The used algorithm is the same of R(D^*) analysis and, therefore it is trained using associated tracks taken from the $D^{**} \to D^*$ decays in simulated $B \to D^{**}\mu\nu$ events, and unassociated tracks taken from simulated $B \to D^*\mu\nu$ events with the signal decay excluded. In both cases, B candidates are reconstructed in the $D^*\mu$ final state. The output distribution for simulated $B \to D^{**}\mu\nu$ and $B \to D^*\mu\nu$ of this MVA is shown in Figure 3.7. The isolation MVA has,then, the power to distinguish between partially reconstructed signal decays and unrelated track. Moreover, it can be used as a selection tool.
Two categories of tool existed before this innovative tool:

- Cone isolation: it is based around summing properties of track within an angular cone around the considered particles;
- Vertex isolation: it is based on the proximity of the closest track to the particle which generate the decay;

The first one approach has the disadvantage that it includes a large number of tracks and it is not so sensitive to background with tracks missing, instead The second one it is ideal to select tracks originating from the PV.

Table 3.7: Input variables for the isolation MVA

Track properties:
$\chi^2_{IP} - PV$
$\chi^2_{IP} - SV$
p_T
cos($D^*\mu$, track)
Vertex properties:
$\chi^2_{flight\_distance}$
$\chi^2_{\Delta(flight\_distance)}$

3.8 Efficiency

Various effects contribute to the efficiency with which a given decay can be detected: acceptance, trigger, reconstruction and selection efficiencies. The

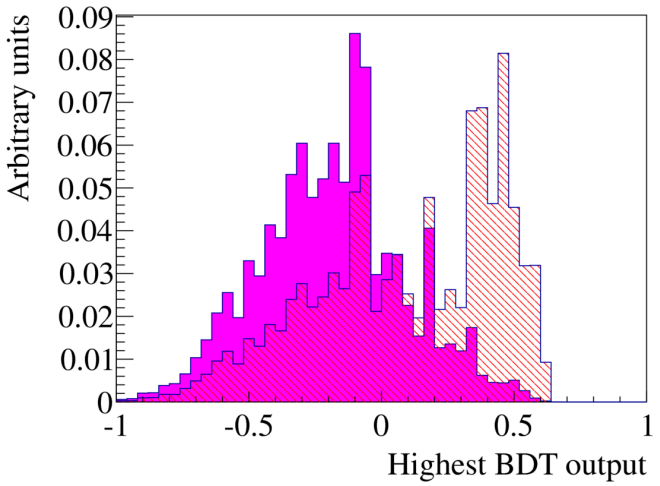

Figure 3.7: Highest isolation MVA output for any track in simulated events (magenta) $B \to D^*\mu\nu$ and in $B \to D^{**}\mu\nu$ (red) [41]

particles in the candidate events must first lie within the detector acceptance, be triggered, reconstructed and finally to pass the offline selection requirements. Each consecutive step reduces the sample further, the overall efficiency ϵ thus be written as a product:

$$\epsilon_{TOT} = \frac{N_{Trigger+Offline\_Selection}}{N_{Stripping}} \cdot \frac{N_{Stripping}}{N_{Acceptance}} \cdot \frac{N_{Acceptance}}{N_{Generated}} \tag{3.2}$$
$$= \epsilon_{Trigger+Offline\_sel|Stripping} \cdot \epsilon_{Stripping|Acceptance} \cdot \epsilon_{Acceptance|Generated}$$

where N_i is the number of events and ϵ_i is the efficiency after the i reduction of sample.

Also the effect of Particle Identification corrections have to be included. In the tables 3.8 and 3.9 are respectively listed the MC events number after each selection cut and the correspondent efficiencies. The main responsible of a decrement in the overall efficiency is the trigger selection. Since the analysis is performed applying a cut on the Δm to select only the $\Lambda_c(2625)$ decays, the overall efficiencies are evaluated after applying the cut $\Delta m \in [336.45, 346.45]$, justified in section 5.3.

	MC($\Lambda_b \to \Lambda_c^* \mu\nu$)	MC($\Lambda_b \to \Lambda_c^* \tau\nu$)	MC($\Lambda_b \to \Lambda_c^* D_s$)	MC($\Lambda_b \to \Lambda_c^* D_s^*$)
$N_{Generated}$	10M	7.5M	15M	15M
$N_{Strip\|Acc}$	359672	103195	64726	19833
$N_{Trig\|Strip}$	900073	19745	12132	3850
$N_{Trig+sel\|Strip}$	44981	9985	11299	3556
$N_{pid+\Delta m+Trig+Sel\|Generated}$	24212 ± 138	5438 ± 66	3676 ± 54	1162 ± 30

Table 3.8: Number of events in the MC samples after applying selection cuts.

	MC($\Lambda_b \to \Lambda_c^* \mu\nu$)	MC($\Lambda_b \to \Lambda_c^* \tau\nu$)	MC($\Lambda_b \to \Lambda_c^* D_s$)	MC($\Lambda_b \to \Lambda_c^* D_s^*$)
ϵ_{Acc}	0.331 ± 0.008	0.341 ± 0.008	0.326 ± 0.008	0.318 ± 0.011
$\epsilon_{overallSel\|Generated}$	$(2.4 \pm 0.01) \cdot 10^{-3}$	$(7.2 \pm 0.08) \cdot 10^{-4}$	$(2.45 \pm 0.04) \cdot 10^{-4}$	$(7.7 \pm 0.2) \cdot 10^{-5}$
ϵ	$(8.01 \pm 0.19) \cdot 10^{-4}$	$(2.47 \pm 0.06) \cdot 10^{-4}$	$(7.98 \pm 0.23) \cdot 10^{-5}$	$(2.46 \pm 0.11) \cdot 10^{-5}$

Table 3.9: Efficiencies after applying selection cuts.

Chapter 4

Reconstruction of semileptonically decaying beauty hadrons produced in high energy pp collisions

In this chapter a new method to infer the momenta of b-hadrons produced in hadron collider experiments using information from their reconstructed flight vectors is presented. In particular, the momentum is obtained using multivariate regression algorithm based on the flight information.

4.1 The b-hadron momentum in a semileptonic decay

The study of a semileptonic decay of a b-hadron, due to the presence of at least one unreconstructible neutrino in the final state poses an experimental challenge. However, in exclusive production of $B\bar{B}$ meson pairs in e^+e^- collisions at the $\Upsilon(4S)$ resonance, the decay kinematics of the B can be resolved by balancing against the $\bar{B}$ decay or vice versa. At an hadron collider, instead, the busy hadronic environment and inclusive production mechanism don't allow to reconstruct the b-hadron momentum in the laboratory rest frame using final particles and therefore to constrain the kinematics of decay. Decays with a single missing particle have an unknown 3-momentum if an assumption is made about the mass of this particle. Two independent constraints are provided by momentum conservation transverse to the flight vector. A third is provided by the assumption of the parent b-hadron mass, though this constraint is quadratic and therefore presents two solutions, as

illustrated in the section 4.2. However, no other information is available on data to select the right solution between the two possibilities. The momentum resolution is very good for the right solution, but, nearly random for the other one. Several technique have been developed, during the years, to approximate the b-hadron momentum. A possibility is to apply a statistical correction called the *k-factor*, derivable using simulated samples. This factor is the ratio between the reconstructible momentum, that is that one resulting momentum between the b-hadron and the lepton, and the true b-hadron, obviously accessible only in MC events [42]. Another possibility [43], is to consider b-hadrons that originate from decays of narrow excited b-hadron states. If the other decay products from these decays are reconstructed, then the mass of the excited state provides a further constraint on the kinematics of the child b-hadron. Further, the hadron momentum in b-hadron the rest frame can be calculated using the b-hadron momentum direction, determined from the unit vector to b-hadron decay vertex from the associated primary vertex and assuming that the proper velocity $\beta\gamma$ of visible part of semileptonic decay. This method is used to perform the $\mathrm{R}(\Lambda_c^*)$ measurements illustrated in this thesis, and will be explained in next chapter in section 5.1. Finally, in this thesis a new method is presented, based on the identification of the variables that are correlated with the b-hadron momentum, but that are independent of the manner in which the b-hadron decays. This implies that the method can be accurately validated with fully reconstructible decays that have a similar topology to the signal. A regression based estimate of the b-hadron momentum, using these variables as input, can then be used to lift the quadratic ambiguity. The studies presented, published on Journal of High Energy Physics [44], use the example of the LHCb experiment, but the ideas should be applicable to any other current or future hadron collider experiment and several centre-of-mass energies are therefore considered. This new algorithm is developed and tested on $B_s^0 \to K^-\mu^+\nu_\mu$ decays, and in the last section of this chapter is shown hits application to the transferred momentum reconstruction in $\Lambda_b^0 \to \Lambda_c^{*+}\mu^-\bar{\nu}_\mu$.

4.2 The b-hadron momentum reconstruction

In semileptonic decays $H_b^0 \to H_c^{*+}\mu^-\bar{\nu}_\mu$ the energy-momentum conservation gives:

$$\begin{cases} \sqrt{m_{H_b}^2 + p_{H_b}^2} = \sqrt{m_{H_c^*\mu^-}^2 + p_{H_c^*\mu^-}^2} + |p_{\bar{\nu}}| \\ \mathbf{p}_{H_b} = \mathbf{p}_{H_c^*\mu^+} + \mathbf{p}_{\bar{\nu}} \end{cases} \tag{4.1}$$

These are four equations with six unknown variables: $p_{H_b}^i$ and $p_{\bar{\nu}}^i$, with i=x,y,z. Given the good resolution on vertex reconstruction of the LHCb detector, we can reconstruct the flight direction determined by the primary and secondary vertex positions. In this way, we have an useful constraint to solve the system but a two-fold ambiguity remains, given the quadratic constraint. To get solutions, it is useful to work in the plane defined by $H_c^{*-}\mu^+$ the and H_b momentum vectors, and use the H_b^0 flight direction to define a parallel and an orthogonal axis. Thus, the previous system 4.1 can be written as:

$$\begin{cases} |\boldsymbol{p}_{\boldsymbol{H_b}}| = p_{H_c^*\mu}^{||} + p_{\bar{\nu}}^{||} \\ p_{H_c^*\mu}^{\perp} = -p_{\bar{\nu}}^{\perp} \end{cases} \tag{4.2}$$

with

$$|\boldsymbol{p}_{\bar{\boldsymbol{\nu}}}|^{\,2} = p_{\bar{\nu}}^{\perp 2} + p_{\bar{\nu}}^{||2};$$

and

$$\left|\boldsymbol{p}_{\boldsymbol{H_c^*\mu}}\right|^{\,2} = p_{H_c^*\mu}^{\perp 2} + p_{H_c^*\mu}^{||2}$$

By substituting the above equations into system 4.1, the H_b^0 momentum can be determined with a two-fold ambiguity:

$$p_{\bar{\nu}}^{||} = \frac{-b \pm \sqrt{b^2 - 4ac}}{2a} \tag{4.3}$$

where

$$\begin{aligned} a &= 4(p_{\bar{\nu}}^{\perp 2} + m^2_{H_c^*\mu}) \\ b &= 4p^{||}_{H_c^*\mu}(2p_{\bar{\nu}}^{\perp 2} - m^2_{miss}) \\ c &= 4p_{\bar{\nu}}^{\perp 2}(p^{||2}_{H_c^*\mu} + m^2_{H_b}) - |m^2_{miss}|^2 \\ m^2_{miss} &= m^2_{H_b} - m^2_{H_c^*\mu} \end{aligned} \tag{4.4}$$

The two solution obtained from Eq.4.3, inserted in Eq.4.2, give the two possibile values for the H_b momentum in the laboratory frame: p_H^+ and p_H^-.

4.3 Simulation of inclusive beauty production

The Pythia [37] event generator is used to simulate inclusive b-hadron pair production in pp collisions at three centre-of-mass energies, $\sqrt{s}$ = 7, 13, 100 TeV. Unless explicitly stated otherwise, the studies that follow are based on the 13 TeV sample. A right-handed coordinate system is defined with z along the beam axis into the detector, y vertical and x horizontal. The magnitude of the momentum of a particle is denoted P, and the component transverse to the z axis is defined as $p_T = P\sin\theta$. The component of the momentum along the z axis is denoted p_z. A particle has a pseudorapidity defined as $\eta = -\log(\tan(\theta/2))$. A particle of energy E is defined to have a rapidity of $y = \frac{1}{2}\log((E+p_z)/(E-p_z))$. Signal b-hadron candidates are required to be produced within the range $2 < \eta < 5$, which corresponds to the approximate kinematic acceptance of the LHCb detector. Figure 4.1 shows, for each of the three centre-of-mass energies under consideration, the P, p_T and η distributions of the b-hadrons in the event sample. One of the first things to notice is that the p_T distribution has a smaller tail than the momentum distribution. This is a feature that is exploited in this work. With increasing centre-of-mass energy, the b-hadron production tends to be at larger pseudorapidities and larger momenta, but the p_T spectrum is less strongly affected.

Since the main features that we try to utilize in this study are related to the line of flight between the b-hadron production and decay vertices, which

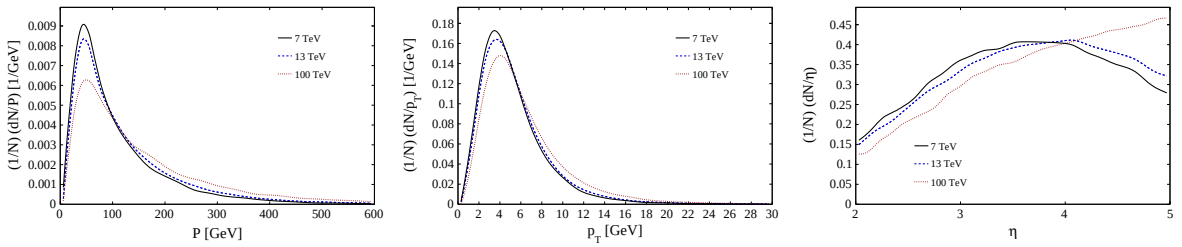

Figure 4.1: Basic b-hadron kinematic distributions in our simulated event samples: (top left) momentum, (top right) transverse momentum, (lower) pseudorapidity.

is denoted $\vec{F}$, it is crucial to model the resolution in the associated variables. The x and y co-ordinates of the b-hadron decay vertices are smeared by $\pm 20 \mu m$ according to a Gaussian distribution. In the z direction a larger resolution of $\pm 200 \mu m$ is assumed. For the production vertices we assume resolutions of $\pm 13 \mu m$ in x and y, and $\pm 70 \mu m$ in z. These assumptions approximately reflect the reported peformance of the LHCb VELO detector [26]. In all subsequent studies it is required that the smeared flight length is larger than 3 mm, which approximates the effect of typical trigger and analysis selections of b-hadron decays by LHCb.
Exclusive decays of B_s mesons to $K^- \mu^+ \nu_\mu$ are simulated with a simple phase space description, which is considered to be sufficiently accurate for the present study. To the B_s decay products it is required that the charged final state particles satisfy $P > 5$ GeV and $1.9 < \eta < 4.9$. Moreover, $p_T(\mu) > 1$ GeV and $p_T(K) > 0.5$ GeV is requred. As a background the decay $B_s^0 \to (K^{*-} \to K^- \pi^0) \mu^+ \nu_\mu$, in which the π^0 isn't reconstructed, has been simulated.

4.4 Variables that are correlated to the b momentum

We attempt to identify variables that are correlated to the b-hadron momentum, but strictly restrict to those that are independent of the b-hadron decay properties. The single most important feature that we try to exploit is apparent in figure 4.2 (left) which shows the distribution of p_T versus η. The (anti-)correlation between the two variables is weak, with a coefficient

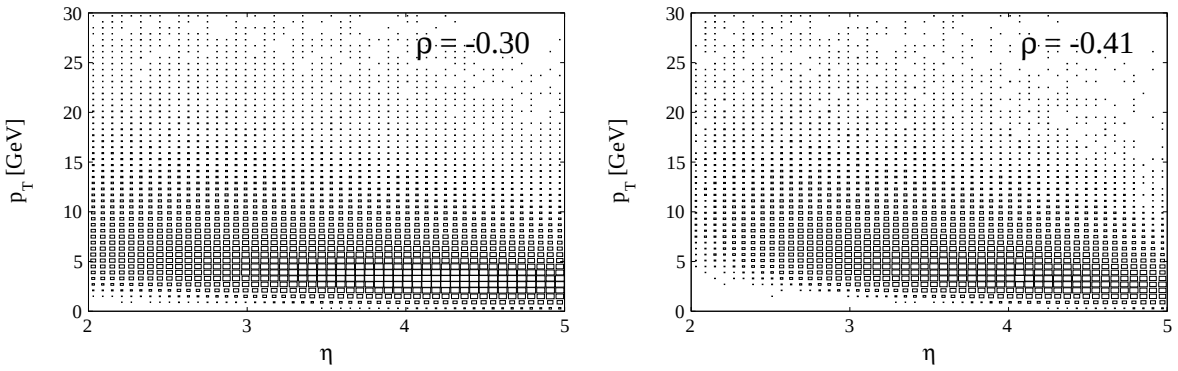

Figure 4.2: Distribution of p_T versus η in the simulated sample of b-hadrons (left) without any simulated decay and (right) with simulated $B_s \to K\mu\nu$ decays that are required to satisfy the basic selection requirements as described in the text.

of around 30%, as indicated on the figure. It is therefore possible to estimate the momentum of the b-hadron as,

$$P = \frac{\overline{p_T}}{\sin\theta_{\text{flight}}}, \tag{4.5}$$

where θ_{flight} is the polar angle of the flight vector, and it can be seen in figure 4.1 that $\overline{p_T} \approx 5$ GeV in our simulated samples. This approximation should return a momentum estimate with a resolution function that resembles the p_T distribution in figure 4.1. In figure 4.3 (left) the distribution of $1/\sin\theta_{\text{flight}}$ is shown. figure 4.3 (right) shows that this variable has a near linear relation to the b-hadron momentum with a correlation coefficient of around 65%. The approximation above is degraded once it is appreciated that the charged decay products from the b-hadron must be within the acceptance of the detector. figure 4.2 (right) shows the distribution of p_T versus η for simulated $B_s \to K\mu\nu$ m decays that satisfy the selection cuts. This has the effect of suppressing the region of low p_T and low η, thus increasing the magnitude of the correlation between these two variables by around 10%.

The flight length, $|\vec{F}|$, of a b-hadron of mass M and decay time t can be directly related to the momentum according to,

$$P = \frac{M|\vec{F}|}{t}. \tag{4.6}$$

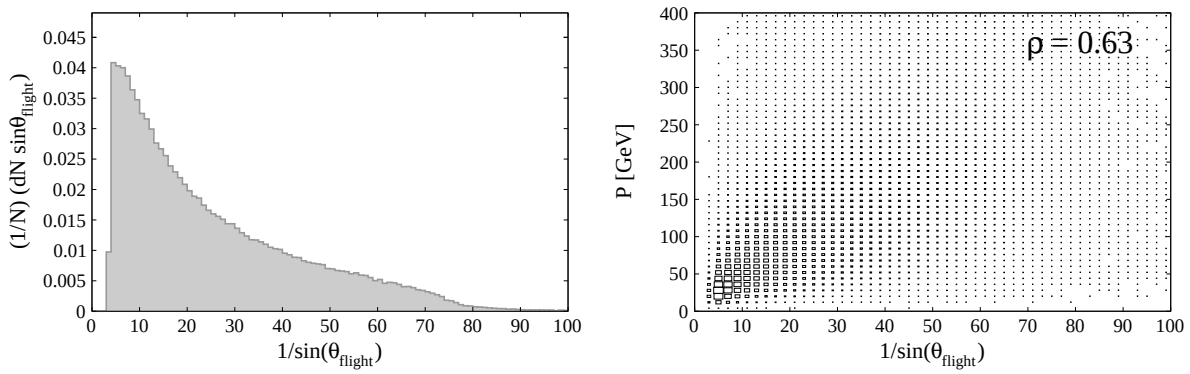

Figure 4.3: The left-hand figure shows the $1/\sin\theta_{\text{flight}}$ distribution of the simulated b-hadrons that are within the LHCb acceptance. The right-hand figure shows the distribution of the same variable versus the b-hadron momentum.

figure 4.4 (left) shows the distribution of $|\vec{F}|$, in which our requirement of at least 3 mm is clearly visible. figure 4.4 (right) shows that this variable is correlated with the momentum with a coefficient of around 50%. We have

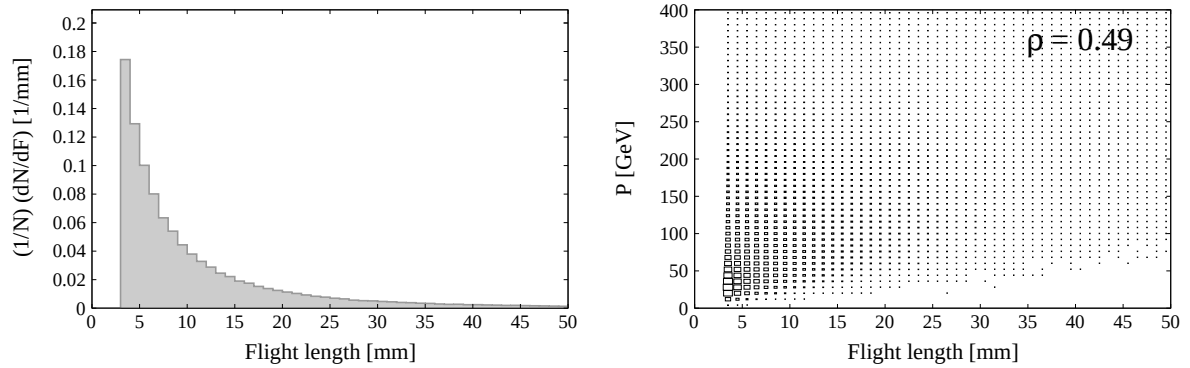

Figure 4.4: The left-hand figure (left) shows the $|\vec{F}|$ distribution of the simulated b-hadrons that are within the LHCb acceptance. The right-hand figure (right) shows the distribution of the same variable versus the b-hadron momentum.

considered the use of information from other reconstructed particles in the event. It is obvious that in the hypothetical case of a detector with 4π angular coverage and perfect efficiency and resolution, the b-hadron p_T could be inferred from the transverse momentum balance. Considering the LHCb detector, and the most optimistic use of all kinematic information from the reconstructible particles, we can only achieve a correlation of around 20%

between the missing p_T and the p_T of the signal b. As an alternative, we have considered the possibility to reconstruct the $\bar{b}$-hadron that is produced in association with the signal b. Even at $b(\bar{b})$-quark level the naive p_T balance between the b and $\bar{b}$ is sploilt by the broad $b\bar{b}$ p_T spectrum. Various combinations of reconstructing the signal b and associated $\bar{b}$ at hadron or jet level have been considered. [1] Even before considering the inefficiency of reconstructing the associated $\bar{b}$ this approach does not seem promising. Therefore, there are only two pieces of information related to the b-hadron flight vector, namely $1/\sin\theta_{\text{flight}}$ and $|\vec{F}|$, which are of value in an estimator of the b-hadron momentum.

4.5 Multivariate regression analysis

The two flight variables described in the previous section, $1/\sin\theta_{\text{flight}}$ and $|\vec{F}|$, are considered in a multivariate regression analysis in order to infer the momenta of the b-hadrons. A simple least squares linear regression algorithm, as implemented in the sklearn package [45], is used. This algorithm is trained on a randomly selected subset of the simulated event sample. The independent data are used to evaluate the performance of the algorithm in estimating the b-hadron momentum from the values of the two flight variables. figure 4.5 shows the distribution of the inferred b-hadron momentum, P_{inf}, versus the true b-hadron momentum. The correlation coefficient is around 70%. In table 4.1, the correlation coefficients between P_{true} and the two flight variables are listed for the three centre of mass energies and various selection requirements on the simulated $B_s \to K\mu\nu$ decays. Also listed are the correlations between P_{true} and the inferred momentum that would be returned by the regression using only $1/\sin\theta_{\text{flight}}$, which is denoted p^{θ}_{inf}. It can be seen that as expected these values are close to the corresponding correlations with the raw flight angle variable itself. The final column of table 4.1 lists the correlations between P_{true} and P_{inf}. It can be seen that the combination of the two variables in the regression algorithm increases the correlation by

[1] In the case of the signal b-hadron at jet level, we consider particles within a hollow cone around the b, in order to avoid picking up the b-hadron decay products.

around 10% compared to the more powerful angular variable alone. Hardly any dependence on the centre-of-mass energy is seen. There is a degradation of the correlations of up to 10% when applying the acceptance and selection requirements on the charged decay products of the simulated $B_s \to K\mu\nu$ decays. The inclusion of $|\vec{F}|$ in the two-variable version increases the correlation between P_{inf} and P_{true} by a few percent. figure 4.6 (left) shows the distribution of $(P_{\text{inf}} - P_{\text{true}})/P_{\text{true}}$ and the corresponding distribution for P_{inf}^{theta} instead of P_{inf}. As expected the shapes of these distributions roughly resemble the underlying b-hadron p_T spectrum shown in figure 4.1. In figure 4.6 (right) the corresponding profiles of the mean $|P_{\text{inf}} - P_{\text{true}}|/P_{\text{true}}$ are shown as a function of η. The resolution of P_{inf} is around 60% and exhibits some dependence on η. It is about 10–20% improved compared to that of P_{inf}^{θ} which neglects the decay length information. We further check the robustness of the method with respect to our assumptions on the vertex resolution. Even for variations of up to three orders of magnitude there is a negligible effect on the performance.

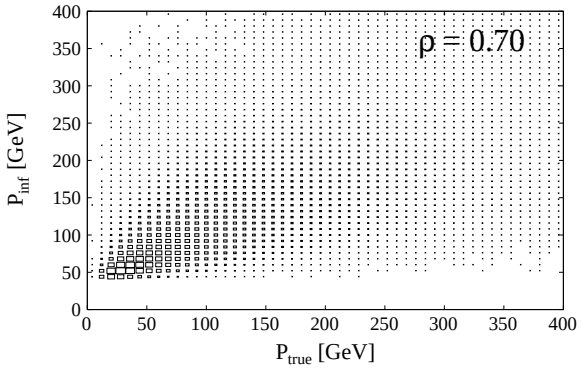

Figure 4.5: The distribution of P_{inf} versus the true b-hadron momentum.

4.6 Application to q^2 reconstruction in $\Lambda_b \to \Lambda_c^* \mu \bar{\nu}_\mu$

In this section the regression algorithm is applied to the reconstruction of the $\Lambda_b \to \Lambda_c(2625)\mu\bar{\nu}_\mu$. The inferred Λ_b momentum, P_{inf}, has been obtained with the MC, using the least square regression algorithm as described before for the $B_s \to K\mu\bar{\nu}_\mu$. The parameters of the regression function have been

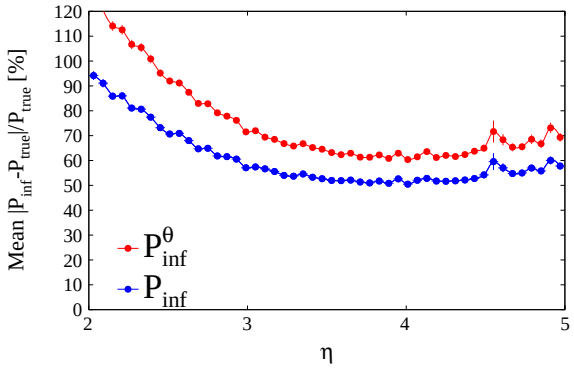

Figure 4.6: The left-hand figure shows the distribution of $(P_{\text{inf}} - P_{\text{true}})/P_{\text{true}}$. The right-hand figure shows how the profile of $|P_{\text{inf}} - P_{\text{true}}|/P_{\text{true}}$ varies with η. Both figures include the corresponding entries for P_{inf}^{theta}.

extracted minimizing the objective function $F = \sum_{events}(p_{inf} - p_{True})^2$, where the functional dependence of p_{inf} on the flight distance and flight angle is given by

$$P_{inf} = a \cdot \frac{1}{\sin\theta_{flight}} + b \cdot |\vec{F}| \tag{4.7}$$

p_{true} is the per-event true momentum of the Λ_b and the coefficienct a and b are free parameteres in the minimization. The distribution of P_{inf} as a function of P_{true} is shown in figure 4.7. The momentum resolution of P_{inf} is about 55% and its correlation with the true momentum is about $\rho = 0.60$. The reduced correlation observed compared to the $B_s \to K\mu\bar{\nu}_\mu$, shown on figure 4.5, is due to the selection as described before. In the $\Lambda_b \to \Lambda_c(2625)\mu\bar{\nu}_\mu$ the P_{inf} resolution is enough to significantly improve the chance to select the best solution between $P^+_{\lambda_b}$ and $P^-_{\lambda_b}$, compared with a simple random choice. We chose as best Λ_b momentum, the solution $P^{\pm}_{\lambda_b}$, closet to P_{inf}.

From the best P_{Λ_b}, the estimated q^2_{reg} can be easily computed. Compared with a random choice of the two $P^{\pm}_{\lambda_b}$ solutions, the resolution improvement is about 15% as shown in figure 4.8.

The q^2 resolution depends on the q^2 itself. In figure4.9 the q^2 resolution in various q^2 bins is reported. The improvements in the q^2 resolution obtained using q^2_{reg} vary between 10% to more than 20%.

		Correlation coefficient			
$\sqrt{s}$	Cuts	$1/\sin\theta$	$\lvert F\rvert$	P^{θ}_{inf}	P_{inf}
7 TeV	None	0.63	0.50	0.61	0.69
7 TeV	P, p_T	0.67	0.59	0.67	0.68
7 TeV	P, p_T, η	0.49	0.52	0.49	0.56
13 TeV	None	0.63	0.49	0.63	0.70
13 TeV	P, p_T	0.60	0.50	0.60	0.69
13 TeV	P, p_T, η	0.53	0.48	0.53	0.65
100 TeV	None	0.62	0.48	0.63	0.69
100 TeV	P, p_T	0.59	0.50	0.60	0.69
100 TeV	P, p_T, η	0.53	0.48	0.54	0.65

Table 4.1: The coefficients of correlation between the true b-hadron momentum, and the raw flight variables and the inferred momentum from the regression. For each centre-of-mass energy, as indicated in the first column, the first row corresponds to only the basic flight length and acceptance requirements on the b-hadron. The second and third rows sequentially apply P, p_T and η requirements on the charged decay products in the simulated $B_s \to K\mu\nu$ decays.

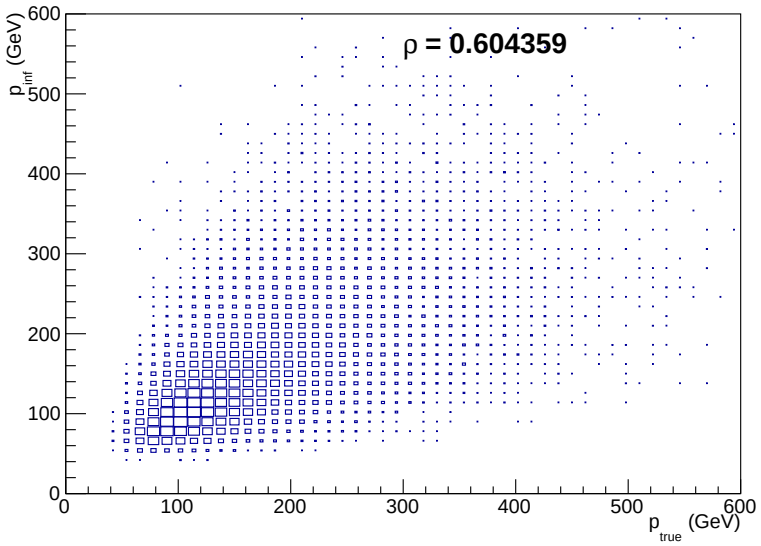

Figure 4.7: Distribution of P_{inf} as a function of the Λ_b momentum. The correlation is $\rho = 0.60$.

4.7 Conclusion

The algorithm described here allows to improve the resolution in the determination of the decay kinematic variables for any semileptonic decays like $H_b \to H_c\mu\bar{\nu}_\mu$ or $H_b \to H_u\mu\bar{\nu}_\mu$. The improved resolutions can be exploited to measure the differential decay width $d\Gamma(H_b \to H\mu\bar{\nu}_\mu)/dq^2$ with good pre-

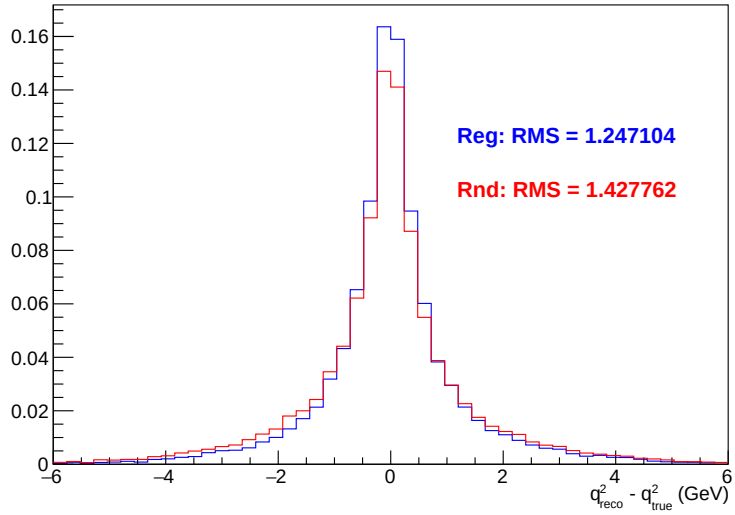

Figure 4.8: Resolution of q^2 obtained using the regression algorithm (blue), compared with the one obtained using a random choice between the $p^+_{\Lambda_b}$ and $p^-_{\Lambda_b}$ (red).

cision because of the reduced migrations between the q^2 bins. Unfortunately the algorithm cannot be applied successfully to improve the kinematic of semitauonic decays $H_b \to H\tau\bar{\nu}_\tau$. In the section 5.8 the diffential decay rate $d\Gamma(\Lambda_b \to \Lambda_c(2625)\mu\bar{\nu}_\mu)/dq^2$ is extracted using a q^2 reconstruction, defined in the section 5.1, that, despite the worst resolution, is suitable for both $\Lambda_b \to \Lambda_c^+(2625)\mu\bar{\nu}_\mu$ and $\Lambda_b \to \Lambda_c^+(2625)\tau\bar{\nu}_\tau$.

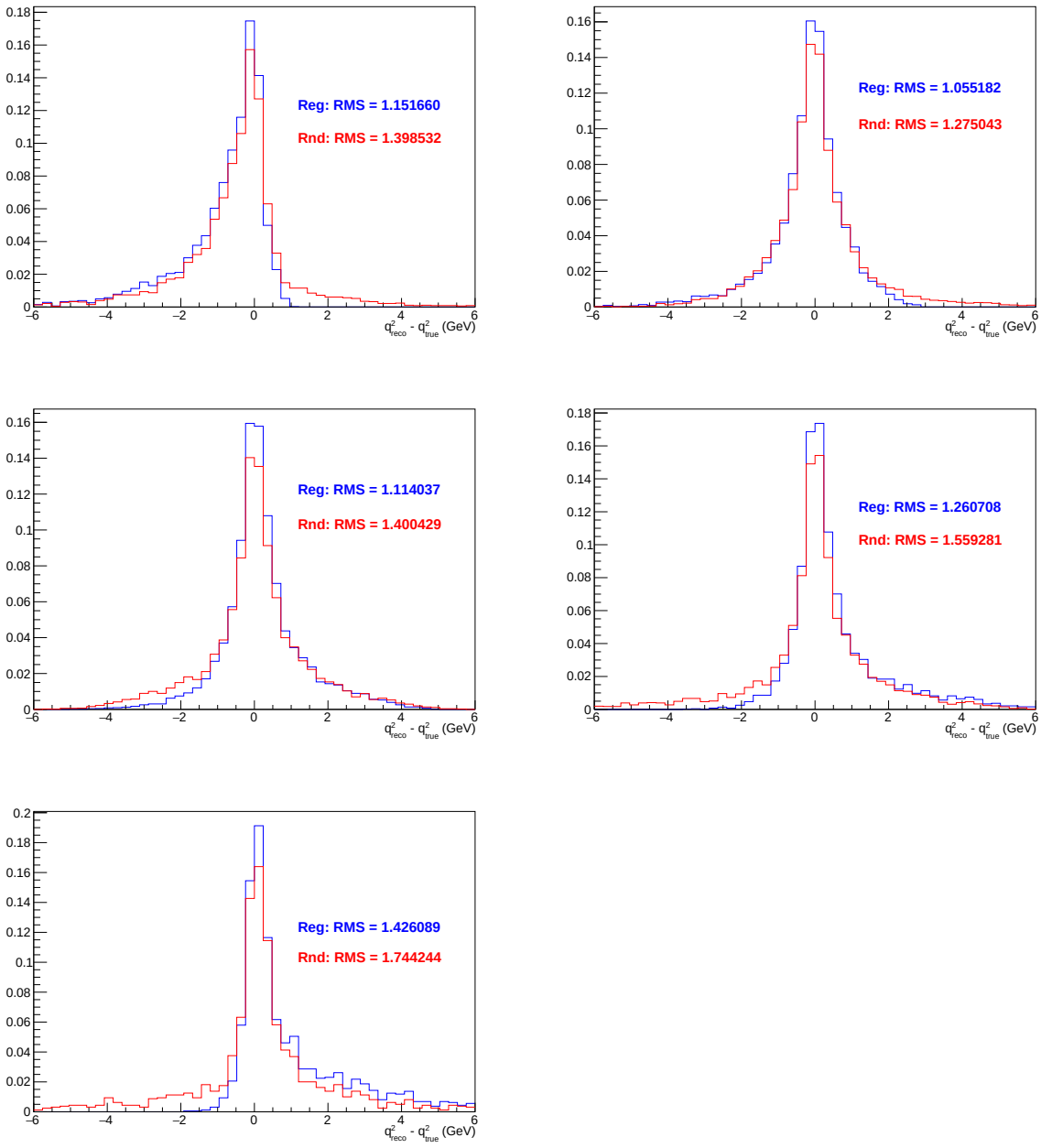

Figure 4.9: Resolution $q^2_{reg} - q^2_{true}$ in five bins of q^2_{true}. From left to right, top to bottom: $0 < q^2_{true} < 1\ GeV^2$, $1 < q^2_{true} < 3\ GeV^2$, $3 < q^2_{true} < 5\ GeV^2$,$5 < q^2_{true} < 7\ GeV^2$, $7 < q^2_{true} < 9\ GeV^2$.

Chapter 5

Signal selection

In this chapter, the strategy to isolate the signal from the $\Lambda_b \to \Lambda_c^* \mu\nu$ decays is presented. To separate out semitauonic Λ_b^0 decays followed by $\tau \to l\nu\nu$ from normalization channel $\Lambda_b \to \Lambda_c^* \mu\nu$, it is necessary to exploit differences in the kinematics of the two processes that result from the large $\mu - \tau$ mass difference as well as the softer lepton energy, the presence of extra neutrinos from the $\tau \to \tau\nu\nu$ decay and of a further displaced decay vertex. The kinematic distributions of $\Lambda_b \to \Lambda_c^* D_s^{(*)}$ are very similar to those of the semitauonic decays, but it is possible to discriminate them from the others using the handle giving by the multivariate isolation variables 3.7 and the momentum transferred, (described in the next sections).
Moreover the techniques to estimate the combinatorial background and the muon misidentification contribution are shown.

5.1 Λ_b^0 Frame Reconstruction of Kinematic Variables

As seen in Chapter 3, at an hadron collider, due to the presence of one or more neutrinos, is not possible to reconstruct the Λ_b^0 momentum in the laboratory rest frame using final particles and therefore to constrain the kinematics of decay. Hence, it is necessary to use an approximation. In this thesis, the hadron momentum in the Λ_b^0 rest frame is calculated using the Λ_b^0 momentum direction, determined from the unit vector to Λ_b^0 decay vertex from the associated primary vertex and assuming that the proper velocity $\beta\gamma$ of visible part of semileptonic decay along z-axis is equal to Λ_b^0 proper

velocity along the same axis:

$$(p_{\Lambda_b^0})_z = (p_{\Lambda_c^*\mu})_z \frac{m_{\Lambda_b^0}}{m_{\Lambda_c^*\mu}}$$

$$|p_{\Lambda_b^0}| = (p_{\Lambda_c^*\mu})_z \frac{m_{\Lambda_b^0}}{m_{\Lambda_c^*\mu}} \sqrt{(1+\tan^2\alpha)}$$

where is α is the angle between unit vector and z axis (beam pipe) [41]. This approximation is called "boost approximation". The Λ_b^0 momentum is calculated according this approximation in all studied presented in the following sections. The figure 5.1 shows the resolution on Λ_b^0 momentum and the consequent resolutions on missing mass square ($MM^2 = (p^\mu_{\Lambda_b^0} - p^\mu_{(\Lambda_c^*\mu)})^2$) and transferred momentum ($q^2 = (p^\mu_{\Lambda_b^0} - p^\mu_{(\Lambda_c^*)})^2$), quantities described in the section 5.2.

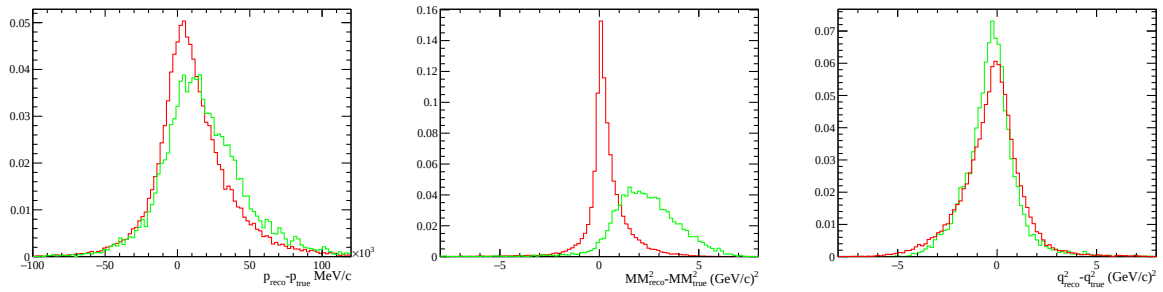

Figure 5.1: Momentum resolution (left), missing mass resolution (center), transferred momentum (right) for the simulated decays $\Lambda_b^0 \to \Lambda_c^*\tau^-\bar{\nu}_\tau$ (Green) and $\Lambda_b^0 \to \Lambda_c^*\mu^-\bar{\nu}_\mu$(Red). The label i_{RECO} described the quantities calculated using the boost approximation, i_{TRUE} those one which use the simulated variables.

5.2 Discriminating Variables

The kinematics of the visible particles in $\Lambda_b^0 \to \Lambda_c^{*+}\mu^- X$ decay modes depend on the mass and momentum of the missing particles. This allows $\Lambda_b^0 \to \Lambda_c^{*+}\tau^-\bar{\nu}_\tau$ to be distinguished from $\Lambda_b^0 \to \Lambda_c^{*+}\mu^-\bar{\nu}_\mu$, and from other sources

of background. The presence of not reconstructible particles in the decays suggests to evaluate the missing mass. It is defined as:

$$\begin{aligned} MM^2 &= (p^{\mu}_{\Lambda_b^0} - p^{\mu}_{(\Lambda_c^*\mu)})^2 = \\ &= m^2_{\Lambda_b^0} + m^2_{(\Lambda_c^*\mu)} - 2(E_{\Lambda_b^0}E_{(\Lambda_c^*\mu)} - p_{\Lambda_b^0}p_{(\Lambda_c^*\mu)}cos(\theta_{(\Lambda_c^*\mu)})) \end{aligned} \tag{5.1}$$

where p_i^{μ} is the four momentum of particle i and therefore the formula can be decomposed in energy E_i and momentum p_i components.

In case of direct semileptonic decays with only a missing track due to a neutrino, such as $\Lambda_b^0 \to \Lambda_c^{*+}\mu^-\bar{\nu}_\mu$, this variable is expected to peak to zero. Instead, for $\Lambda_b^0 \to \Lambda_c^{*+}\tau^-\bar{\nu}_\tau$ and double charmed decays, more than one tracks are missed and the distributions of MM^2 will peak on average to values higher than zero. This can be seen in figure 5.2, where the MM^2 distributions for MC($\Lambda_b^0 \to \Lambda_c^{*+}\mu^-\bar{\nu}_\mu$), MC($\Lambda_b^0 \to \Lambda_c^{*+}\tau^-\bar{\nu}_\tau$) and double charm decays are plotted: in the left side of the figure the distributions of muonic and tauonic decays are shown. The distributions are affected by the reconstruction effects, in fact, otherwise the muonic MM^2 would be always equal to zero. This can be inferred by missing mass resolution distribution, shown on figure 5.2. Only the events for which the reconstructed particles match the generated ones have been selected. It can be observed that the main discriminant power of this variable is in the separation of muonic and tauonic decay.

Morover, the muons from the $b \to c\tau\nu \to c(\mu\nu\nu)\nu$ decay chain are typically much softer than the primary muons which come directly from the $b \to c\mu\nu$ decay, so that for $\Lambda_b^0 \to \Lambda_c^*\tau^-\bar{\nu}_\tau$ events the rest frame energy E^* peaks at small values, as shown in figure 5.3.

There are other two variables which allow us to slightly separate semitauonic from semimuonic decay: the impact parameter in unit of χ^2 of the muons with respect to primary vertex ($\chi^2_{IP}(\mu)$ (see 3.1.1)) and the variable describing the Λ_b^0 decaying vertex quality ($\chi^2_{vtx}(\Lambda_b^0)$)(see 3.1.1)). The first one should give different results for signal and normalization channel since the impact parameter of the muon derived by the semitauonic decays is expected to be greater than those form direct decays. Instead, the Λ_b^0 vertex,

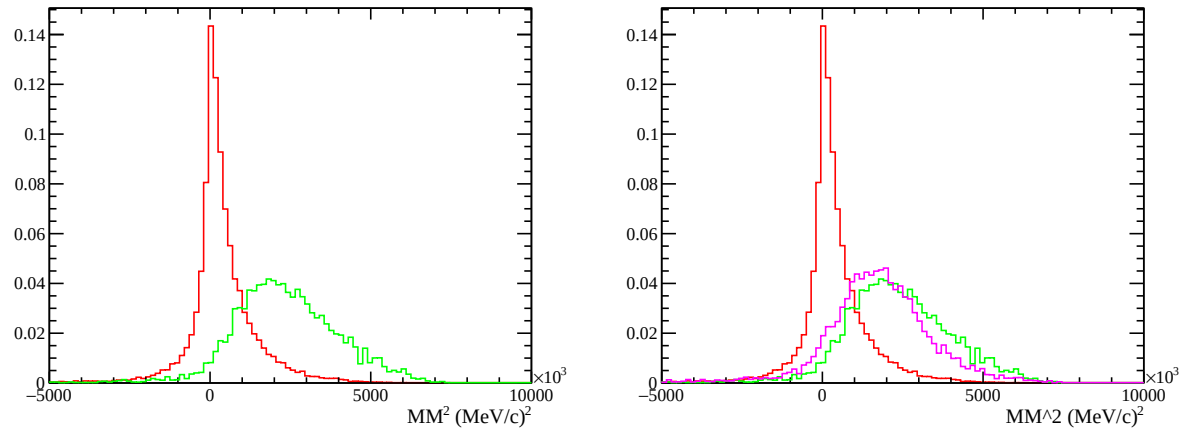

Figure 5.2: Missing mass square for the simulated decays: $\Lambda_b^0 \to \Lambda_c^* \tau^- \bar{\nu}_\tau$ (Green), $\Lambda_b^0 \to \Lambda_c^* \mu^- \bar{\nu}_\mu$(Red) and (only right) $\Lambda_b \to \Lambda_c^* D_s^*$ added to $\Lambda_b \to \Lambda_c^* D_s$ (Pink).

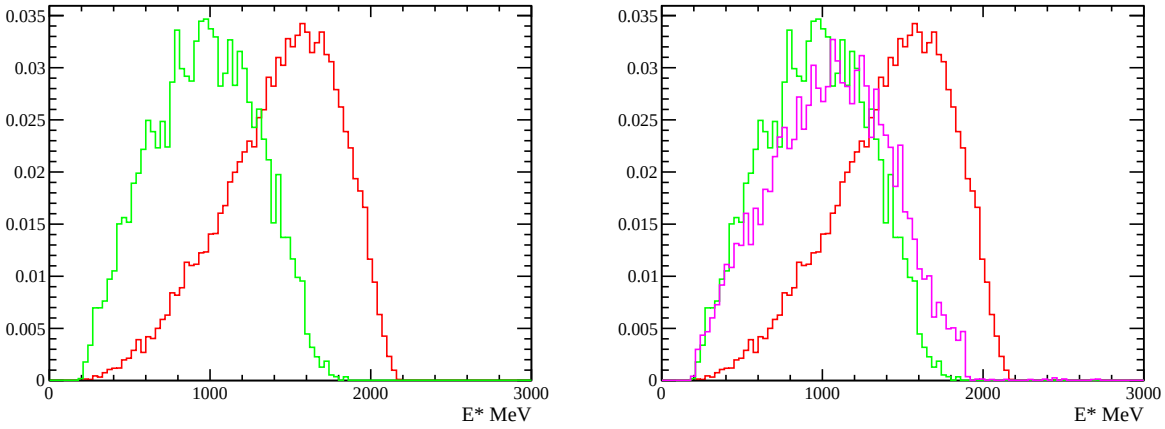

Figure 5.3: Energy of the muon on the center of mass of Λ_b^0: $\Lambda_b^0 \to \Lambda_c^* \tau^- \bar{\nu}_\tau$ (Green), $\Lambda_b^0 \to \Lambda_c^* \mu^- \bar{\nu}_\mu$(Red) and (only right) $\Lambda_b \to \Lambda_c^* D_s^*$ added to $\Lambda_b \to \Lambda_c^* D_s$ (Pink).

in the tauonic decay is formed without the muonic constraint and therefore the vertex quality should be less accurate. The correspondent distributions are in figure 5.4. They provide a slight separation but they have been put in input of a multivariate analysis, presented in section 5.5.1.

Finally, another relevant variable is the transferred momentum. It is defined such as:

$$\begin{aligned} q^2 &= (p^\mu_{\Lambda_b^0} - p^\mu_{\Lambda_c^*})^2 = \\ &= m^2_{\Lambda_b^0} + m^2_{\Lambda_c^*} + 2(E_{\Lambda_b^0} E_{\Lambda_c^*} - p_{\Lambda_b^0} p_{\Lambda_c^*} cos\theta_{\Lambda_c^*}) \end{aligned} \tag{5.2}$$

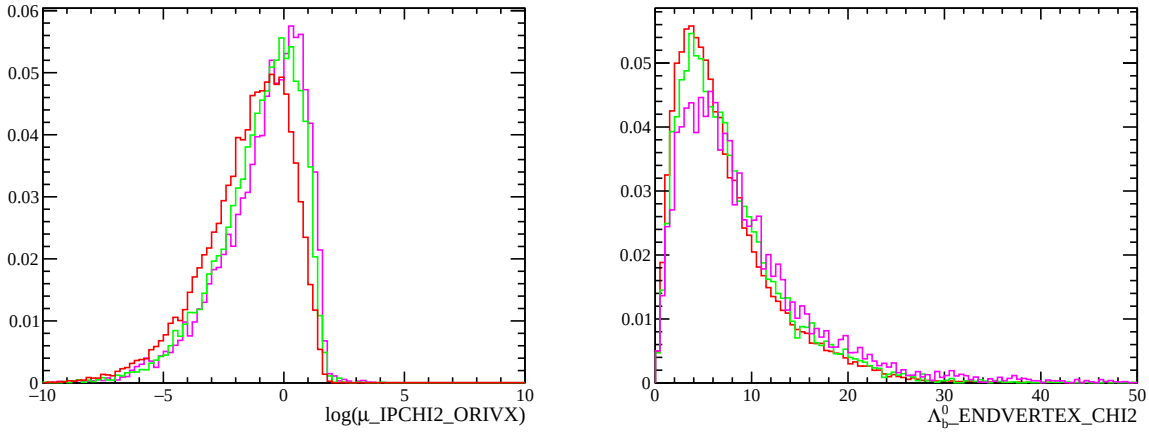

Figure 5.4: The impact parameter in unit of chi^2 of the muons with respect to primary vertex (left) and the Λ_b^0 decaying vertex quality (right) : $\Lambda_b^0 \to \Lambda_c^* \tau^- \bar{\nu}_\tau$ (Green), $\Lambda_b^0 \to \Lambda_c^* \mu^- \bar{\nu}_\mu$(Red) and (only right) $\Lambda_b \to \Lambda_c^* D_s^*$ added to $\Lambda_b \to \Lambda_c^* D_s$ (Pink).

where p_i^μ is the four momentum of particle i and therefore the formula can be decomposed in energy E_i and momentum p_i components.
The semitauonic decays, in fact, can be occur in the kinematic region restricted to $q^2 = (p^\mu_{\Lambda_b^0} - p^\mu_{\Lambda_c^*})^2 > m_\tau^2$ while the $\Lambda_b^0 \to \Lambda_c^{*+} \mu^- \bar{\nu}_\mu$ extends all the way down to $q^2 > m_\mu^2 \approx 0$. It can be seen in figure 5.5. In this image also the distribution of $\Lambda_b \to \Lambda_c^* D_s$ transferred momentum appears, and it can be noticed that the shape is different with respect to muonic and tauonic decays, therefore discriminable from the others.

In particular, in this thesis, to take the biggest advantages of transferred momentum variable, this one has been evaluated in five different intervals, chosen basing on the kinematic properties of signal, normalization, double charmed channels and combinatorial background. In fact, in the first two bins, $q^2 \in [-10, 1](\mathrm{GeV}/c)^2$ and $q^2 \in [1, 3](\mathrm{GeV}/c)^2$ only seminuonic and combinatorial decays are expected; in third and fourth defined by $q^2 \in [3, 5](\mathrm{GeV}/c)^2$ and $q^2 \in [5, 7](\mathrm{GeV}/c)^2$ all components should be present, and finally the interval $q^2 \in [7, 10](\mathrm{GeV}/c)$ should be depleted in semimuonic decays.

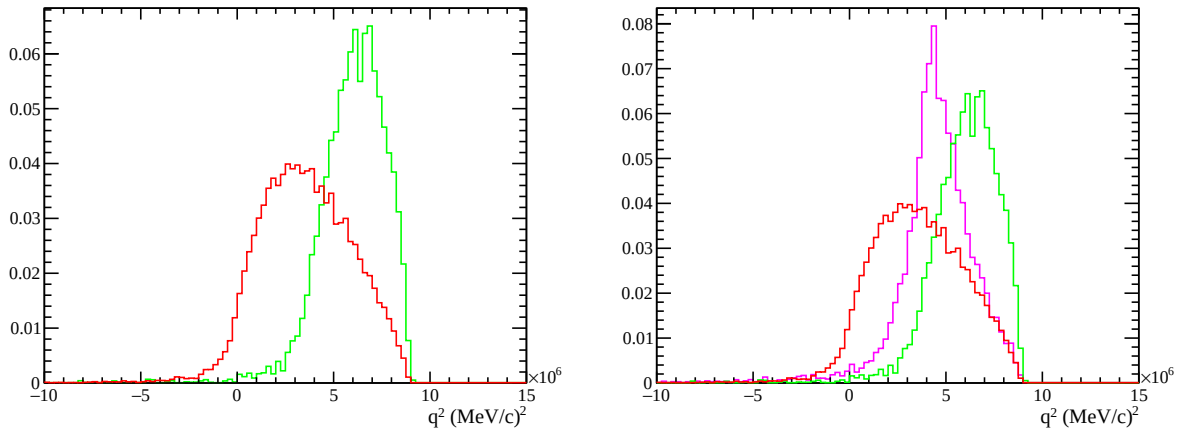

Figure 5.5: Momentum transferred for the simulated decays: $\Lambda_b^0 \to \Lambda_c^* \tau^- \bar{\nu}_\tau$ (Green), $\Lambda_b^0 \to \Lambda_c^* \mu^- \bar{\nu}_\mu$(Red) and (only right) $\Lambda_b \to \Lambda_c^* D_s^*$ added to $\Lambda_b \to \Lambda_c^* D_s$ (Pink).

5.3 Samples enriched using isolation

In this thesis it is used the output of the MVA isolation presented in section 3.7, to identity one sample depleted of Λ_b^0 double charmed decays with respect to those one semitauonic. In particular, the considered variable is the $\Lambda_b^0\_ISOLATION\_BDT$ (in the following cited as ISO) which is that one containing the highest MVA BDT outputs. In fact in every track in an events, that is not a candidate element of the searched decay, is evaluated and those one for which the BDT value is highest are inserted in the considered isolation variable. In other to define a boundary value of the sample depleted of Λ_b^0 double charmed decays, we looked for the value of the ISO variable for which is maximized the ratio given by

$$f = \frac{n_{MC}(\Lambda_b^0 \to \Lambda_c^* \tau^- \bar{\nu}_\tau)}{\sqrt{n_{MC}(\Lambda_b^0 \to \Lambda_c^* D_s^*) + n_{MC}(\Lambda_b^0 \to \Lambda_c^* D_s)}}$$

Table 5.1 report the ratios correspondent to several cut: the value which maximize the ratio is $ISO < 0.25$. In the following section and chapter, all quantities are evaluated in the due identified isolation bins: $ISO \leq 0.25$ and $ISO < 0.25$.

ISO value	f	ISO value	f
< -0.3	54.29	< 0.10	70.68
< -0.25	58.46	< 0.15	70.89
< -0.20	61.33	< 0.20	71.33
< -0.15	64.24	< 0.25	71.50
< -0.10	68.78	< 0.30	71.42
< -0.05	70.02	< 0.35	70.79
< 0	70.52	< 0.40	69.49
< 0.05	70.52	< 0.45	68.69

Table 5.1: f values, defined in 5.3, for different ISO cuts.

5.4 m(Λ_c^*)-m(Λ_c^+)

The $\Delta m = m(\Lambda_c^*) - m(\Lambda_c^+)$ distribution of LHCb data, in the range of [280,380] MeV/c is plotted in figure 3.4. The data sample is identified form final states formed of $\Lambda_c^{*+}\mu^-$ reconstructed tracks which passes all steps of the selection illustrated in chapter 3.
This variable allows to identify the presence of decays containing one of the two resonances $\Lambda_c^+(2595)$ or $\Lambda_c^+(2625)$, correspondent respectively to the lower and the higher Δm peak of the distribution.
Events defined by Δm out of the peaks are composed of Λ_c^* fake and then they form a component of the combinatorial background (subsection 3.17). Therefore, a fit to the Δm in the data allow to extract the number of combinatorial background event under the resonances.
Moreover, thanks to fit to Δm distribution of a sample composed of $\Lambda_c^{*+}\mu^+$ (wrong charge sample (subsection 3.17)), the muons misidentification component of background can be extracted, as explained in subsection 5.4.2.
The PDF used to fit the Δm data distribution is built:

$$P(\Delta m) = N_{\Lambda_c^+(2595)} S_{\Lambda_c^+(2595)}(\Delta m) + N_{\Lambda_c^+(2625)} S_{\Lambda_c^+(2625)}(\Delta m) + N_{comb} B(\Delta m) \tag{5.3}$$

where N_i (i= $\Lambda_c^+(2595)$, $\Lambda_c^+(2625)$, comb) are the events respectively fitted around the expected peak for the lower and higher Λ_c^+ resonance and the number of combinatorial background events. Then, $S_{\Lambda_c^+(2595)}$ and $S_{\Lambda_c^+(2625)}$ are the PDF which describe the peaks events and B, the background PDF.

The fit components are modeled using the following PDFs:

- $S_{\Lambda_c^+(2595)}(\Delta m)$:

$$S_{\Lambda_c^+(2595)}(\Delta m) = P_{Bifurcated\_Gauss} + (1 - f_{2595})P_{Breit\_Wigner} \quad (5.4)$$

where

– $P_{Bifurcated\_Gauss}(\Delta m; \Delta m_{\Lambda_c^+(2595)\_BIF}; \sigma) =$

$$= \begin{cases} \frac{1}{\sigma_L\sqrt{2\pi}} e^{\Delta m - \frac{(-\Delta m_{\Lambda_c^+(2625)\_BIF})^2}{2\sigma_L^2}} & \Delta m < \Delta m_{\Lambda_c^+(2595)\_BIF} \\ \frac{1}{\sigma_R\sqrt{2\pi}} e^{-\left(\frac{(\Delta m - \Delta m_{\Lambda_c^+(2625)\_BIF})^2}{2\sigma_R^2}\right)} & \Delta m > \Delta m_{\Lambda_c^+(2595)\_BIF} \end{cases}$$

defined by $\Delta m_{\Lambda_c^+(2595)\_BIF}$ is the mean value, widths σ_L and σ_L.

– $P_{Breit\_Wigner}(\Delta m, \Delta m_{\Lambda_c^+(2595)\_BW}, \Gamma) =$

$$\frac{1}{2\pi} \frac{1}{(\Delta m - \Delta m_{\Lambda_c^+(2595)\_BW})^2 + (\Gamma/2)^2}$$

where $\Delta m_{\Lambda_c^+(2595)\_BW}$ is the central mass and Γ is the width of the resonances.

- $S_{\Lambda_c^+(2625)}(\Delta m)$:

– $P_{Double\_Gaussian}(\Delta m; \Delta m_{\Lambda_c^+(2625)\_DG}; \sigma_1; \sigma_2) =$

$$= \frac{f_{2625}}{\sigma_1\sqrt{2\pi}} e^{-\left(\frac{(\Delta m - \Delta m_{\Lambda_c^+(2625)\_DG})^2}{2\sigma_1^2}\right)} + \frac{(1 - f_{2625})}{\sigma_2\sqrt{2\pi}} e^{-\left(\frac{(\Delta m - \Delta m_{\Lambda_c^+(2625)\_DG})^2}{2\sigma_2^2}\right)}$$

defined by same mean $\Delta m_{\Lambda_c^+(2625)\_DG}$, widths σ_1 and σ_2.

$\Lambda_c^{*+}\mu^-$

- $B(\Delta m)$:

– $B(\Delta m) = (\Delta m - \Delta m0)^p e^{\alpha(\Delta m - \Delta m0)}$
where $\Delta m0$ is the value for which $B(\Delta m0) = 0$, p and α two parameters.

In Figure 5.6 the plot of the fit to the Δm distribution on the 2012 data sample after applying selection illustrated in chapter 3 is shown in both bins of ISO, while in table 5.2 the results for the PDF parameters are reported. The aim of this thesis is not to study the decays containing $\Lambda_c^+(2595)$ in the final state, but only that including the $\Lambda_c^+(2625)$. This choice has been taken because of the limited statistic and the consequent few $\Lambda_c^+(2595)$ fitted. The lower resonance is however fitted, in order to prevent the corrected fit of the combinatorial background and the resulting overestimation of the last one.

Parameter	Fitted Value
$N_{\Lambda_c^+(2625)}$	37039 ± 1299
$\Delta m_{\Lambda_c^+(2625)\_DG}$	341.65 ± 0.02
σ_1	1.81 ± 0.06
σ_2	4.46 ± 0.46
f_{2625}	0.64 ± 0.04
N_{comb}	139502 ± 1901
α	- 0.0144 ± 0.0002
p	2.12 ± 0.01
$N_{\Lambda_c^+(2595)}$	16745 ± 409
$\Delta m_{\Lambda_c^+(2595)\_BW}$	306.51 ± 0.17
Γ	4.18 ± 0.25
σ_L	1.49 ± 0.14
σ_R	4.45 ± 0.46
f_{2595}	10.95 ± 0.08

Parameter	Fitted Value
$N_{\Lambda_c^+(2625)}$	4169 ± 290
$\Delta m_{\Lambda_c^+(2625)\_DG}$	341.64 ± 0.08
σ_1	1.99 ± 0.21
σ_2	4.73 ± 1.37
f_{2625}	0.64 ± 0.14
N_{comb}	50049 ± 506
α	- 0.012 ± 0.001
p	1.87 ± 0.06
$N_{\Lambda_c^+(2595)}$	2317 ± 227
$\Delta m_{\Lambda_c^+(2595)\_BW}$	306.75 ± 0.71
Γ	4.26 ± 1.33
σ_L	2.75 ± 0.47
σ_R	10.99 ± 0.92
f_{2595}	0.80 ± 0.07

Table 5.2: Parameters of the fit to Δm LHCb 2012 data distribution after applying the $ISO < 0.25$ (left), and $ISO \geq 0.25$ (right) .

5.4.1 Fake Λ_c^* Events Fit

A fit to the Δm variable in the data allows to extract the number of combinatorial background events composed of Λ_c^* fake under the resonances. As described in section 5.4, this combinatorial component can be described using the following PDF:

$$B(\Delta m) = (\Delta m - \Delta m0)^p e^{\alpha(\Delta m - \Delta m0)}$$

where $\Delta m0$ is the value for which $B(\Delta m0) = 0$, p and α two parameters. The fits, performed in every q^2 bins (section 5.2) for both the isolation bins

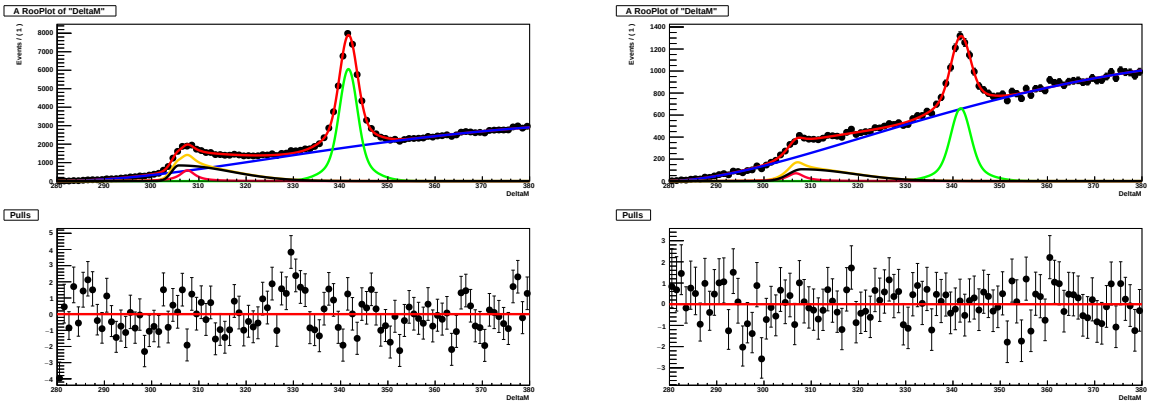

(a) $ISO < 0.25$ (b) $ISO \geq 0.25$

Figure 5.6: Fit to distribution of Δm LHCb 2012 data after applying $ISO < 0.25$ cut (left) and $ISO \geq 0.25$ cut (right). Table 5.2 shows the parameters fitted.

(section 5.3), are shown in Figures 5.7 and 5.8, while in Appendix A the results for the PDF parameters are reported. Instead, the distributions of these events, with respect to the variables described in the section 5.2 and the MVA output variables illustrated in the next section, both aimed to separate semitauonic from seminuonic Λ_b^0 decays, correspond to the LHCb data distributions in the Δm range $]360,380[$ MeV/c. In fact, as it is possible to see in Figures 5.7 and 5.8, all events characterized by a Δ_m included in this range are fitted by Λ_c^* fake combinatorial background PDF. The impact of the chosen Δm sideband range on the discriminating variables shapes is described in the subsection 6.3.1 .

5.4.2 Wrong charge sample: Estimation of Muon Misidentification Events

The Λ_b^0 events candidates constituted of a final state composed of a true Λ_c^* track and a muon track characterized form the same charge of the baryon, form the so called wrong sign sample. The Δm distribution of this sample allows to identify the peaks which correspond to candidate containing $\Lambda_c^+(2595)$ or $\Lambda_c^+(2625)$. After the fit, the background contribution can be removed from wrong sign sample weighting each event with its *sWeight*, the technique is explained in the following subsection. Thanks to this fit we

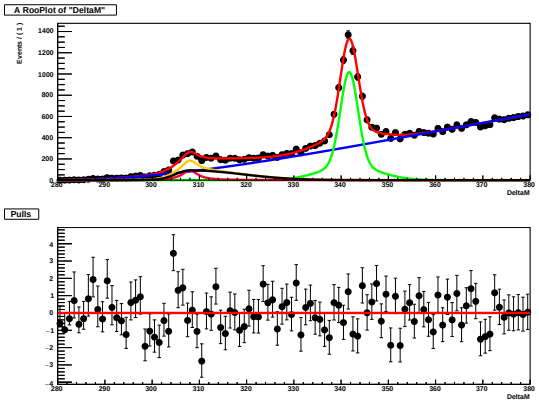

(a) $q^2 \in (-10, 1)(GeV/c)^2$

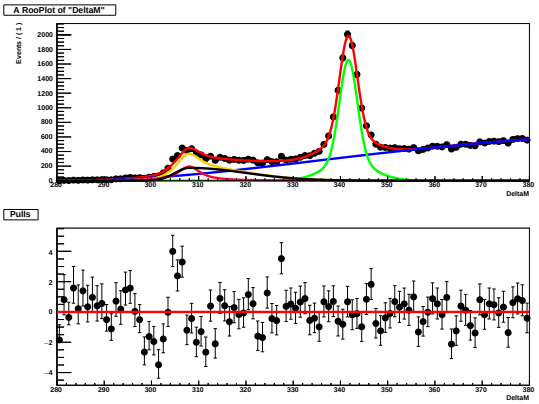

(b) $q^2 \in (1, 3)(GeV/c)^2$

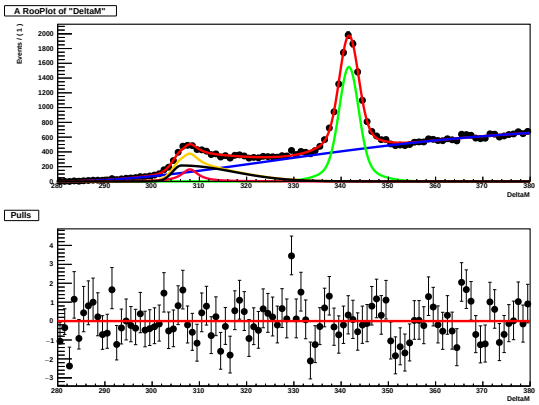

(c) $q^2 \in (3, 5)(GeV/c)^2$

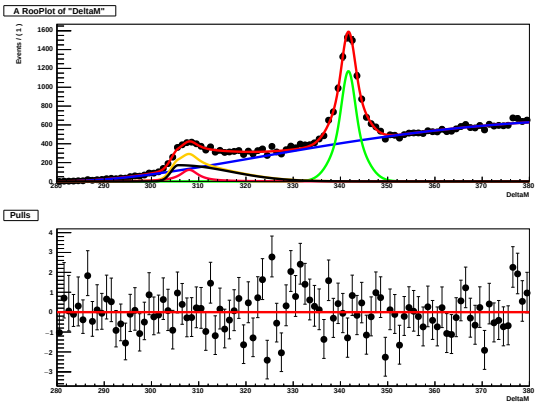

(d) $q^2 \in (5, 7)(GeV/c)^2$

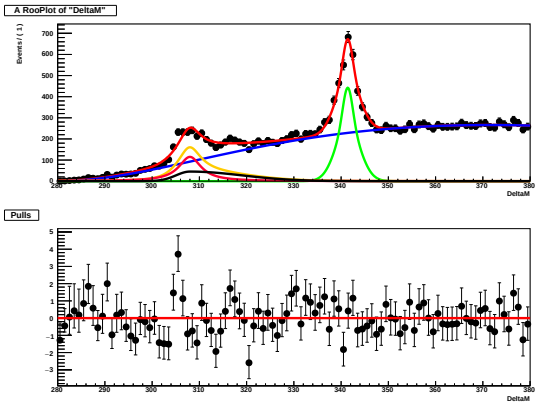

(e) $q^2 \in (7, 10)(GeV/c)^2$

Figure 5.7: Fit to distribution of Δm LHCb 2012 data after applying $ISO < 0.25$ in q^2 bins:$S_{\Lambda_c^+(2595)}$(orange), $P_{Bifurcated\_Gauss}$(black), P_{Breit_Wigner}(light red), $S_{\Lambda_c^+(2625)}$(green) and B_{comb} (blue). Appendix A shows the parameters fitted.

can know the number of events formed of a true Λ_c^* track composed with a wrong charge muon which can not be signal-like but only events with a muon

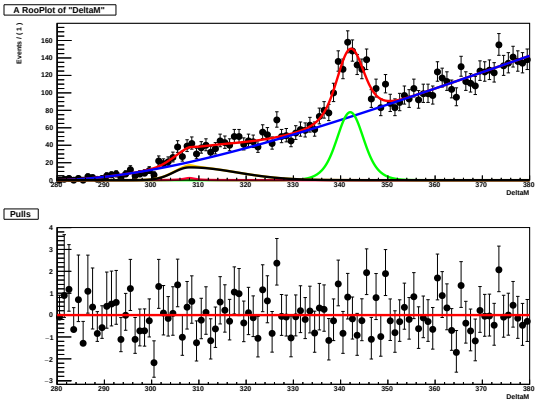

(a) $q^2 \in (-10, 1)(GeV/c)^2$

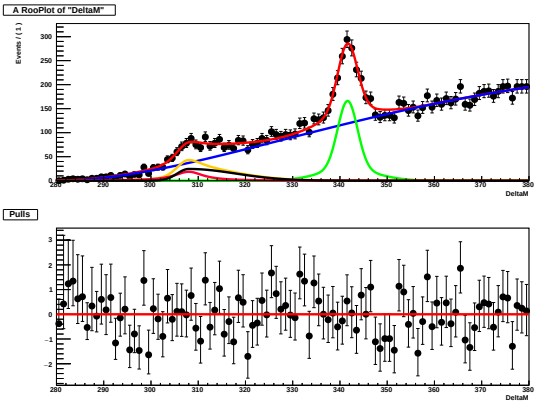

(b) $q^2 \in (1, 3)(GeV/c)^2$

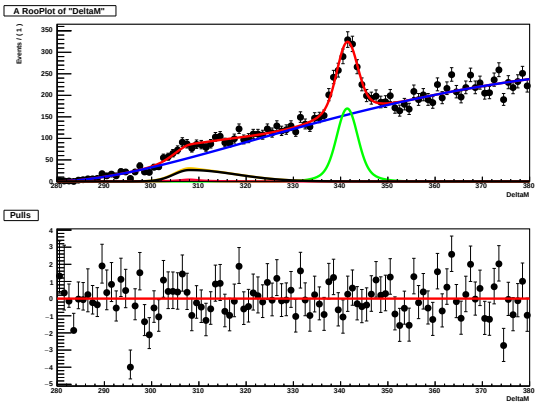

(c) $q^2 \in (3, 5)(GeV/c)^2$

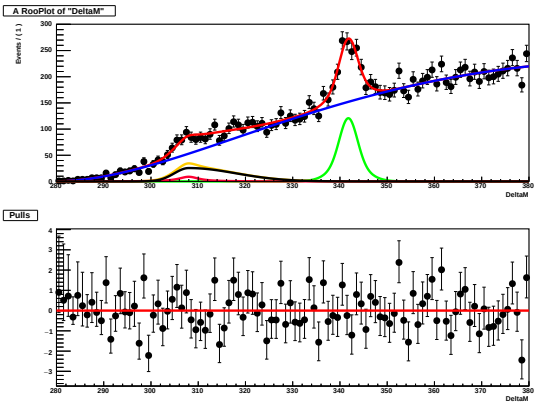

(d) $q^2 \in (5, 7)(GeV/c)^2$

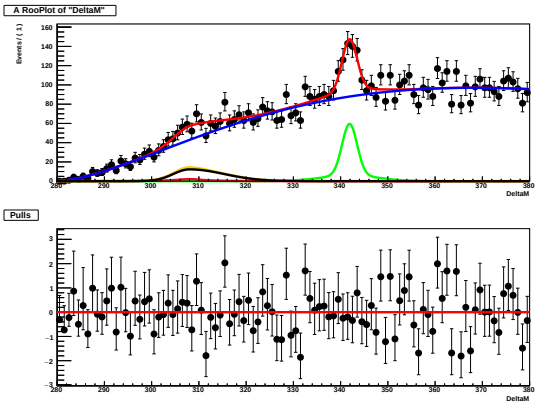

(e) $q^2 \in (7, 10)(GeV/c)^2$

Figure 5.8: Fit to distribution of Δm LHCb 2012 data after applying $ISO \geq 0.25$ in q^2 bins:$S_{\Lambda_c^+(2595)}$(orange), $P_{Bifurcated\_Gauss}$(black), P_{Breit_Wigner}(light red), $S_{\Lambda_c^+(2625)}$(green) and B_{comb} (blue). Appendix A shows the parameters fitted.

misidentified. Since the topology of these decays and the selection applied are the same to that searched for our signal candidate ($\Lambda_c^{*+}\mu^-$ final state),

we can assume that the muon misidentification component of background in $\Lambda_c^{*+}\mu^-$ final state data is equal to the number of events and has the same the kinematic distributions of the wrong sign sample.

The wrong sign sample is fitted using the same PDFs for combinatorial background, while the events peaking to the $\Lambda_c^+(2595)$ and the $\Lambda_c^+(2625)$ are described using a Gaussian. The fits, performed in every q^2 bins (section 5.2) for both the isolation bins (section 5.3), are shown in Figures 5.9 and 5.10, while in Appendix B the results for the PDF parameters are reported.

5.4.2.1 *sPlot*

The sPlot technique [46] allows to reconstruct *priori* unknown distributions of some variables (control variables) independently for each of the various species of events, inferring the knowledge available for a set of discriminating variables. In particular, it is performed on the data sample to determine the yields of the various sources. It can be applied when:

- The set of discriminating variables must have a good discrimination power.
- The control variable has to be uncorrelated with the discriminating set.

This technique exploits the maximum Likelihood method using the discriminating variables. The used log-Likelihood is:

$$L = \sum_{e=1}^{N} ln \left\{ \sum_{i=1}^{N_s} N_i f_i(y_e) \right\} - \sum_{i=1}^{N_s} N_i \tag{5.5}$$

where

- N is the total number of events considered;
- N_s is the number of species of events populating the data sample (signal and background);
- N_i is the number of events expected on the average for the i^{th} species;
- y represents the set of discriminating variables;

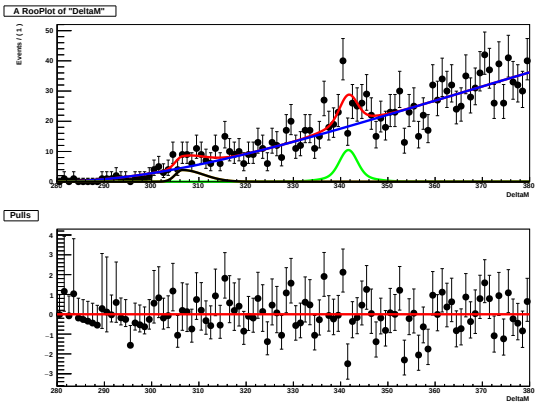

(a) $q^2 \in (-10, 1)(GeV/c)^2$

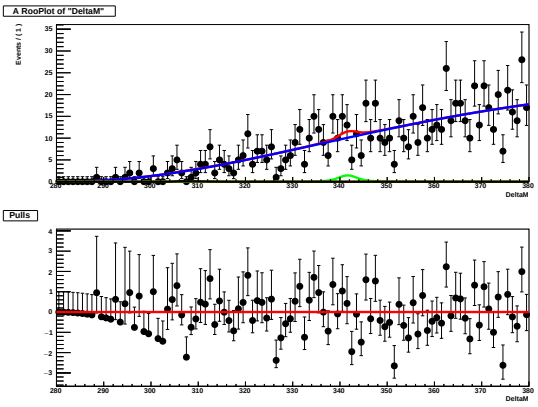

(b) $q^2 \in (1, 3)(GeV/c)^2$

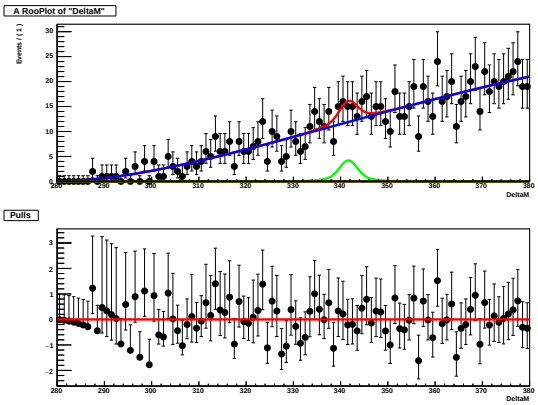

(c) $q^2 \in (3, 5)(GeV/c)^2$

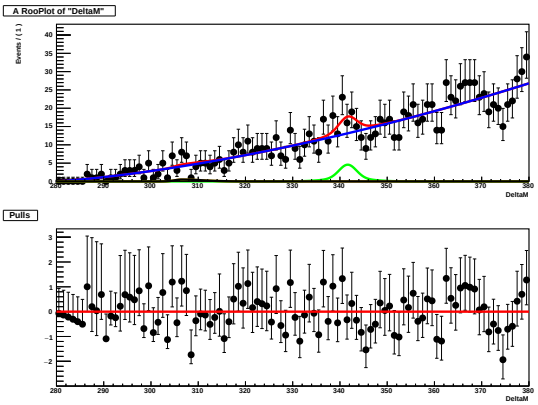

(d) $q^2 \in (5, 7)(GeV/c)^2$

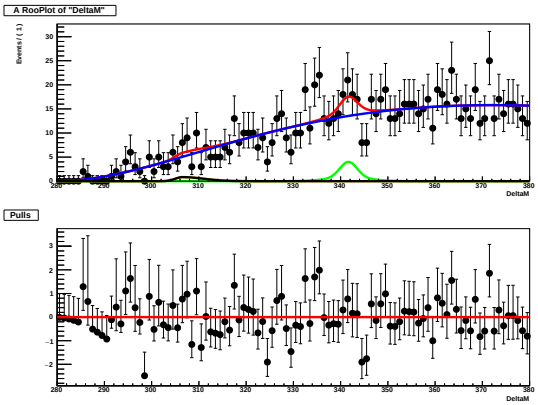

(e) $q^2 \in (7, 10)(GeV/c)^2$

Figure 5.9: Fit to distribution of Δm WS distribuition after applying $ISO < eq0.25$ in q^2 bins:$S_{\Lambda_c^+(2595)}$(light red), $P_{Gaussian}$(black), $S_{\Lambda_c^+(2625)}$(green) and B_{comb} (blue). Appendix B shows the paramters fitted about od each bin fit.

- f_i is the Probability Density Function (PDF) of the discriminating variables for the i^{th} species;

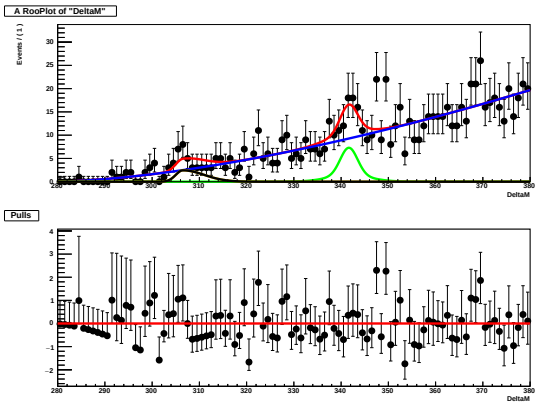

(a) $q^2 \in (-10, 1)(GeV/c)^2$

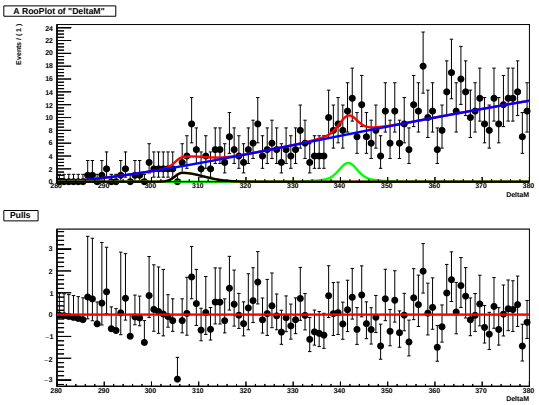

(b) $q^2 \in (1, 3)(GeV/c)^2$

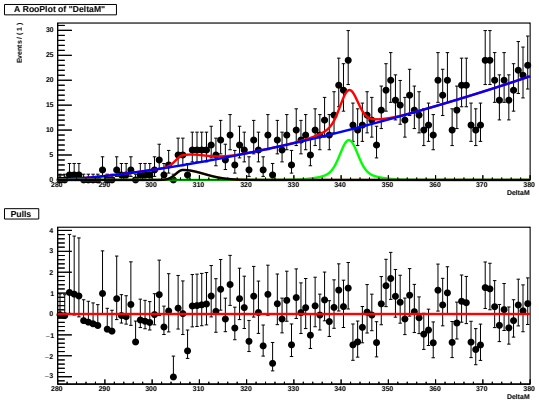

(c) $q^2 \in (3, 5)(GeV/c)^2$

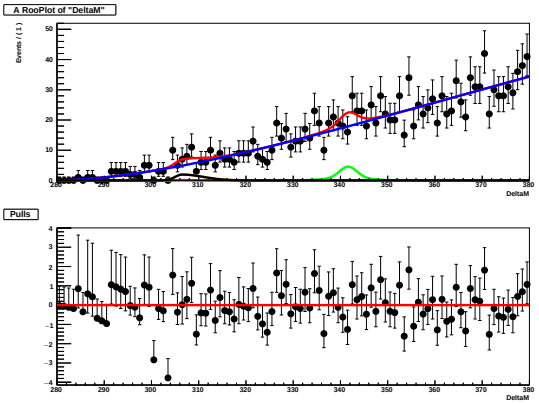

(d) $q^2 \in (5, 7)(GeV/c)^2$

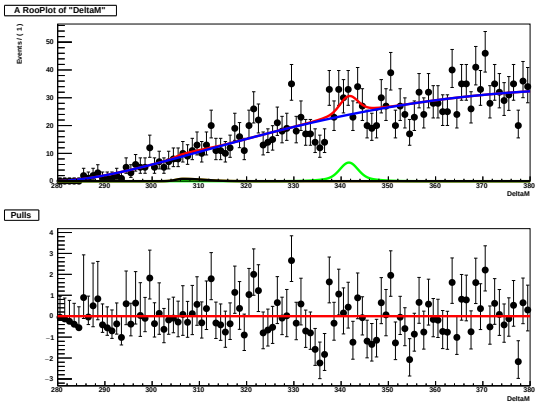

(e) $q^2 \in (7, 10)(GeV/c)^2$

Figure 5.10: Fit to distribution of Δm WS distribution after applying $ISO \geq 0.25$ in q^2 bins:$S_{\Lambda_c^+(2595)}$(light red), $P_{Gaussian}$(black), $S_{\Lambda_c^+(2625)}$(green) and B_{comb} (blue). Appendix B shows the paramters fitted about od each bin fit.

- $f_i(y_e)$ is the value of the pdf of y for the i^{th} species and for the e^{th} events.

Through the maximization of the log-Likelihood all implicit free parameters designed to tune the PDFs on data sample and the N_i yealds are determined. It is so possible to build a weight for each event to be of the i^{th} species, called *sWeight*, that can be calculated as:

$$ {}_sP_i(y_e) = \frac{\sum_{j=1}^{N_s} V_{ij} f_j(y_e)}{\sum_{j=1}^{N_s} N_k f_k(y_e)} \tag{5.6} $$

where V is the likelihood covariance matrix between species i and j defined as:

$$ V_{ij}^{-1} = \frac{\partial^2(-L)}{\partial N_i \partial N_j} = \sum_{e=1}^{N} \frac{f_i(y_e) f_j(y_e)}{(\sum_{j=1}^{N_s} N_k f_k(y_e))^2} \tag{5.7} $$

This technique allow to unfold the contributions of background and signal. In this thesis, is applied to identify the combinatorial background due to muon misidentification.

5.5 Separation of $\Lambda_b^0 \to \Lambda_c^* \tau^- \bar{\nu}_\tau$ from $\Lambda_b^0 \to \Lambda_c^* \mu^- \bar{\nu}_\mu$ decays

The separation of $\Lambda_b^0 \to \Lambda_c^* \tau^- \bar{\nu}_\tau$(signal channel) from $\Lambda_b^0 \to \Lambda_c^* \mu^- \bar{\nu}_\mu$ decays (normalization channel) can be distinguished in two steps. Both of them are based on multivariate methods and exploit, for the most part, the variable described in section 5.2.

Firstly, a Fisher discriminant with Gaussian transformed input variables is used, build to exploit the different features of Λ_b^0 decay vertex in semitauonic and semimuonic decays. At one second stage, the output of the previous algorithm and the variables connected to the kinematic characteristics of two considered decays are the inputs of a Multi-Layer Perceptron. This two methods are chosen since they imply the best performance with respect to the others tested, as it will explain in the following subsections.

The multivariate analysis are performed using the Toolkit for Multivariate Analysis (TMVA) [47], an environment which allows the processing, the evaluation and the application of a variety of different machine learning algorithms. They make use of training events, generally MC events, for which the desired output is known to determine the mapping function that describes a

decision boundary.
It can be happens that a machine learning problem has too few degrees of freedom when a many input parameters of an algorithm try to be adjusted with few data point. This phenomenon is called overtraining and leads to a fake increment of classification performance. Then a test in every TMVA method is implemented to evaluate if the overtraing is occurring. After learning, the sample is divided in two piece, training and testing sample. The procedure to separation is recalculated on the testing events and compared to the one for training. If the performance on training sample results significantly better, the chosen procedure results sensitive to statistical fluctuations and the overtraining is occurring.

5.5.1 Fisher Discriminant

5.5.1.1 Fisher Discriminant Method

The Fisher Discriminant method [48] is a linear classifier, performed in a transformed variable space with zero linear correlations. In a linear discriminant analysis an axis is found in the input variable hyperspace such that when events are projected on the axis, signal and background events are pushed as far as possible from each other, while events in the same class are kept close together. The metric for determining this separation is the covariance matrix of the variable space.
A Fisher coefficient F_K is determined for each variable K such that:

$$F_k = \frac{\sqrt{N_S N_B}}{N_S + N_B} \sum_{i=1}^{n_{var}} W_{Kl}^{-1} (\bar{x}_{S,i} - \bar{x}_{B,i})$$

where N_S and N_B are the number of signal and background events, $\bar{x}_{S,i}$ and $\bar{x}_{B,i}$ are the variable means in the signal and background classes and W_{Kl} is the sum of the signal and background covariance matrices.
The Fisher classifier response for an m event is then given by;

$$y_{Fisher}(m) = F_0 + \sum_{i=1}^{n_{var}} F_i x_i(m)$$

where F_0 is an offset which set the average Fisher response across both signal and background samples to zero.
In order to achieve the greatest separation power from the Fisher Discriminant, transformations can be applied to each input variables. The Fisher method is most effective when the input variables are linearly correlated Gaussian distributions. Therefore, a transformation can be applied to each input variable, that when applied to the signal distribution, gives a Gaussian shaped output. The found transformation is then applied to both signal and background distribution for each variable (Gaussianization). This optimization is applied using the FisherG discriminant inside the TMVA toolkit.
The covariant matrix can be decomposed into the sum of the matrix which describes the dispersion of events relative to the means of their own class (within-class matrix) and that one concerning on the overall sample mean (between-class matrix). The aims of a Fisher discriminant analysis is of maximizing the between-class separation while minimizing the within-class dispersion; therefore a measure of the discrimination power of a variable is given by the ratio of between-class matrix and the overall covariance matrix. This quantity is used to determine the ranking of the input variables.

5.5.1.2 Discriminant Based on Vertex Features

Using the TMVA toolkit [47] many multivariate analysis have been performed to find the best method which allow to discriminate the $\Lambda_b^0 \to \Lambda_c^* \tau^- \bar{\nu}_\tau$ signal decay from the normalization/background $\Lambda_b^0 \to \Lambda_c^* \mu^- \bar{\nu}_\mu$ events. The TMVA classificator algorithm is trained on a signal-like MC events sample ($\Lambda_b^0 \to \Lambda_c^* \tau^- \bar{\nu}_\tau$) and on a background-like MC sample composed of $\Lambda_b^0 \to \Lambda_c^* \mu^- \bar{\nu}_\mu$ events, that have to pass the selection procedure described in chapter 3 and for which the MC match on the decays is required.
The feature which differentiates mainly the semimuonic decays with respect to the semitauonic decays considered, is the final muon that is produced, in the first case directly from a Λ_b^0 decay and in the second are from $\tau \to \mu$ decays. It is, then, expected that the quality with which the Λ_b^0 decay vertex ($\chi^2_{vtx}(\Lambda_b^0)$) will be reconstructed will be more accurate and the error ($\sigma_z(\Lambda_b^0)$)

smaller for the first decays respect to the second type. Moreover, for the semitauonic decay, the muon, deriving from a secondary decays should have a larger impact parameter with respect to PV $log(\chi^2_{IP}(\mu))$ and should form a larger angle ($\mu\_cos\theta$) with respect to Λ_b^0 decay direction than one from semimuonic. For this reason, a TMVA classification analysis is build using as input the previous cited variables. The distributions put in input to the classification algorithm are visible in Figure 5.11. Moreover, Figure 5.12 shows that the chosen variables are weakly correlated each other in both channel.

Several methods are tested, as it is shown in Figure.5.13 which reproduces

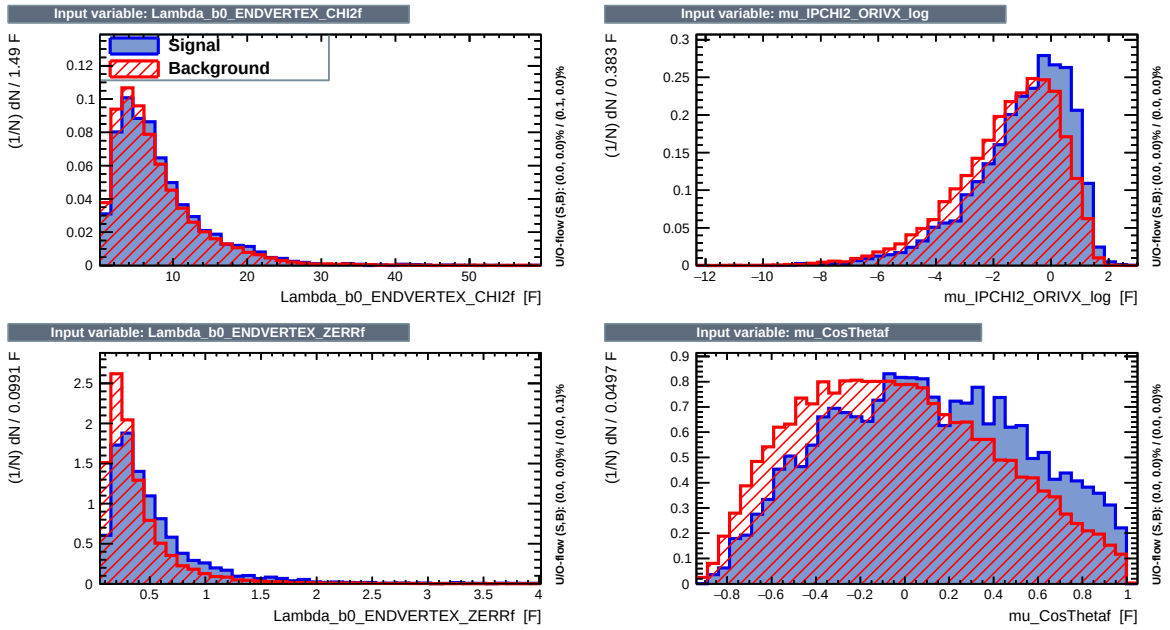

Figure 5.11: Discriminant based on vertex properties - FisherG input variables distributions separately drawn for simulated signal $\Lambda_b^0 \to \Lambda_c^* \tau^- \bar{\nu}_\tau$ decays (signal) and simulated background events of $\Lambda_b^0 \to \Lambda_c^* \mu^- \bar{\nu}_\mu$ (red). Top-left side: $\chi^2_{vtx}(\Lambda_b^0)$; top-right side: $log(\chi^2_{IP}(\mu))$; bottom-left side: $\sigma_z(\Lambda_b^0)$; bottom-right side: $\mu\_cos\theta$.

the power of rejection of semimuonic decays with respect to the efficiency to select the semitauonic one. From this figure it is possible to deduce that the best separation results applying a Fisher discriminant method with Gaussian transformation of input variables. Figure 5.14 reproduces the input variable to Fisher discriminant after Gaussianization, illustrated in 5.5.1.1. Moreover, Figure 5.12 shows that the chosen variable are weakly correlated each other.

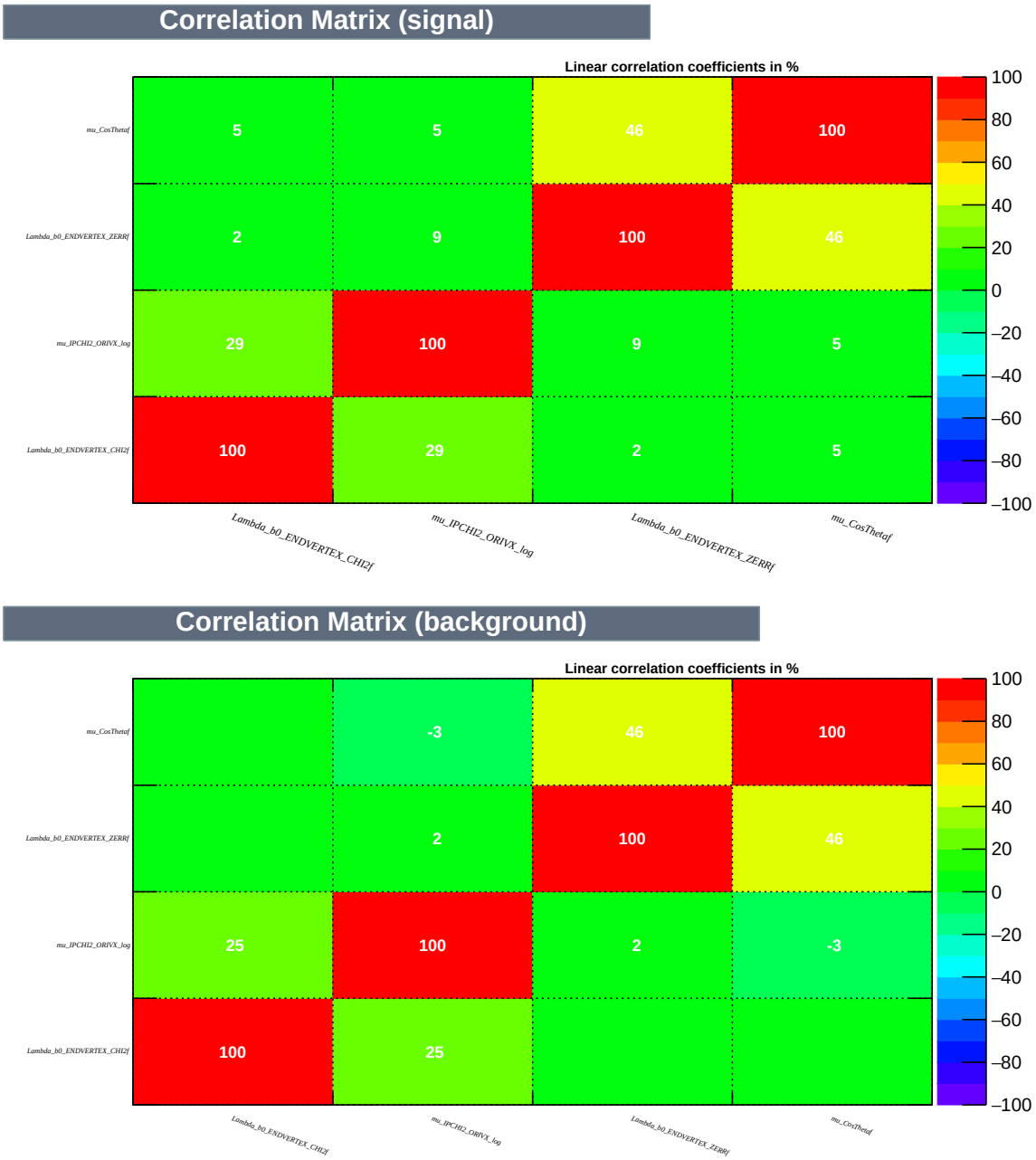

Figure 5.12: Discriminant based on vertex properties - Correlation matrix of the input variables, on the top side for the simulated $\Lambda_b^0 \to \Lambda_c^* \tau^- \bar{\nu}_\tau$, in the bottom side concerning the simulated $\Lambda_b^0 \to \Lambda_c^* \mu^- \bar{\nu}_\mu$ decays.

Finally, in figure 5.15 the result of the test to ensure that the analysis result is not overtrained (see introduction of this section) is displayed. The Table 5.3 reports the ranking of the input variable and the separation power, calculated according technique illustrated in 5.5.1.1. This learning methods is applied to all simulated sample (semitauonic, semimuonic and double

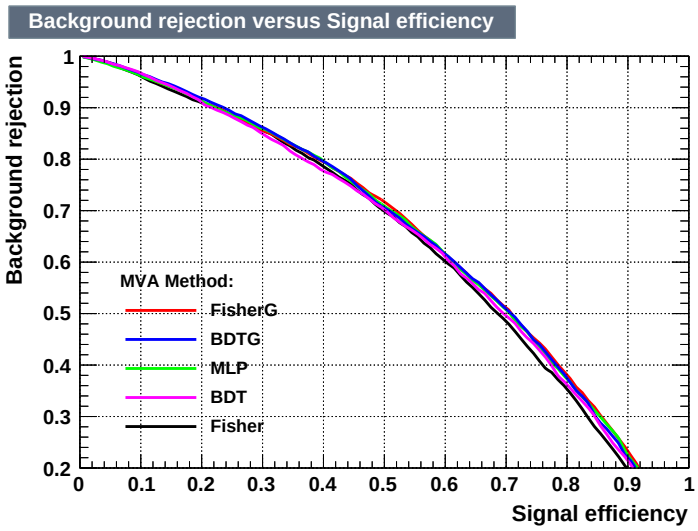

Figure 5.13: Discriminant based on vertex features - $\Lambda_b^0 \to \Lambda_c^* \mu^- \bar{\nu}_\mu$ (background) rejection with respect selection efficiency of $\Lambda_b^0 \to \Lambda_c^* \tau^- \bar{\nu}_\tau$ (signal).

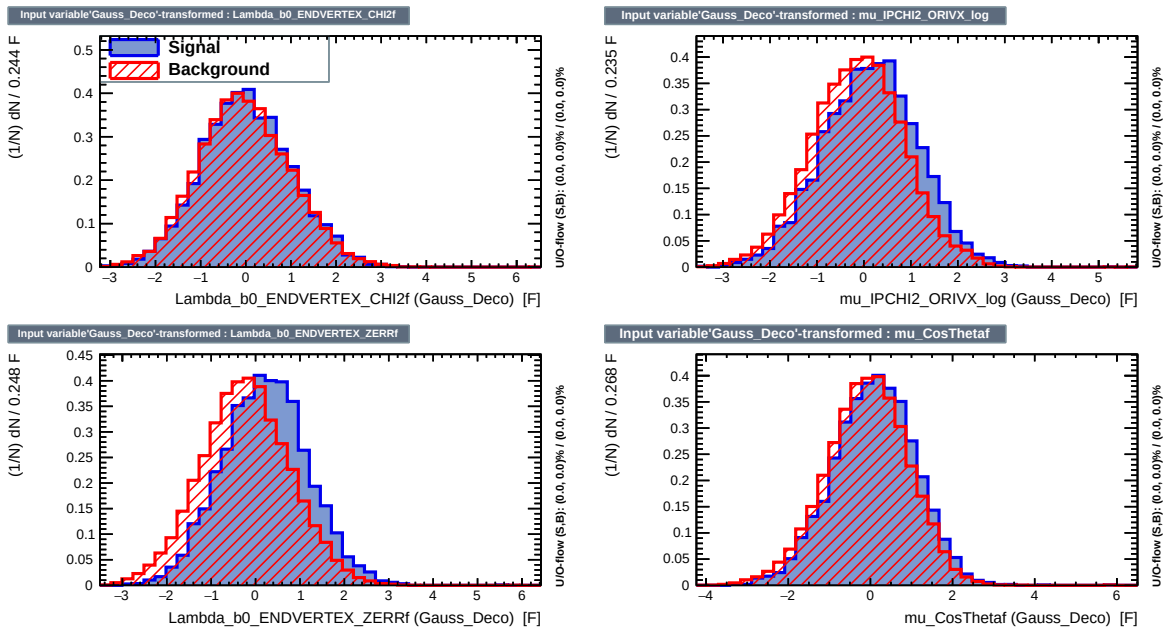

Figure 5.14: Discriminant based on vertex properties - FisherG input variables distributions after Gaussianisation separately drawn for simulated signal $\Lambda_b^0 \to \Lambda_c^* \tau^- \bar{\nu}_\tau$ decays (blue) and simulated background events of $\Lambda_b^0 \to \Lambda_c^* \mu^- \bar{\nu}_\mu$(red).Top-left side: $\chi^2_{vtx}(\Lambda_b^0)$; top-right side: $log(\chi^2_{IP}(\mu))$; bottom-left side: $\sigma_z(\Lambda_b^0)$; bottom-right side: $\mu\_cos\theta$.

charmed samples), to data, to sideband of data which describes the combinatorial background and to the wrong charge sample. The output variable FisherG it is used as input of an artificial neural network which combines vertex features of the considered decays with kinematics.

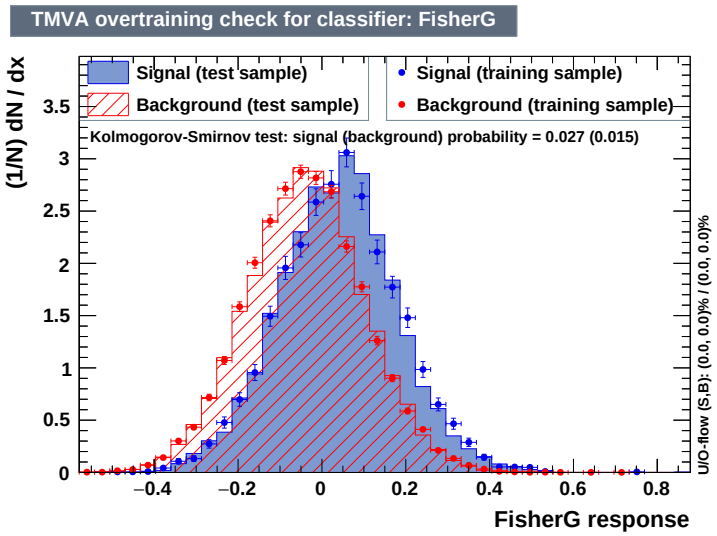

Figure 5.15: Discriminant based on vertex properties - TMVA overtraining check for FisherG classifier. Signal corresponds to $\Lambda_b^0 \to \Lambda_c^* \tau^- \bar{\nu}_\tau$ decays and backgorund to $\Lambda_b^0 \to \Lambda_c^* \mu^- \bar{\nu}_\mu$.

Rank	Variable	Separation Power
1	$\sigma_z(\Lambda_b^0)$	2.956×10^{-2}
2	$log(\chi^2_{IP}(\mu))$	1.086×10^{-2}
3	$\mu\_cos\theta$	1.057×10^{-2}
4	$\chi^2_{vtx}(\Lambda_b^0)$	1.269×10^{-3}

Table 5.3: Separation Power of the input variables of FisherG.

5.5.2 The Artificial Neutral Network Classifier

5.5.2.1 Multi-Layer Perceptron

The artificial neural network, ANN, is a supervised learning algorithm that learns a function. It can be described as a series of non linear functional transformations from a set of input variables x_i to a set of output variables y_k controlled by a vector $\vec{w}$ of adjustable parameters, the network weights [49]. They are structured in layers. Each layer consists of neurons, where a neuron is linear o not linear function, that maps the input neuron on the output one. The basic structure is given by three layers; input, hidden and an output layer. The input variables x_i are connected to the neurons of the input layer $f^{(1)}(x_i)$ and linearly mapped on the outputs of the first layers y_i:

$$y_i^{(1)} = f^{(1)}(x_i); \qquad f^{(1)}(x_i) = \alpha x_i + \beta.$$

The input of the of the second layer called activations a_j are build forming m linear combinations of the output of first layer:

$$a_j = w_{j0}^{(1)} + \sum_{i=1}^{n} w_{ji}^{(1)} y_i^{(1)}$$

where $w_{ji}^{(1)}$ are the weights used to adjust the training process and the $w_{j0}^{(1)}$ are the biases weight used to stabilize the same process. The activations a_j are transformed using a differentiable, non linear activation function $f^{(2)}(a_j)$, (=tanh in our case) to yield the output $y_j^{(2)}$ of the second layer:

$$y_j^{(2)} = f^{(2)}(a_j); \quad f^{(2)}(a_j) = tanh(a_j)$$

To obtain the input of the third layer, k linear combinations are built of the outputs of the second layer to form the activations a_k and the correspondent activation function is:

$$a_k = w_{k0}^{(2)} + \sum_{k=1}^{n} w_{kj}^{(2)} y_j^{(2)}$$

$$y_{ANN} = f^{(2)}(a_k)$$

Hence, combining the various stages the overall network functions take the form:

$$y_k(\vec{x}, \vec{w}) = f^{(2)}(\sum_{j=1}^{m} w_{ki}^{(2)} f^{(2)}(\sum_{i=1}^{n} w_{ji}^{(1)} f^{(1)}(x_i) + w_{j0}^{(1)}) + w_{k0}^{(2)})$$

This function can be represented in the form of a network diagram as shown in Figure 5.16. The evaluation of the process can be interpreted as a forward propagation of information through the network, therefore the ANN are defined feed-forward. Moreover the ANN can be called multilayer perceptron(MLP), since each stage of neural network processing resembles the perceptron model.

The determination of the event weights occurs during the learning process. An error function E is minimized by adjusting the vector of weights $\vec{w}$:

$$E(x_1, ..., X_n|\vec{w}) = \sum_{a=1}^{N} E(x_a|\vec{w}) = \sum_{a=1}^{N} \frac{1}{2}(y_{ANN,a}(x_a, \vec{w}) - y_a)^2$$

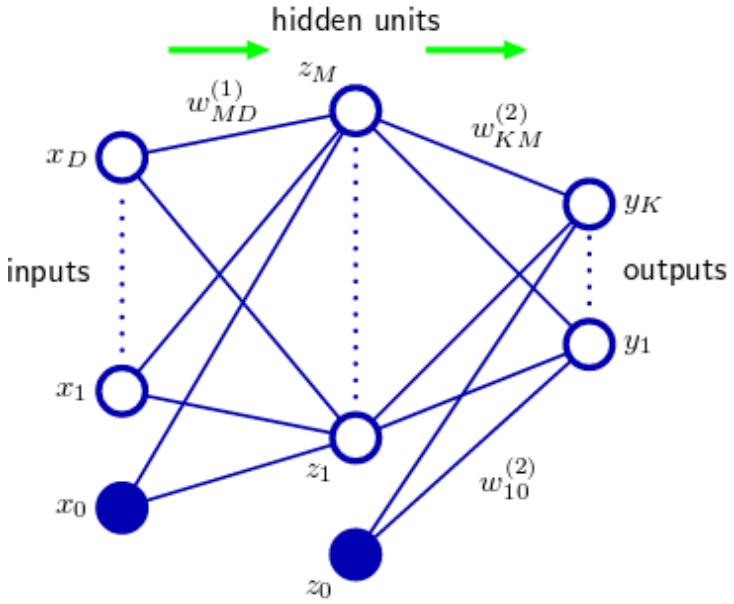

Figure 5.16: Network diagram for the a neural network with one hidden layer. The neurons are connected in feed forward structure [49]

where $E_a, a = 1, ..., N$ is the error function of a^{th} trained event, $y_{ANN,a}(x_a, \vec{w})$ is the network response computed from the vector of input variables $\vec{x}_a$ and weights $\vec{w}$ and finally y_a is the desired output, which is either 1 for signal and 0 for background.

Depending on the chosen of learning mechanism the optimal set of weights is found. The Broyden-Fletcher-Goldfarb-Shanno (BFGS) method [50], [51], [52], [53], used in this thesis, optimizes the weights iteratively using via the second derivatives of the Error function [49].

In order to determine the best ANN for a given problem, the importance I_i of each input variable x_i is determining using the weights between the input layer and the first hidden layer $w^{(1)}_{ij}$:

$$I_i = \bar{x}_i^2 \sum_{j=1}^{n_h} \left(w^{(1)}_{ij} \right)^2$$

where n_h is the neuron number and $\bar{x}$ the mean of input variable i.

5.5.2.2 Discriminant Based on Kinematic Features

A second process to learn is used to identify the to find the best method which allow to discriminate the $\Lambda_b^0 \to \Lambda_c^* \tau^- \bar{\nu}_\tau$ signal decay from the normalization/background $\Lambda_b^0 \to \Lambda_c^* \mu^- \bar{\nu}_\mu$ events using kinematics features. The TMVA classificator algorithm is trained on the signal-like MC events sample ($\Lambda_b^0 \to \Lambda_c^* \tau^- \bar{\nu}_\tau$) and on the background-like MC sample composed of $\Lambda_b^0 \to \Lambda_c^* \mu^- \bar{\nu}_\mu$ events, that have to pass the selection procedure described in chapter 3 and for which the MC match on the decays is required, as requested for event used in vertex discriminant. The parameters used as input, shown in Figure 5.17 are the energy of the muon in the Λ_b^0 center of mass, missing mass square, described in subsection 5.2, to which is added the output of vertex discriminator, the FigherG variable. Then, in Figure 5.18

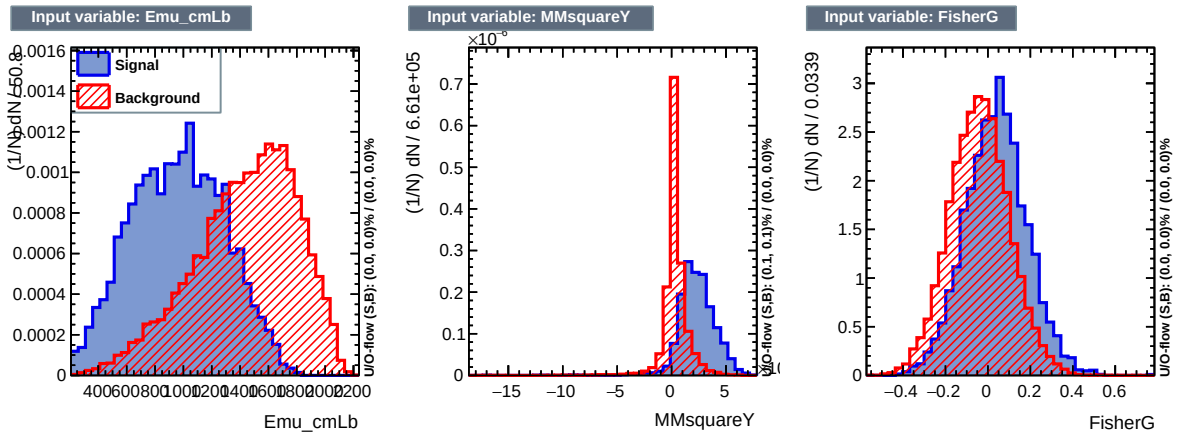

Figure 5.17: Discriminant based on kinematics properties - ANN input variables distributions separately drawn for simulated signal $\Lambda_b^0 \to \Lambda_c^* \tau^- \bar{\nu}_\tau$ decays (signal) and simulated background events of $\Lambda_b^0 \to \Lambda_c^* \mu^- \bar{\nu}_\mu$ (red): Energy of the muon in the Λ_b^0 center of mass (left), Missing Mass square (center), FigherG (right).

are displayed the matrix correlation about $\Lambda_b^0 \to \Lambda_c^* \tau^- \bar{\nu}_\tau$ signal decays and semimuonic normalization channel labeled as background. Also in this case, many multivariate technique are tried to select that one which allows the best rejection of Λ_b^0 semimuonic decays, maximizing the selection efficiency for that semitauonic. As shown in Figure 5.19, the more efficient approach result to be that takes in advantage of an artificial neural network. This method gives an answer 1 for signal and 0 for normalization channel events.

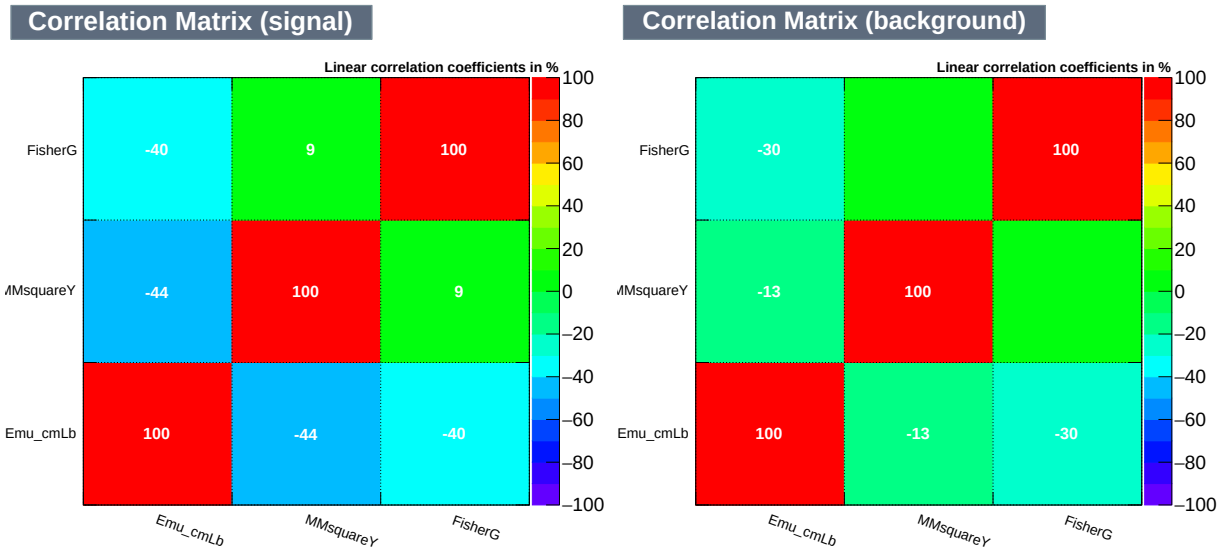

Figure 5.18: Discriminant based on kinematics properties - Correlation matrix of the variables, on the left side for the simulated $\Lambda_b^0 \to \Lambda_c^* \tau^- \bar{\nu}_\tau$, on the right side concerning the simulated $\Lambda_b^0 \to \Lambda_c^* \mu^- \bar{\nu}_\mu$ decays: on the x axis respectively the energy of the muon in the Λ_b^0 center of mass, the Missing Mass square and the FigherG.

Then, once trained it is able to provide a probability to be a signal events.

Figure 5.20 shows the result of the test to ensure that the analysis result

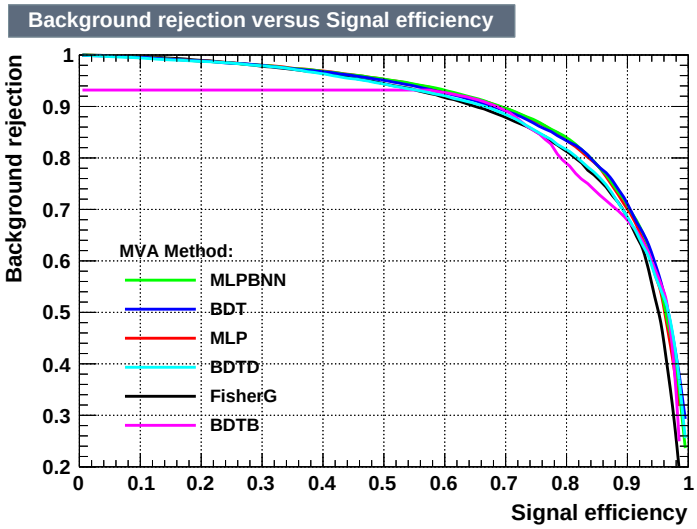

Figure 5.19: Discriminant based on kinematics properties - $\Lambda_b^0 \to \Lambda_c^* \mu^- \bar{\nu}_\mu$(background) with respect selection efficiency of $\Lambda_b^0 \to \Lambda_c^* \tau^- \bar{\nu}_\tau$ (signal).

is not overtrained (see introduction of this section). Finally in Table 5.4 are reported the ranking of the input variable and the separation power,

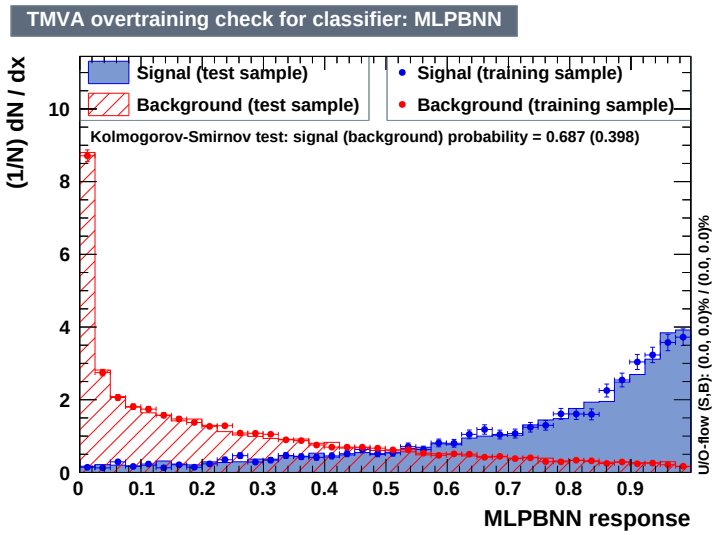

Figure 5.20: Discriminant based on kinematics properties - TMVA overtraining check for ANN classifier. Signal corresponds to $\Lambda_b^0 \to \Lambda_c^* \tau^- \bar{\nu}_\tau$ decays and backgorund to $\Lambda_b^0 \to \Lambda_c^* \mu^- \bar{\nu}_\mu$.

calculated according technique illustrated in 5.5.2.1. This learning meth-

Rank	Variable	Separation Power
1	MM^2	3.33×10^2
2	E^*	1.50
3	$FisherG$	1.49×10^{-2}

Table 5.4: Separation Power of the input variables of ANN.

ods is applied to all simulated sample (semitauonic, semimuonic and double charmed samples), to data, to sideband of data which describes the combinatorial background and to the wrong charge sample. The output variable, MLPBNN, is then fitted to extract the $R(\Lambda_c^*)$ ratio, aim of this thesis. The procedure is described in the next chapter.

5.6 Templates of The Discriminating Variables

In the figure 5.21 and 5.22, which only differ in the isolation cut, respectively $ISO < 0.25$ and $ISO \geq 0.25$, the distributions of all discriminating variables semitauonic from semimuonic decays and of the outputs of fisher discriminant and ANN are displayed. In each plots are superimposed the distributions of the $\Lambda_b^0 \to \Lambda_c^* \tau^- \bar{\nu}_\tau$, $\Lambda_b^0 \to \Lambda_c^* \mu^- \bar{\nu}_\mu$ and $\Lambda_b^0 \to \Lambda_c^* D_s^{(*)}$ simulated decays, of the

data, of the sideband of data which describes the combinatorial background and of the wrong charge sample. All distributions are normalized to unit, in order to visualized the shapes differences. The distributions of $\Lambda_b^0 \to \Lambda_c^* D_s^*$ and $\Lambda_b^0 \to \Lambda_c^* D_s$ in the next studies and in the MLPBNN fit are combined. The change of the MLPBNN fit results due to this combination has been taken into account in the systematical uncertainties.

5.6.1 $\Lambda_b^0 \to \Lambda_c^* \tau^- \bar{\nu}_\tau$ and $\Lambda_b^0 \to \Lambda_c^* D_s^{(*)}$

The process of discrimination performed by means of multivariate algorithms aimed to separate principally Λ_b^0 semitauonic decays from that one semimuonic. To evaluate as much as this discrimination allows to obtain separated template for Λ_b^0 double charmed decays with respect to that one semitauonic, we considered the efficiency of selecting a signal decay with respect to the efficiency of rejecting one charmed. As it is possible to see in figure 5.23, the chosen variables are useful in the separation of the two channels since the curvature is not a line.

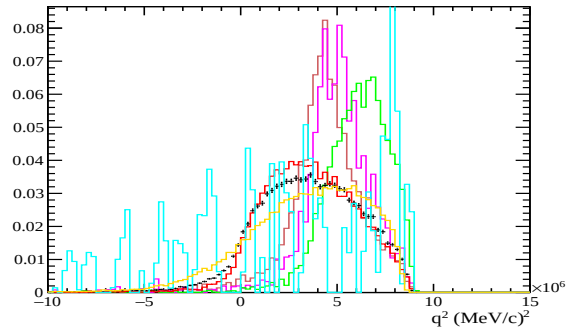

(a) Transferred Momentum

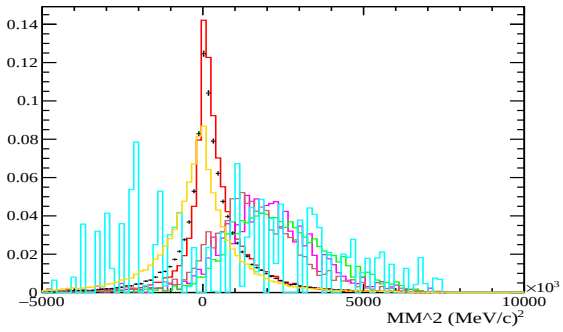

(b) Missing Mass Square

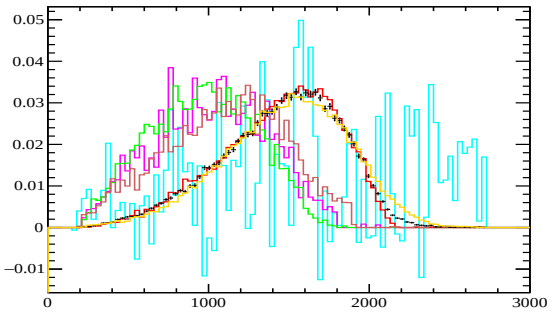

(c) E^*

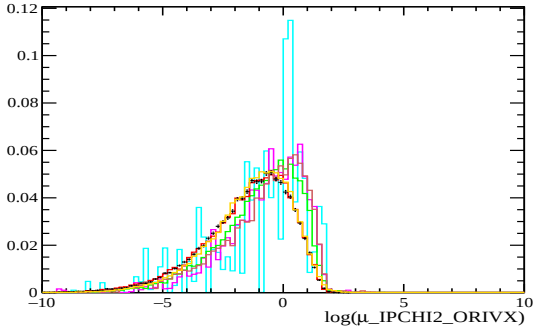

(d) $log(\chi^2_{IP}(\mu))$

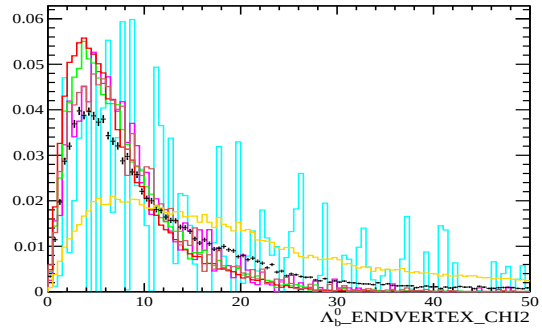

(e) $\chi^2_{vtx}(\Lambda_b^0)$

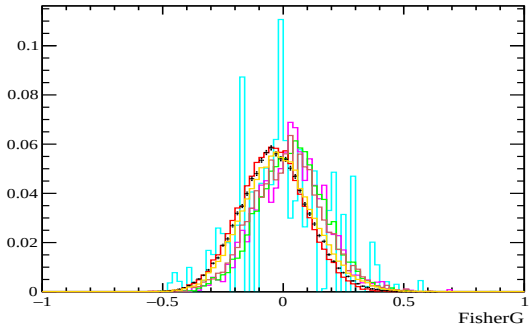

(f) FisherG

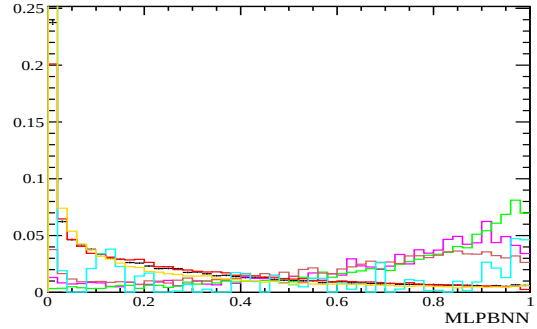

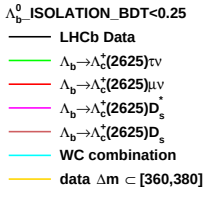

(g) MLPBNN

Figure 5.21: Distribution of variables used to measure the $R(\Lambda_c^*)$ ratio after applying the $ISO < 0.25$ cut. All templates are normalized to unit.

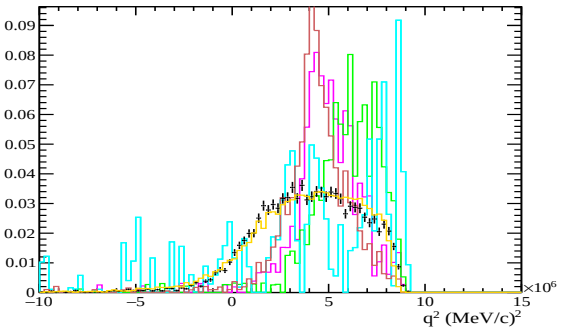

(a) Transferred Momentum

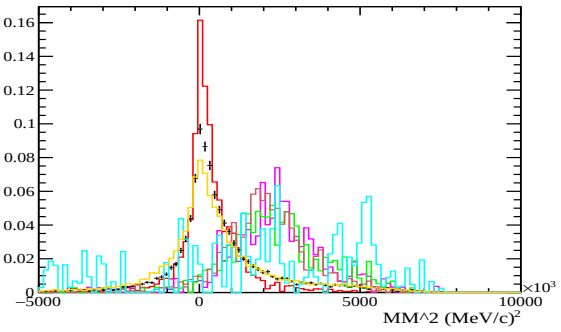

(b) Missing Mass Square

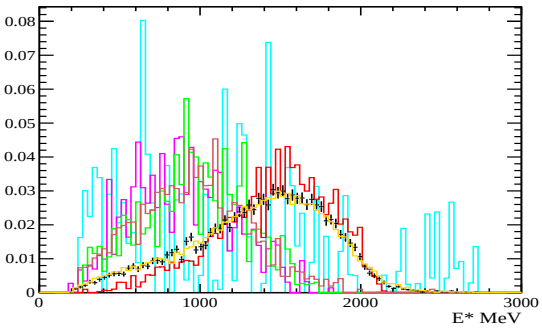

(c) E^*

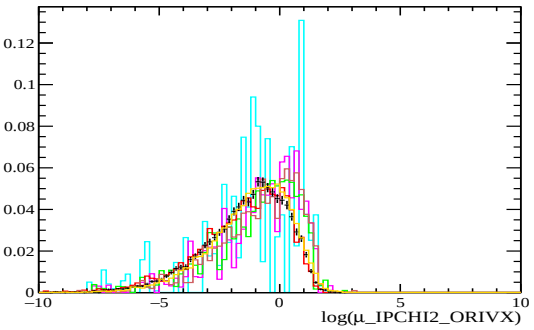

(d) $log(\chi^2_{IP}(\mu))$

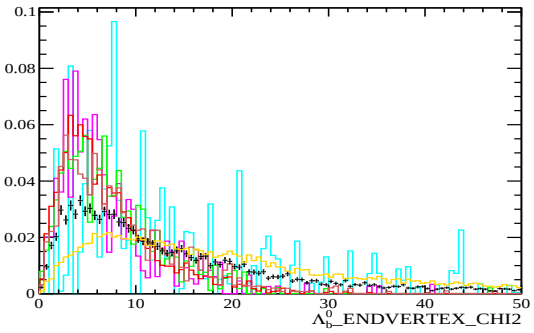

(e) $\chi^2_{vtx}(\Lambda_b^0)$

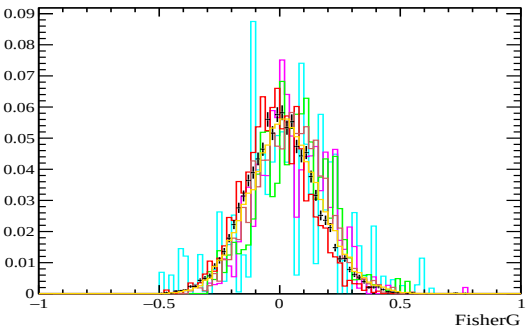

(f) FisherG

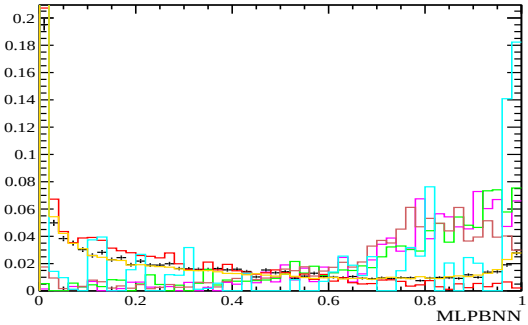

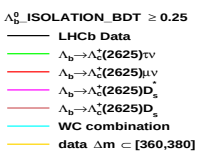

(g) MLPBNN

Figure 5.22: Distribution of variables used to measure the $R(\Lambda_c^*)$ ratio after applying the $ISO \geq 0.25$ cut. All templates are normalized to unit.

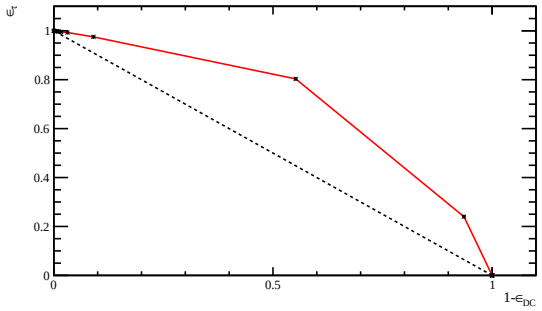

(a) Transferred Momentum

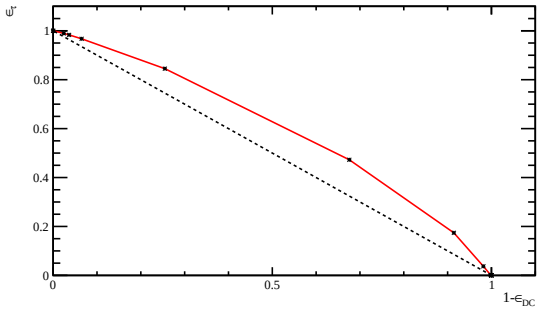

(b) Missing Mass Square

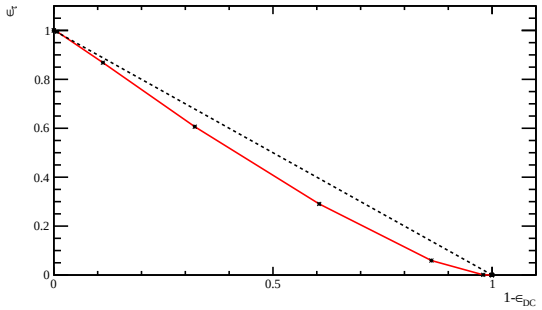

(c) E^*

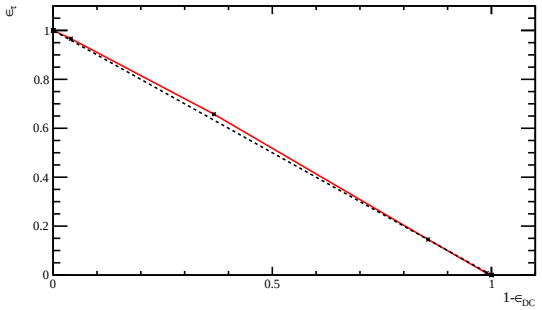

(d) FisherG

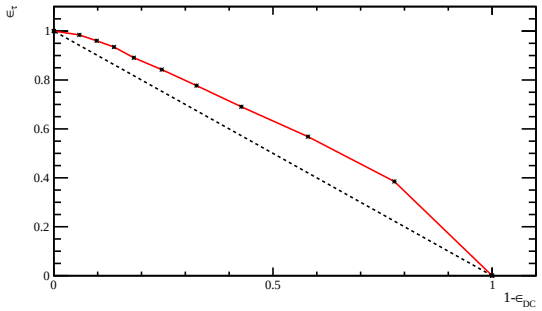

(e) MLPBNN

Figure 5.23: Ffficiency of selecting a signal decay with respect to the efficiency of rejecting one charmed for the variables used to discriminate semimuonic from semitauonic decays.

Chapter 6

The Extraction of R(Λ_c^*) ratio

This chapter is devoted to the extraction of the R(Λ_c^*) ratio with its uncertainties, by means of a fit to MLPBNN variable, already introduced in section 5.5.2.2. The fit is based on templates of $\Lambda_b^0 \to \Lambda_c^{*+}\tau^-\bar{\nu}_\tau$, $\Lambda_b^0 \to \Lambda_c^{*+}\mu^-\bar{\nu}_\mu$, double charmed Λ_b^0 decays, fake Λ_c^* and wrong sign components and it is implemented using the *HistFactory* tool, which is described in the next section. Then, an extended maximum likelihood fit is performed simultaneously on transferred momentum and isolation bins.

As said in chapter 4, only one double charmed Λ_b^0 template the fit has been inserted in the fit. It has been obtained adding the simulated distributions of $\Lambda_b^0 \to \Lambda_c^* D_s$ and of $\Lambda_b^0 \to \Lambda_c^* D_s^*$ and in all chapter will be referred as $\Lambda_b^0 \to \Lambda_c^* D_s$ template.

6.1 Extended Maximum Likelihood fits

The likelihood is defined as

$$\mathcal{L}(x_i, ..., x_N|\alpha_i, ..., \alpha_N) = \prod_{i=1}^{N} f(x_i|\alpha_i, ..., \alpha_N) \tag{6.1}$$

where $f(x_i|\alpha_i...\alpha_N)$ represents the probability density function of measuring x_i for a set of parameters $\alpha_i...\alpha_N$.

The method of maximum likelihood consists of maximizing the likelihood with respect to the set of parameters $\alpha_i...\alpha_N$. In practice it is more convenient to work with the logarithm of the likelihood function, called the

log-likelihood:

$$-ln\mathcal{L}(x_i, ..., x_N|\alpha_i, ..., \alpha_N) = \sum_{k=1}^{N} f(x_i|\alpha_i ... \alpha_N) \tag{6.2}$$

Thus the method of maximum likelihood is reduced to minimizing the previous equation.

Therefore, a maximum likelihood fit is used to determine the set of parameters which minimizes -ln$\mathcal{L}$ associated to a dataset. Moreover, if the parameters α_i are not independent on the number of expected events, it is necessary to include a Poisson term in the likelihood, which becomes:

$$\mathcal{L}(x_i, ..., x_N|\alpha_i, ..., \alpha_N) = e^{-\mathcal{N}} \frac{\mathcal{N}^N}{N!} \prod_{i=1}^{N} f(x_i|\alpha_i, ..., \alpha_N) \tag{6.3}$$

where $\mathcal{N}$ is the expected number of events and the observed number N is given by Poisson statistics. The likelihood fit method using equation 6.3, which considers the statistical power of the data sample, is called *Extended Maximum Likelihood fit*.

6.2 *HistFactory*

A fit based on templates is implemented using the *HistFactory* tool which is a ROOT tool, designed to build parametrized probability density functions based on simple histograms. The PDFs are built on a set of histograms implementing the different components, each one holding the number of events in a chosen region. Separate histograms are made for the nominal number of events and for each systematic variation; the systematic variations are modulated by nuisance parameters constrained by Gaussians [54].

6.3 Fit Templates

For each bin of transferred momentum and isolation evaluated, about the $\Lambda_b^0 \to \Lambda_c^* \tau^- \bar{\nu}_\tau$, $\Lambda_b^0 \to \Lambda_c^{*+} \mu^- \bar{\nu}_\mu$ and $\Lambda_b^0 \to \Lambda_c^* D_s$ the implemented templates

correspond to Monte Carlo sample distributions.
The fake Λ_c^* events templates, instead, as described in subsection 6.3.1, have been taken by the shape of MLPBNN in the Δm range $[360, 380]$ MeV/c^2, weighted event by event using a function which consider the variations in shape for the MLPBNN distribution evaluated in a lower and higher Δm interval with respect to signal region ($\Delta m \in [336.45, 346.45]$ MeV/c^2, described in section 6.4), containing pure background events.
Finally the template of the wrong sign component, as explained in 6.3.2 has been taken by a one-dimensional kernel estimation p.d.f applied to distribution of muon misidentified events, whose description is in subsection 5.4.2 .

6.3.1 Fake Λ_c^* Events Templates

As shown in section 5.4, a fit to the data sample, defined from final states formed of $\Lambda_c^{*+}\mu^-$ reconstructed tracks which passes all steps of the selection, allow to identify the fake Λ_c^* events distributions.
From figure 5.6, displaying the Δm fit in the range $\Delta m \in [280, 380]$ MeV/c^2, it is possible to select a region containing only combinatorial fake Λ_c^* events where $\Delta m > 350$ MeV/c^2. Another region can be found in the range $\Delta m \in [325.5, 332.5]$ MeV/c^2, between the peaks of $\Lambda_c^+(2595)$ and $\Lambda_c^+(2625)$ events. Then, the shapes of each one variable input of vertexes Fisher and of neutral network about the combinatorial fake Λ_c^* component can be identify using these events, expecting that, the distributions under the $\Lambda_c^+(2625)$ signal peak don't change as a function of Δm . In particular, due to the proximity of the peaks, is more safe to select as combinatorial fake Λ_c^* region, that one around $\Delta m \in [360, 380]$ MeV/c^2. However, to take into account some potential difference in shapes for this type of events under the signal peak, a correction is applied. It is calculated as the ratio of MLPBNN distributions in the range of $\Delta m \in [325.5, 332.5]$ MeV/c^2 and of $\Delta m \in [350, 360]$ MeV/c^2 both normalized to $\Delta m \in [260, 280]$ MeV/c^2. The plots obtained are then fitted using a third order Chebyshev polynomials of first kind, which is used to weight event by event the MLPBNN combinatorial fake Λ_c^* distributions.

This technique is applied for each isolation and q^2 bin and the results are

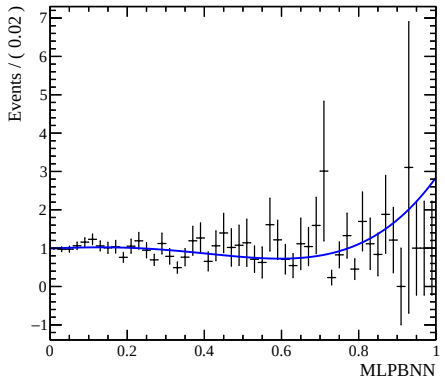

(a) $q^2 \in (-10, 1)(GeV/c)^2$

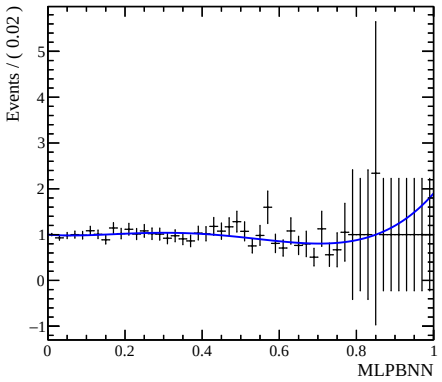

(b) $q^2 \in (1, 3)(GeV/c)^2$

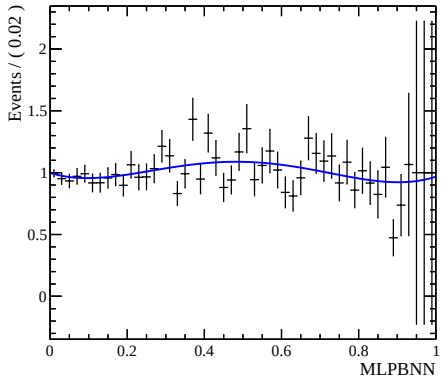

(c) $q^2 \in (3, 5)(GeV/c)^2$

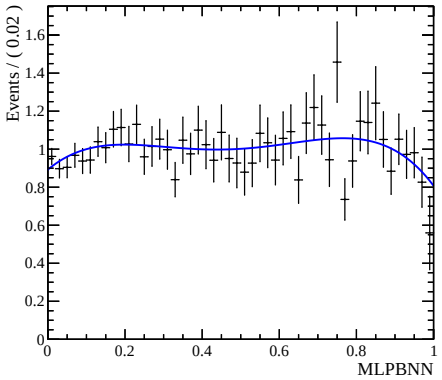

(d) $q^2 \in (5, 7)(GeV/c)^2$

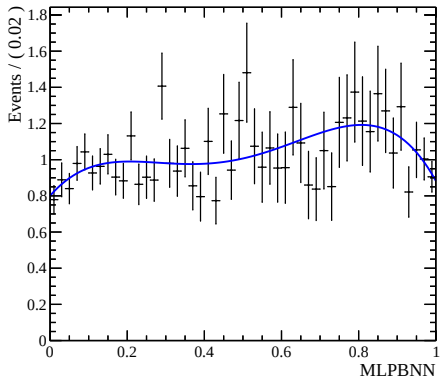

(e) $q^2 \in (7, 10)(GeV/c)^2$

Figure 6.1: Fit to the ratio of MLPBNN distributions in the range of $\Delta m \in [325.5, 332.5]$ MeV/c^2 and of $\Delta m \in [350., 360]$ MeV/c^2 both normalized to $\Delta m \in [360, 380]$ MeV/c^2- $ISO < 0.25$

shown in figure 6.1 and 6.2, respectively for bin $ISO < 0.25$ and $ISO \geq 0.25$.

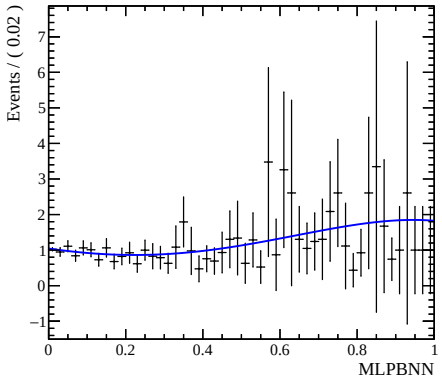

(a) $q^2 \in (-10, 1)(GeV/c)^2$

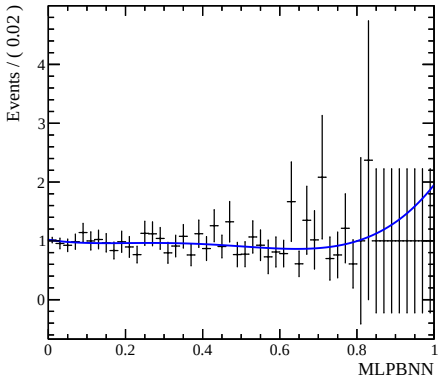

(b) $q^2 \in (1, 3)(GeV/c)^2$

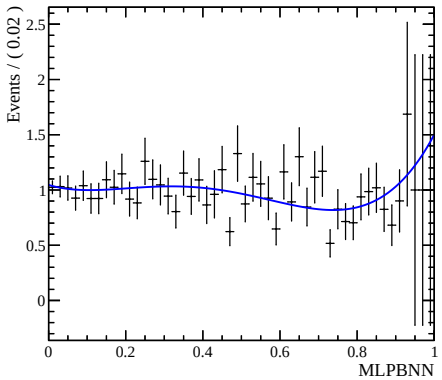

(c) $q^2 \in (3, 5)(GeV/c)^2$

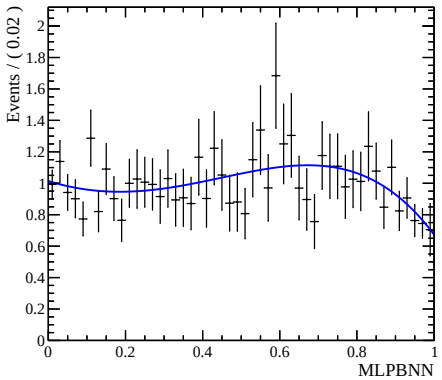

(d) $q^2 \in (5, 7)(GeV/c)^2$

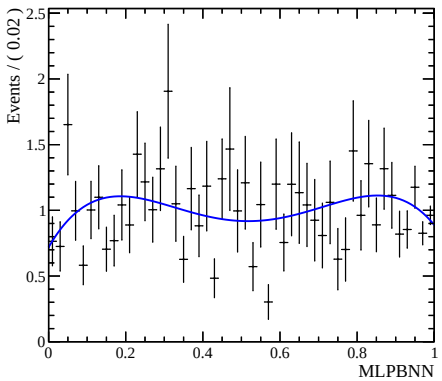

(e) $q^2 \in (7, 10)(GeV/c)^2$

Figure 6.2: Fit to the ratio of MLPBNN distributions in the range of $\Delta m \in [325.5, 332.5]$ MeV/c^2 and of $\Delta m \in [350., 360]$ MeV/c^2 both normalized to $\Delta m \in [360, 380]$ MeV/c^2 - $ISO \geq 0.25$

6.3.2 Wrong Sign Component Templates

Thanks to this fit to the wrong sign component we can know the number of events formed of a true Λ_c^* track composed with a wrong charge muon which can not be signal-like but only events with a muon misidentified. Since the topology of these decays and the selection applied are the same to that searched for our signal candidate ($\Lambda_c^{*+}\mu^-$ final state), we can assume that the muon misidentification component of background in $\Lambda_c^{*+}\mu^-$ final state data is equal to the number of events and has the same the kinematic distributions of the wrong sign sample. The number of these events in each q^2 and isolation bins is not enough to form a template which is not affected by statistical fluctuations, therefore a one-dimensional kernel estimation p.d.f [55] is performed, using the *RooKeysPdf* ROOT class.
The technique allows to model the distribution of an arbitrary input dataset as a superposition of Gaussian kernels, one for each data point, each contributing 1/N to the total integral of the p.d.f. The final distribution is then a continuous estimations of parental distribution.
Figure 6.3 shows, on the left column the histograms of wrong sign events and, on the right the smoothed correspondent distribution for bin $ISO < 0.25$ and for each q^2 bins except the first one. In fact, in this case all events are concentrated to very low MLPBNN event and a smoothed distribution would provide a distorted shape. The same effect is present for the distribution of MLPBNN concerning for the $ISO \geq 0.25$ bin. Figure 6.4 shows, using with the same structure of figure 6.3, the wrong sign distribution after applying $ISO \geq 0.25$ for the residual q^2 bins.

6.4 Fit to MLPBNN Distributions

An extended maximum likelihood fit is performed simultaneously on MLPBNN variable distribution of LHCb 2012 data, in five bins of transferred momentum ($]-10, 1]$, $]1, 3]$, $]3, 5]$, $]5, 7]$, $]7, 10]$ (GeV/c)^2) and in two isolation bins ($ISO \geq 0.25$ and $ISO < 0.25$). It is performed around the $\Lambda_c^+(2625)$ peak, in the $\Delta m \in [336.45, 346.45]$ MeV/c^2 range. In order to find the most

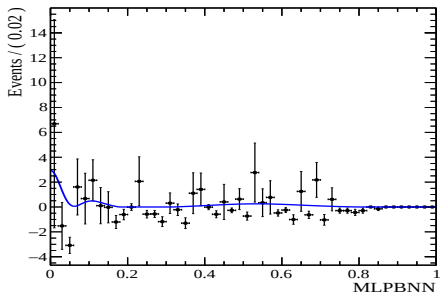

(a) $q^2 \in (1,3)(GeV/c)^2$

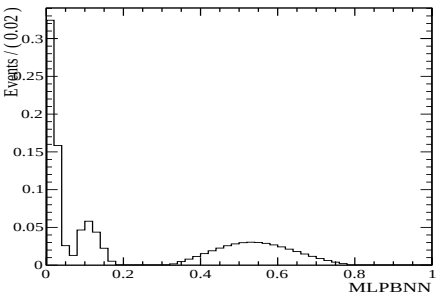

(b) $q^2 \in (1,3)(GeV/c)^2$ - RooKeysPdf

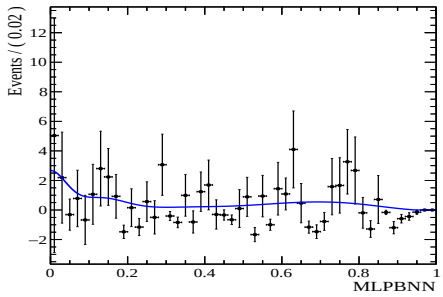

(c) $q^2 \in (3,5)(GeV/c)^2$

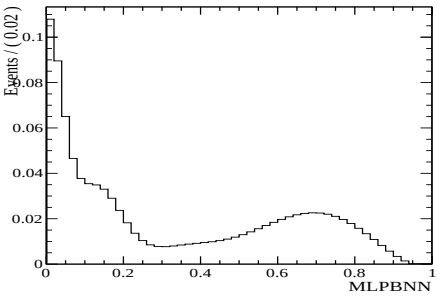

(d) $q^2 \in (3,5)(GeV/c)^2$- RooKeysPdf

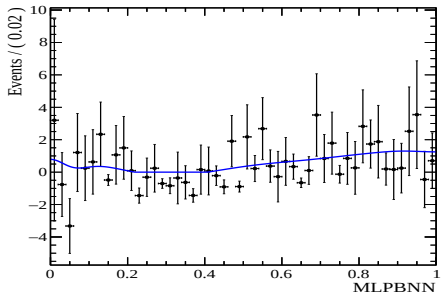

(e) $q^2 \in (5,7)(GeV/c)^2$

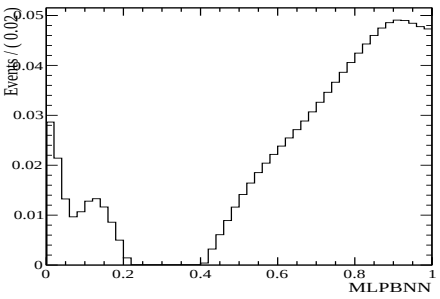

(f) $q^2 \in (5,7)(GeV/c)^2$- RooKeysPdf

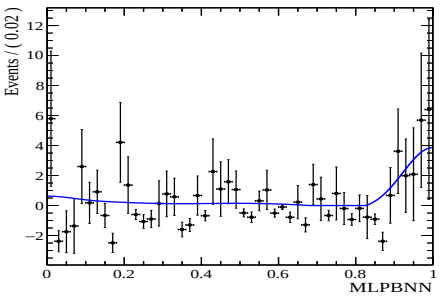

(g) $q^2 \in (7,10)$ $|(GeV/c)^2$

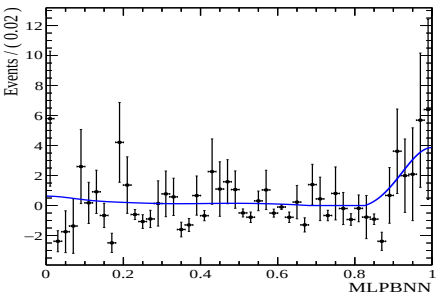

(h) $q^2 \in (7,10)$ $(GeV/c)^2$- RooKeysPdf

Figure 6.3: MLPBNN distributions (left) and smoothed correspondent distributions (right) of the wrong sign sample, after applying the $ISO < 0.25$ cut.

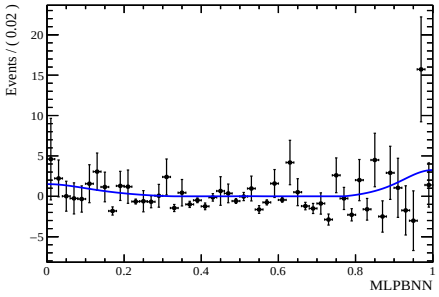

(a) $q^2 \in (-10, 1)(GeV/c)^2$

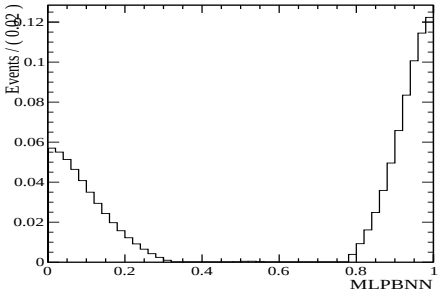

(b) $q^2 \in (-10, 1)(GeV/c)^2$-RooKeysPdf

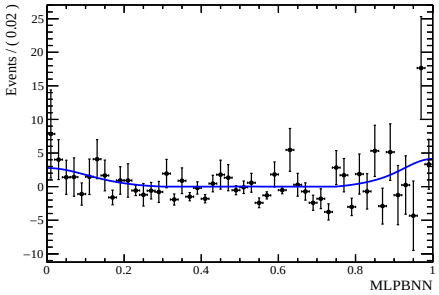

(c) $q^2 \in (3, 5)(GeV/c)^2$

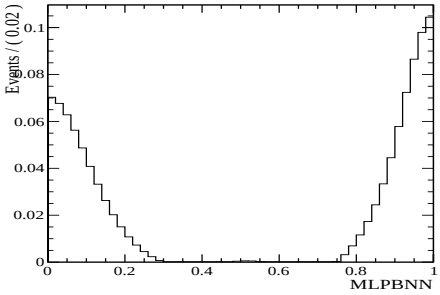

(d) $q^2 \in (3, 5)(GeV/c)^2$- RooKeysPdf

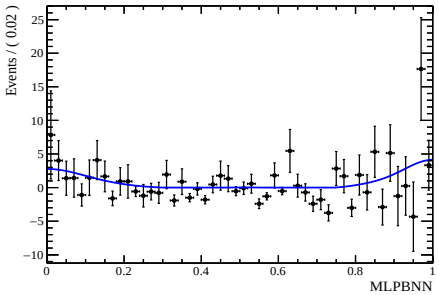

(e) $q^2 \in (5, 7)(GeV/c)^2$

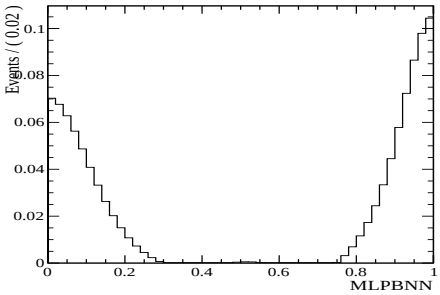

(f) $q^2 \in (5, 7)(GeV/c)^2$- RooKeysPdf

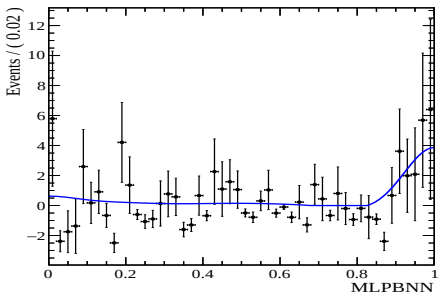

(g) $q^2 \in (7, 10)(GeV/c)^2$

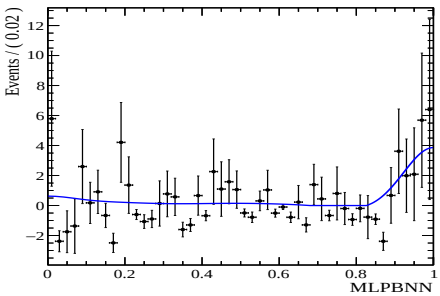

(h) $q^2 \in (7, 10)(GeV/c)^2$-RooKeysPdf

Figure 6.4: MLPBNN distributions (left) and smoothed correspondent distributions (right) of the wrong sign sample, after applying the $ISO \geq 0.25$ cut.

efficient signal region we looked for the Δm cut for which was maximized the ratio given by number of $\Lambda_c^+(2625)$ events with respect to the square root of themselves added to those one of background resulting in the Δm fit of data (not binned).

The fit is based on the templates of the components and it is implemented using the *HistFactory* tool. The $\Lambda_b^0 \to \Lambda_c^* \tau^- \bar{\nu}_\tau$, $\Lambda_b^0 \to \Lambda_c^{*+} \mu^- \bar{\nu}_\mu$ and double charmed components correspond to the MC distributions, shown in section 5.6, and contain the events number listed in table 6.1 and 6.2 for the two isolation bins. The templates put in the fit to determine the fake Λ_c^* and the wrong sign components are instead described in the sections 6.3.1 and 6.3.2 respectively and the events number is reported in tables 6.3 and 6.4. The wrong sign events number keeps into account the efficiency of the Δm cut on the signal region, which is about the 90 %. The last two components, obtained from LHCb data, are fixed in the fit.

$q^2 \in]-10,1]$ $(GeV/c)^2$	
Nevents	Value
N_μ	165±10
N_τ	7±2
N_{D_S}	34±5

$q^2 \in]1,3]$ $(GeV/c)^2$	
Nevents	Value
N_μ	365±16
N_τ	6±2
N_{D_S}	114±9

$q^2 \in]3,5]$ $(GeV/c)^2$	
Nevents	Value
N_μ	331±15
N_τ	50±6
N_{D_S}	466±18

$q^2 \in]5,7]$ $(GeV/c)^2$	
Nevents	Value
N_μ	218±12
N_τ	117±9
N_{D_S}	248±13

$q^2 \in]7,10]$ $(GeV/c)^2$	
Nevents	Value
N_μ	84±7
N_τ	75±7
N_{D_S}	66±6

Table 6.1: MC events in the simulated templates - $ISO \geq 0.25$.

The isolation cut allows to select a sample depleted of semitauonic with respect to double charmed decays. The transferred momentum division permits, instead, to have a greater discriminant power between the MLPBNN distribution of the semitauonic and double charmed Λ_c^* decays and also to reduce the dependence of semimuonic form factors which have never been

$q^2 \in]-10,1]$ $(GeV/c)^2$	
Nevents	Value
N_μ	2169±39
N_τ	39±5
N_{D_S}	150±10

$q^2 \in]1,3]$ $(GeV/c)^2$	
Nevents	Value
N_μ	4528±56
N_τ	101±8
N_{D_S}	346±15

$q^2 \in]3,5]$ $(GeV/c)^2$	
Nevents	Value
N_μ	4655±57
N_τ	730±23
N_{D_S}	1404±31

$q^2 \in]5,7]$ $(GeV/c)^2$	
Nevents	Value
N_μ	3201±47
N_τ	1682±34
N_{D_S}	808±24

$q^2 \in]7,10]$ $(GeV/c)^2$	
Nevents	Value
N_μ	1261±30
N_τ	1079±27
N_{D_S}	233±13

Table 6.2: MC events in the simulated templates - $ISO < 0.25$.

q^2 range $(GeV/c)^2$	$N_{\Lambda_c^* fake}(ISO \geq 0.25)$	$N_{\Lambda_c^* fake}(ISO < 0.25)$
$q^2 \in]-10,1]$	3128 ± 106	781 ± 26
$q^2 \in]1,3]$	3444 ± 139	1349 ± 55
$q^2 \in]3,5]$	4619 ± 91	1704 ± 34
$q^2 \in]5,7]$	4523 ± 81	1716 ± 31
$q^2 \in]7,10]$	2537 ± 29	1099 ± 14

Table 6.3: Number of Λ_c^* fake events in each isolation bins.

q^2 range $(GeV/c)^2$	$N_{WS}(ISO \geq 0.25)$	$N_{WS}(ISO < 0.25)$
$q^2 \in]-10,1]$	38 ± 12	54 ± 15
$q^2 \in]1,3]$	14 ± 9	7 ± 10
$q^2 \in]3,5]$	41 ± 12	22 ± 12
$q^2 \in]5,7]$	23 ± 14	23 ± 16
$q^2 \in]7,10]$	34 ± 16	21 ± 16

Table 6.4: Number of wrong sign events in each isolation bins.

measured. Also for the semitauonic form factor only a theoretical estimation exists but the contribution to the overall distribution of these decays is very low with respect to semimuonic one. In particular, the fractions of double charmed and semitauonic decays in each isolation bins have been fixed in the fit according to the MC samples and are listed in table 6.5. In the fit are also fixed the fractions of semitauonic and double charmed decays with respect to overall number of themselves, in each q^2 bin in the two ISO bins. The values are reported in table 6.6.

	$ISO \geq 0.25$	$ISO < 0.25$
$\Lambda_b^0 \to \Lambda_c^* \tau^- \bar{\nu}_\tau$	0.07	0.93
$\Lambda_b \to \Lambda_c^* D_s$	0.24	0.76

Table 6.5: Fractions of MC semitauonic and double charmed events in each isolation bins.

$\Lambda_b^0 \to \Lambda_c^* \tau^- \bar{\nu}_\tau$	
$ISO \geq 0.25$	
q^2 range $(GeV/c)^2$	g
$q^2 \in]-10, 1]$	0.027
$q^2 \in]1, 3]$	0.023
$q^2 \in]3, 5]$	0.196
$q^2 \in]5, 7]$	0.459
$q^2 \in]7, 10]$	0.294

$\Lambda_b^0 \to \Lambda_c^* \tau^- \bar{\nu}_\tau$	
$ISO < 0.25$	
q^2 range $(GeV/c)^2$	g
$q^2 \in]-10, 1]$	0.0105
$q^2 \in]1, 3]$	0.028
$q^2 \in]3, 5]$	0.201
$q^2 \in]5, 7]$	0.463
$q^2 \in]7, 10]$	0.297

$\Lambda_b \to \Lambda_c^* D_s^{(*)}$	
$ISO \geq 0.25$	
q^2 range $(GeV/c)^2$	g
$q^2 \in]-10, 1]$	0.031
$q^2 \in]1, 3]$	0.124
$q^2 \in]3, 5]$	0.504
$q^2 \in]5, 7]$	0.268
$q^2 \in]7, 10]$	0.067

$\Lambda_b \to \Lambda_c^* D_s^{(*)}$	
$ISO < 0.25$	
q^2 range $(GeV/c)^2$	g
$q^2 \in]-10, 1]$	0.051
$q^2 \in]1, 3]$	0.117
$q^2 \in]3, 5]$	0.477
$q^2 \in]5, 7]$	0.275
$q^2 \in]7, 10]$	0.08

Table 6.6: Fraction g of τ, and $D_s^{(*)}$ semileptonic Λ_c^* decays with respect to overall number of themselves, in each q^2 bin in the two ISO bins.

$N_\mu(q^2 \in]-10, 1]\ (GeV/c)^2,\ ISO \geq 0.25)$	480 ± 50
$N_\mu(q^2 \in]1, 3]\ (GeV/c)^2,\ ISO \geq 0.25)$	883 ± 66
$N_\mu(q^2 \in]3, 5]\ (GeV/c)^2,\ ISO \geq 0.25)$	800 ± 71
$N_\mu(q^2 \in]5, 7]\ (GeV/c)^2,\ ISO \geq 0.25)$	549 ± 63
$N_\mu(q^2 \in]7, 10]\ (GeV/c)^2,\ ISO \geq 0.25)$	183± 40
$N_\mu(q^2 \in]-10, 1]\ (GeV/c)^2,\ ISO < 0.25)$	5161 ± 129
$N_\mu(q^2 \in]1, 3]\ (GeV/c)^2,\ ISO < 0.25)$	9179 ± 160
$N_\mu(q^2 \in]3, 5]\ (GeV/c)^2,\ ISO < 0.25)$	8250 ± 173
$N_\mu(q^2 \in]5, 7]\ (GeV/c)^2,\ ISO < 0.25)$	5695 ± 160
$N_\mu(q^2 \in]7, 10]\ (GeV/c)^2,\ ISO < 0.25)$	2048 ± 106
N_τ	489 ± 206
N_{D_S}	1320 ± 226

Table 6.7: Fit to MLPBNN distribution, where N_τ is number of $\Lambda_b^0 \to \Lambda_c^* \tau^- \bar{\nu}_\tau$ decay events fitted, N_μ the number of $\Lambda_b^0 \to \Lambda_c^* \mu^- \bar{\nu}_\mu$ decay events and N_{D_S} the number of double charmed decay events.

Finally, the fit results are listed in table 6.7 and in figures 6.6, 6.5 (logarithmic scale) and 6.7, 6.8, the fit projections in each transferred momentum and isolations bins are presented.

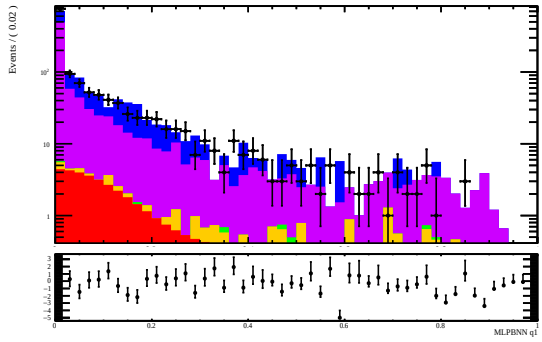

(a) $q^2 \in (-10, 1)(GeV/c)^2$

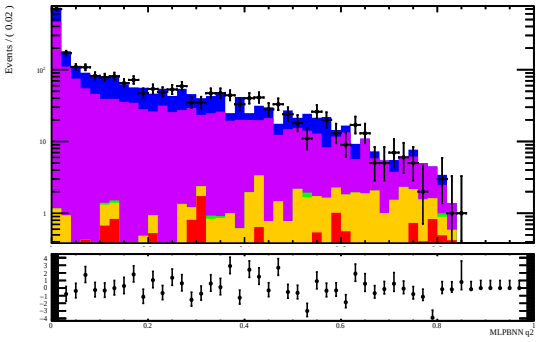

(b) $q^2 \in (1, 3)(GeV/c)^2$

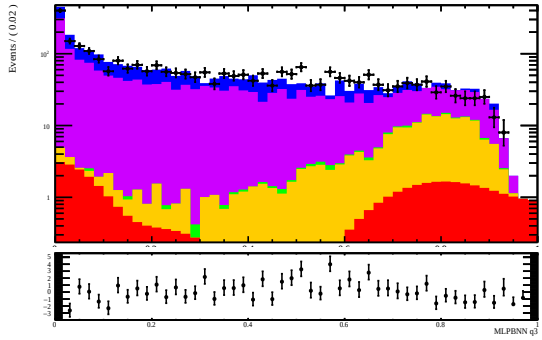

(c) $q^2 \in (3, 5)(GeV/c)^2$

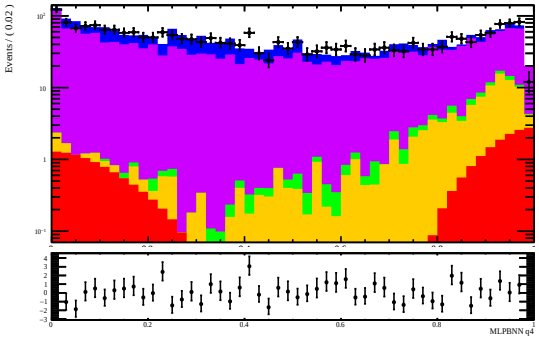

(d) $q^2 \in (5, 7)(GeV/c)^2$

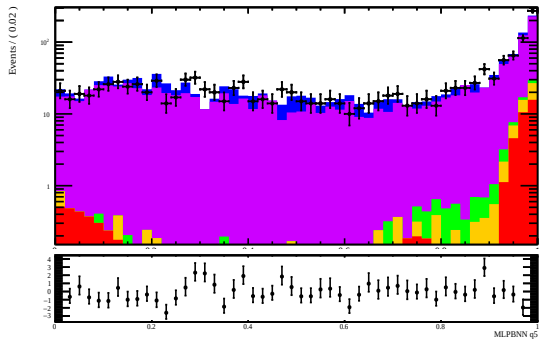

(e) $q^2 \in (7, 10)(GeV/c)^2$

Figure 6.5: MLPBNN fit projection in each transferred momentum after applying the cut $ISO \geq 0.25$, logarithmic scale. Components: LHCb Data (black dots), $\Lambda_b^0 \to \Lambda_c^* \tau^- \bar{\nu}_\tau$(Green), $\Lambda_b^0 \to \Lambda_c^* \mu^- \bar{\nu}_\mu$(Blue), double charmed decays (Orange), Λ_c^* fake events (Purple), Wrong sign component (Red).

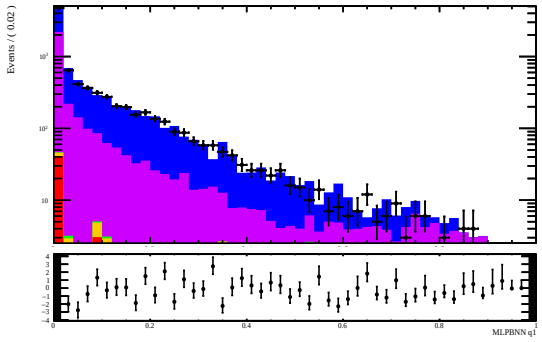

(a) $q^2 \in (-10, 1)(GeV/c)^2$

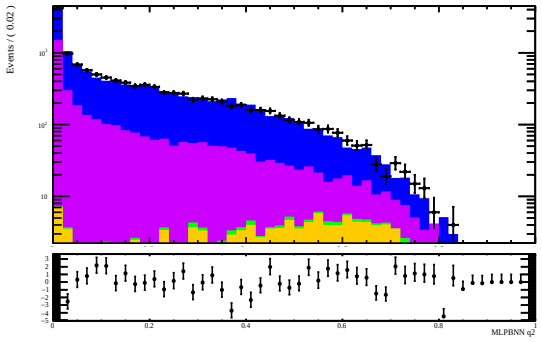

(b) $q^2 \in (1, 3)(GeV/c)^2$

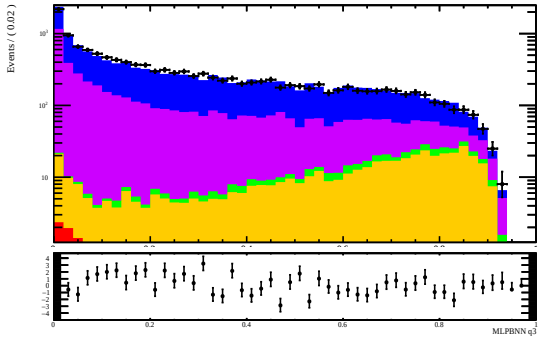

(c) $q^2 \in (3, 5)(GeV/c)^2$

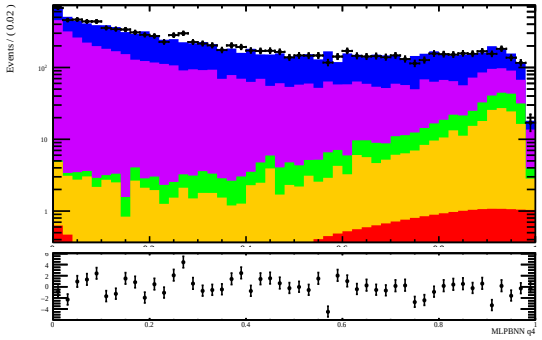

(d) $q^2 \in (5, 7)(GeV/c)^2$

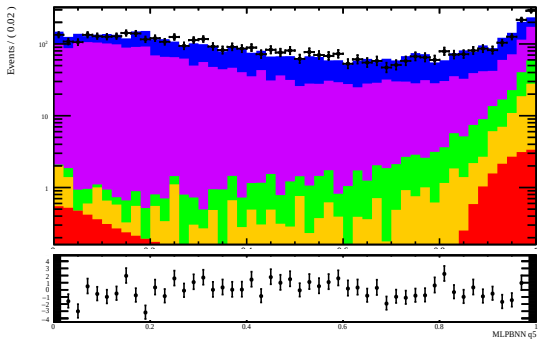

(e) $q^2 \in (7, 10)(GeV/c)^2$

Figure 6.6: MLPBNN fit projection in each transferred momentum after applying the cut $ISO < 0.25$, logarithmic scale. Components: LHCb Data (black dots), $\Lambda_b^0 \to \Lambda_c^* \tau^- \bar{\nu}_\tau$(Green), $\Lambda_b^0 \to \Lambda_c^* \mu^- \bar{\nu}_\mu$(Blue), double charmed decays (Orange), Λ_c^* fake events (Purple), Wrong sign component (Red).

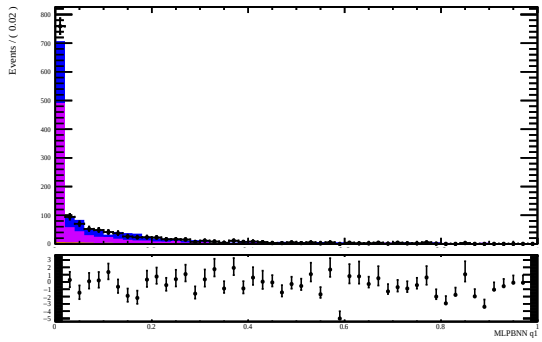

(a) $q^2 \in (-10, 1)(GeV/c)^2$

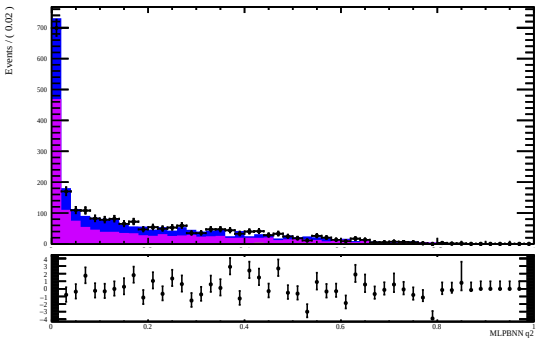

(b) $q^2 \in (1, 3)(GeV/c)^2$

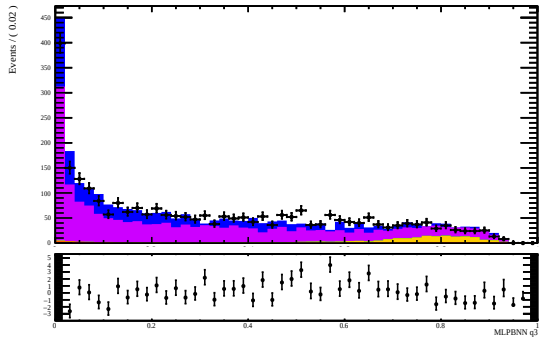

(c) $q^2 \in (3, 5)(GeV/c)^2$

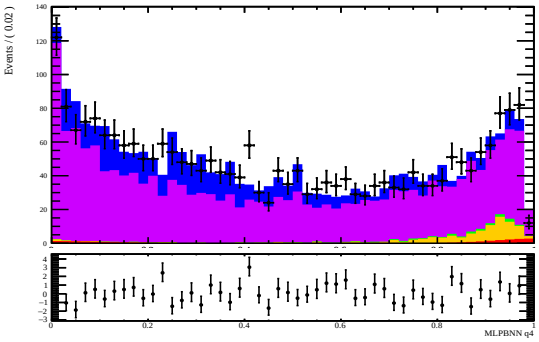

(d) $q^2 \in (5, 7)(GeV/c)^2$

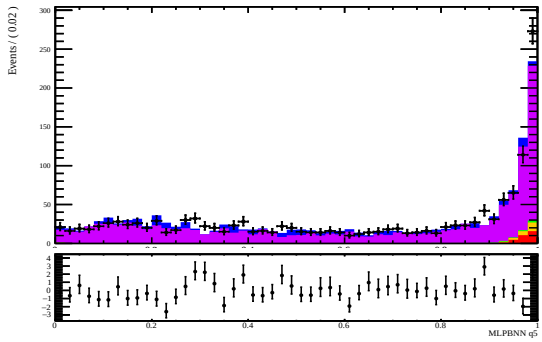

(e) $q^2 \in (7, 10)(GeV/c)^2$

Figure 6.7: MLPBNN fit projection in each transferred momentum after applying the cut $ISO \geq 0.25$. Components: LHCb Data (black dots), $\Lambda_b^0 \to \Lambda_c^* \tau^- \bar{\nu}_\tau$(Green), $\Lambda_b^0 \to \Lambda_c^* \mu^- \bar{\nu}_\mu$(Blue), double charmed decays (Orange), Λ_c^* fake events (Purple), Wrong sign component (Red).

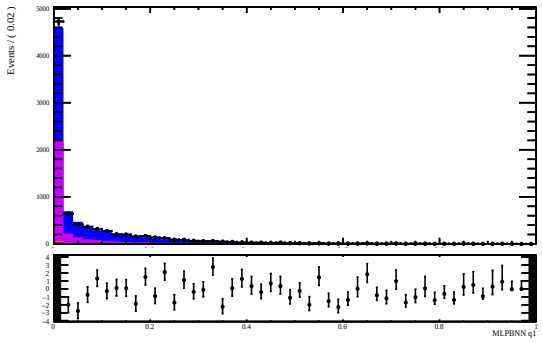

(a) $q^2 \in (-10, 1)(GeV/c)^2$

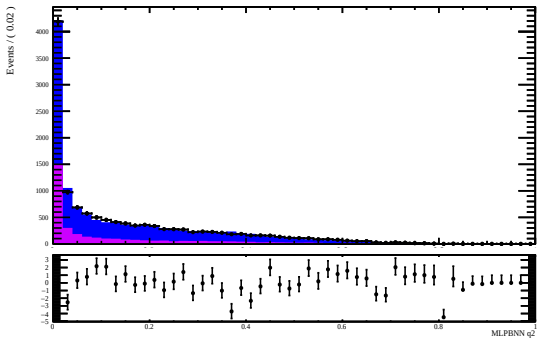

(b) $q^2 \in (1, 3)(GeV/c)^2$

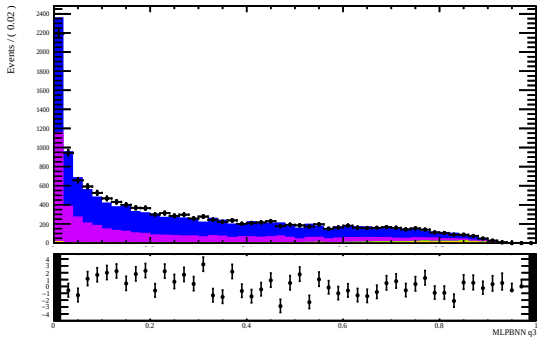

(c) $q^2 \in (3, 5)(GeV/c)^2$

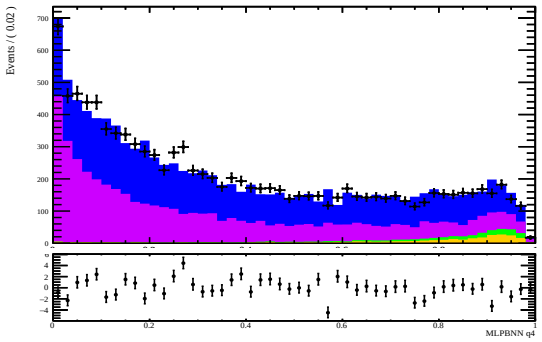

(d) $q^2 \in (5, 7)(GeV/c)^2$

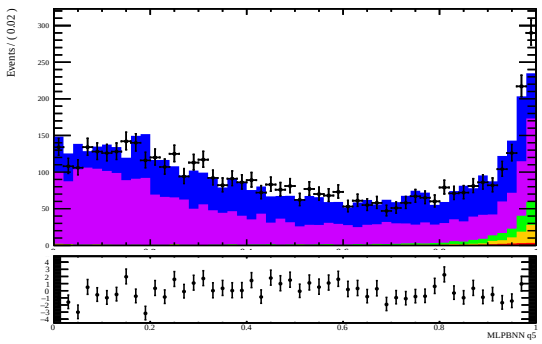

(e) $q^2 \in (7, 10)(GeV/c)^2$

Figure 6.8: MLPBNN fit projection in each transferred momentum after applying the cut $ISO < 0.25$. Components: LHCb Data (black dots), $\Lambda_b^0 \to \Lambda_c^* \tau^- \bar{\nu}_\tau$(Green), $\Lambda_b^0 \to \Lambda_c^* \mu^- \bar{\nu}_\mu$(Blue), double charmed decays (Orange), Λ_c^* fake events (Purple), Wrong sign component (Red).

6.5 Data - Monte Carlo comparisons

In order to check the agreement between the data and the MC samples, the distributions of several variables for each MLPBNN fit component, normalized to the correspondent fitted events number have been stacked and superimposed to the LHCb 2012 data distribution. In particular, the distributions of the missing mass square, of the energy of muon in Λ_b^0 center of mass frame, of the Fisher variable, transferred momentum and finally of transverse momentum of the muon are checked.

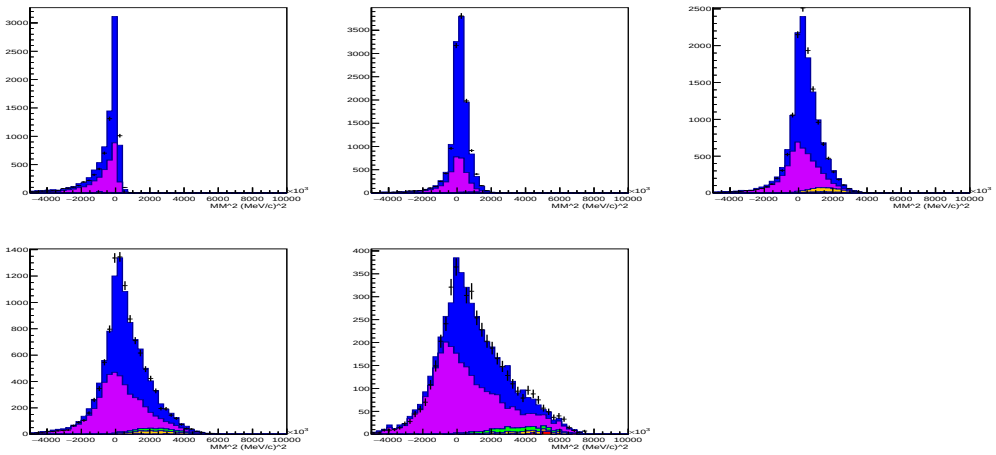

(a)

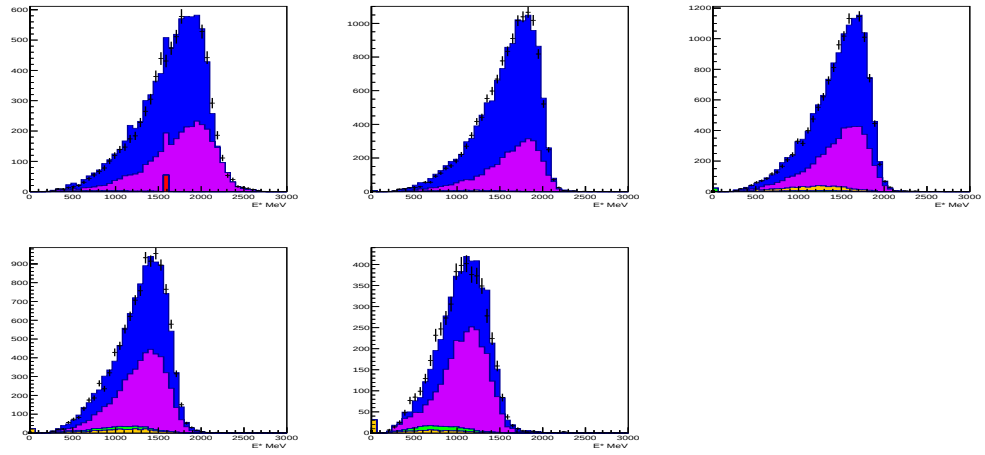

(b)

Figure 6.9: Data-MC comparison of a) MM^2, b) E^*, c) FisherG, d) $p_T(\mu)$ and e) transferred momentum distributions in q^2 bins - $ISO < 0.25$. Components: LHCb Data (black dots), $\Lambda_b^0 \to \Lambda_c^* \tau^- \bar{\nu}_\tau$(Green), $\Lambda_b^0 \to \Lambda_c^* \mu^- \bar{\nu}_\mu$(Blue), double charmed decays (Orange), Λ_c^* fake events (Purple), Wrong sign component (Red).

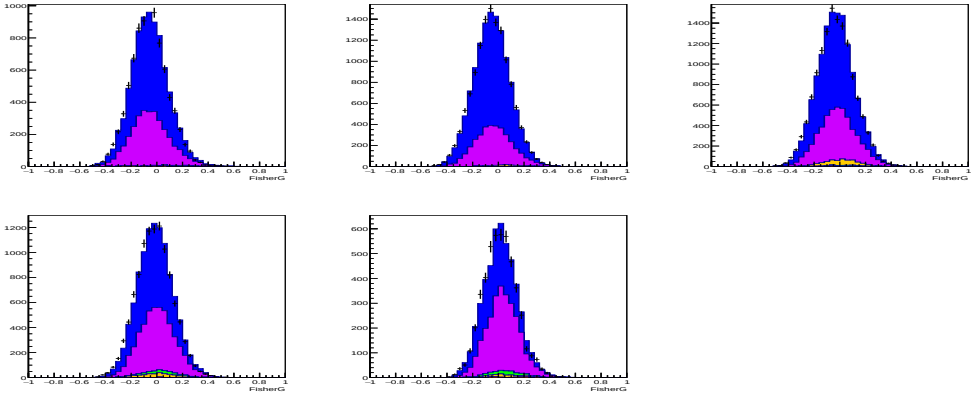

(c)

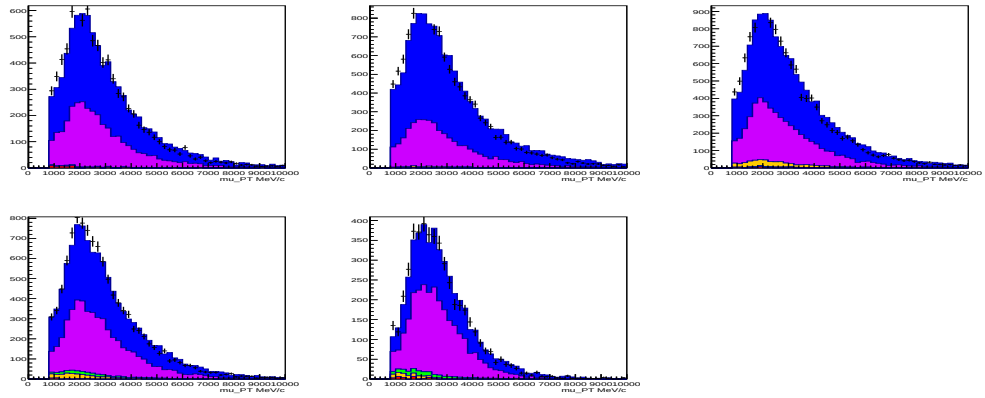

(d)

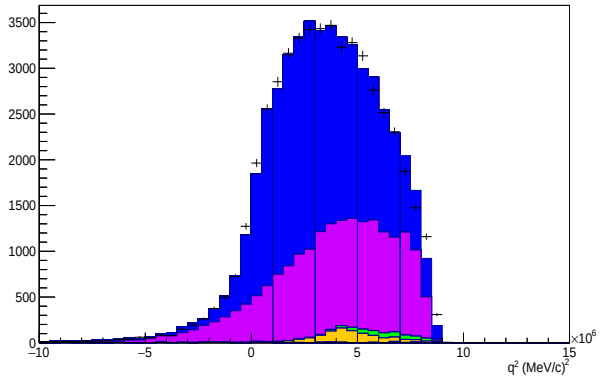

(e)

Figure 6.9: Data-MC comparison of a) MM^2, b) E^*, c) FisherG, d) $p_T(\mu)$ and e) transferred momentum distributions in q^2 bins - $ISO < 0.25$. Components: LHCb Data (black dots), $\Lambda_b^0 \to \Lambda_c^* \tau^- \bar{\nu}_\tau$(Green), $\Lambda_b^0 \to \Lambda_c^* \mu^- \bar{\nu}_\mu$(Blue), double charmed decays (Orange), Λ_c^* fake events (Purple), Wrong sign component (Red).

6.6 Fit Validation

The HistFactory fitter is validated using the the so-called toy Monte Carlo technique (toyMC). A set of pseudo-experiment (also called toys) is generated according to the PDFs used in the fit and with in general the same statistics of the data sample used in the measurement. Each pseudo-experiment is then fitted with the same nominal fit used for the data. This allows to study how sensitive the fit parameters are with respect to statistical fluctuations in the data sample, if tools are performing correctly and if the analysis procedure provides correct error estimates. To evaluate the goodness of fit results, it is usual to calculate, for an ensemble of pseudo datasets, the *"Pull"* related to each parameter, *i.e.* the distribution of the difference between fit (p_{fit}) and generation (p_{gen}) values, normalized to the error on that parameter returned by the fit (σ_{fit}):

$$p_{Pull} = \frac{p_{fit} - p_{gen}}{\sigma_{fit}} \tag{6.4}$$

To minimize the statistical fluctuations affecting fit results, it is usual to perfom hundreds of ToyMC. The relative uncertainty on the average fit parameters is proportional to $\frac{1}{\sqrt{N}}$, where N is the number of toys generated and fitted.

The distribution of the pulls for a given parameter provides the information concerning the reliability of the estimate of that parameter. The relevant features for a pull distribution are the shape, the mean value and the pull width. For a well behaved parameter estimation, the pull distribution is expected to exhibit a Gaussian distribution. This might not be the case for example if the parameter of interest is expected to take a value close to the limits of the allowed range for that parameter. In this cases the likelihood used is not considered a good estimator for the parameter considered. The mean value is expected to be zero for an unbiased fit. A mean pull value different from zero indicates that the parameter considered is systematically overestimated or underestimated. Finally, for a correct uncertainty estimation in the fit, the width of the pull distribution is expected to be compatible with 1 and a smaller (larger) value for the width indicates that the error on

the parameter is systematically overestimated (underestimated).
A thousand of toys have been performed in order to validate the MLPBNN fit and the distribution of the mean value, the error and of the pull for each fit parameter are shown in figure **??**. The number of semitauonic, double charmed or semimuonic Λ_b^0 decays, respectively N_τ, N_{D_s} and N_μ(in the isolation bin ISO $<$0.25 or ISO$\geq$ 0.25) used to generate each toy have been extracted from a Poissionian distribution around the correspondent nominal fit result. The number of fitted semitauonic Λ_b^0 decays, N_τ results slightly biased and the Pulls standard deviations of all parameters assume the values around 0.7.

The exercise is repeated for N_τ equal to zero, the twice and the triple of the number of nominal fit result. Each one of these toys is further repeated for half and twice of N_{D_s} nominal fitted events. Form Figure 6.11, that shows the N_τ mean value resulting from toys as a function of generated events, it is possible to notice that also increasing the N_τ the bias doesn't increase. However, increasing the number of double charmed pseudo events also N_τ rises, and therefore an amount of N_{D_s} is confused with semitauonic decays. Finally a 500 toys have been performed tripling all fit component, also the Λ_c^* fake and wrong sign events. This exercise simulates the condition of Run II LHCb data taking, which will terminate at the end of 2018 and for which the purpose is to collect at least 5 fb^{-1} of data. The results are shown in Figure 6.12. Therefore, using all Run II statistics and the same selection applied in this thesis it will be possible to observe the semitauonic Λ_b^0 decays with an error of 20%.

The number of fitted semitauonic Λ_b^0 decays, N_τ results biased and the Pulls standard deviations of all parameters assume the values around 0.7 in the most of the toys. We have performed many toys configurations but in all cases the pull errors remain wrong. It happens also when only one component is generated and fitted. For this reason we can conclude that the origin of overestimated error is intrinsic to the fit. We have chosen to preform a conservative errors estimation and we haven't propagated the

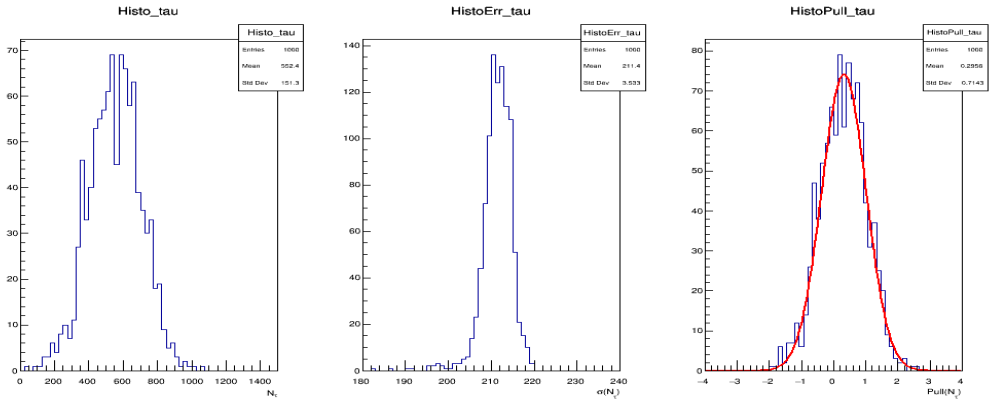

(a)

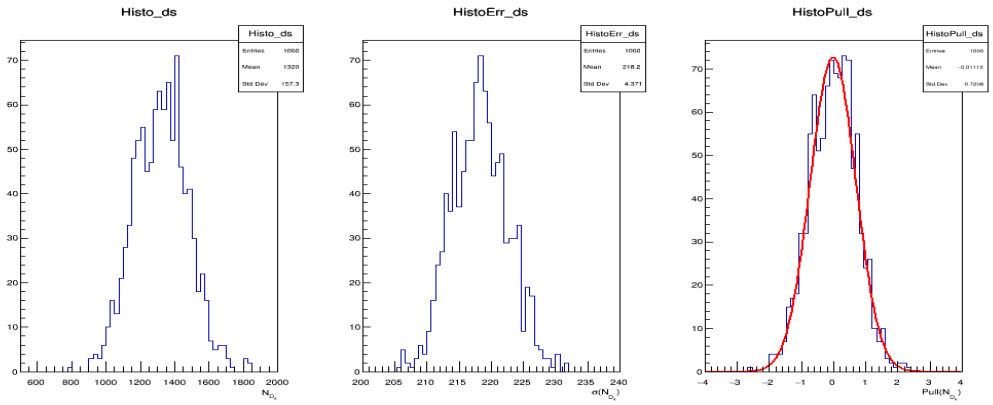

(b)

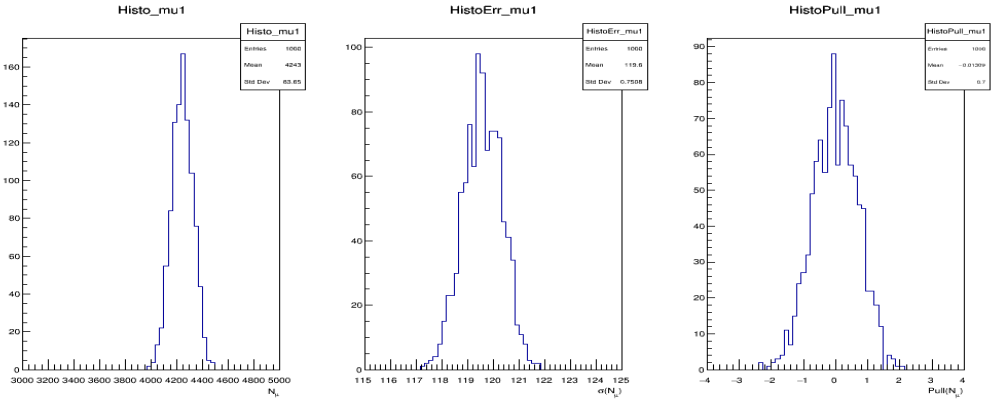

(c)

Figure 6.10: N_τ (a), N_{D_s} (b) and N_μ ((c-g): ISO $<$ 0.25, (h-l): ISO $\geq$ 0.25) mean value, error and pull distributions for toys results generated from Poissonian distribution around the correspondent nominal fit result.

inferred correction to the fit results. Moreover, as you can see in figure 6.10, the mean of the pull about the semitauonic fit component results equal to

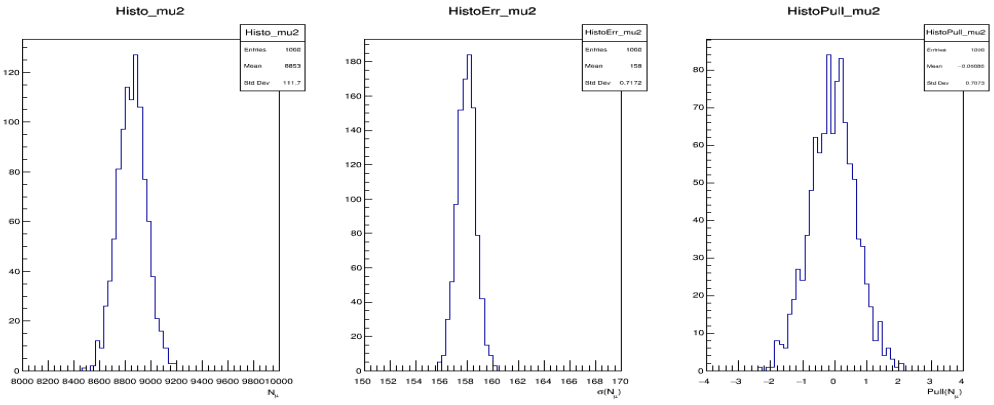

(d)

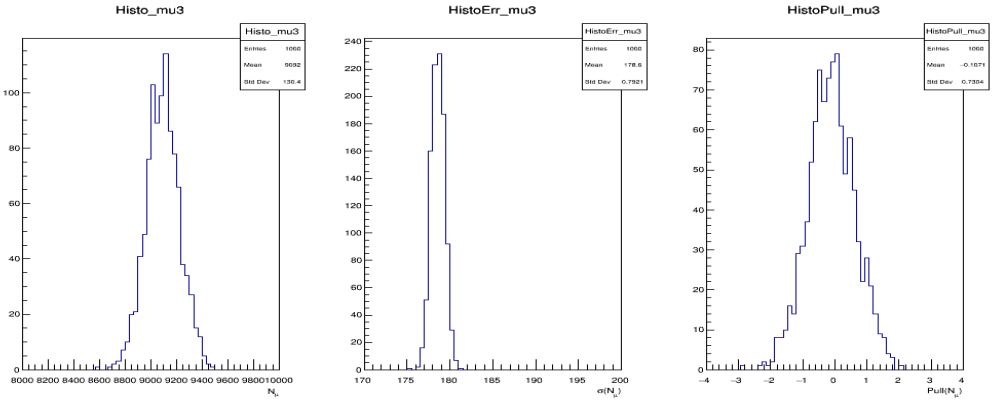

(e)

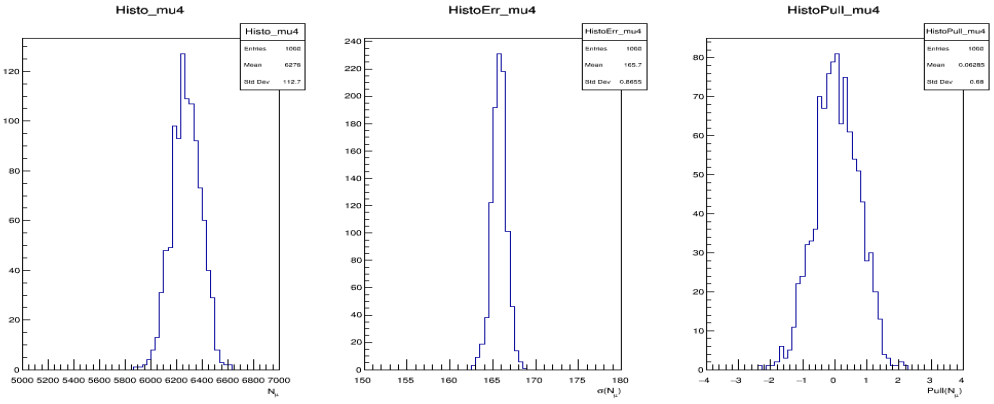

(f)

Figure 6.10: N_τ (a), N_{D_s} (b) and N_μ ((c-g): ISO $<$ 0.25, (h-l): ISO $\geq$ 0.25) mean value, error and pull distributions for toys results generated from Poissonian distribution around the correspondent nominal fit result.

0.29. The figure 6.13 shows the variation of the toys mean of fitted tau decays with respect to generated one as a function of number of double

charmed generated decays. In particular, 500 toys have been performed generating 511 semitauonic events (nominal fit results without statistical

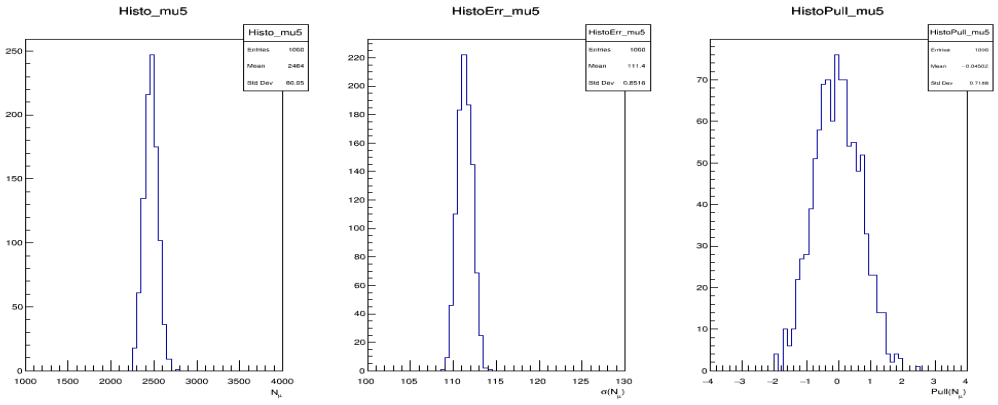

(g)

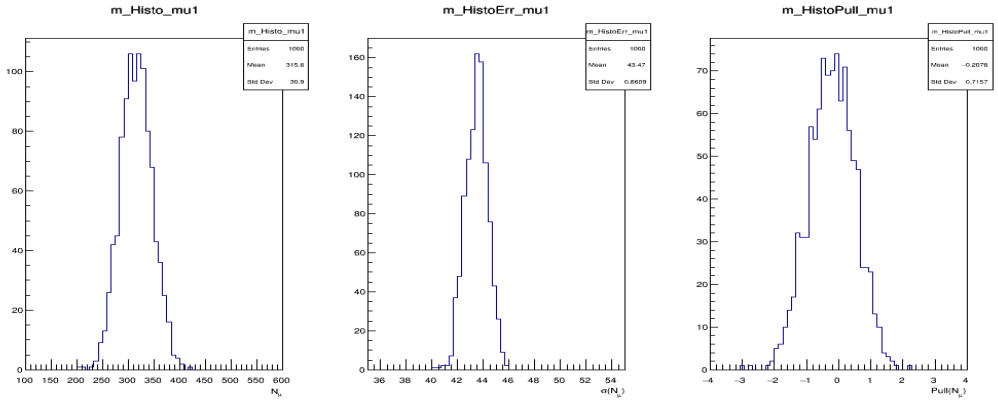

(h)

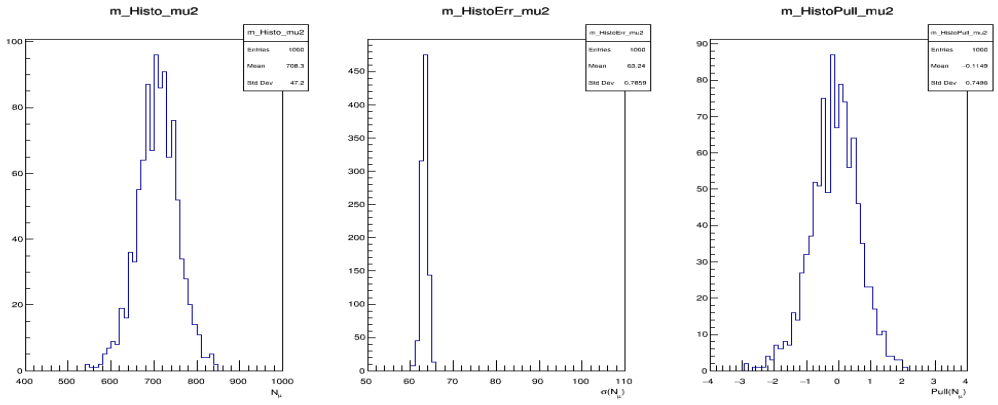

(i)

Figure 6.10: N_τ (a), N_{D_s} (b) and N_μ ((c-g): ISO $<$ 0.25, (h-l): ISO $\geq$ 0.25) mean value, error and pull distributions for toys results generated from Poissonian distribution around the correspondent nominal fit result.

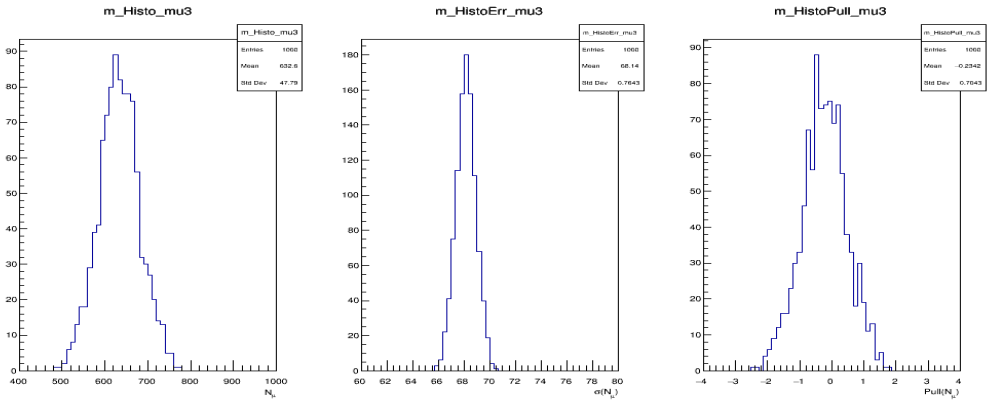

(j)

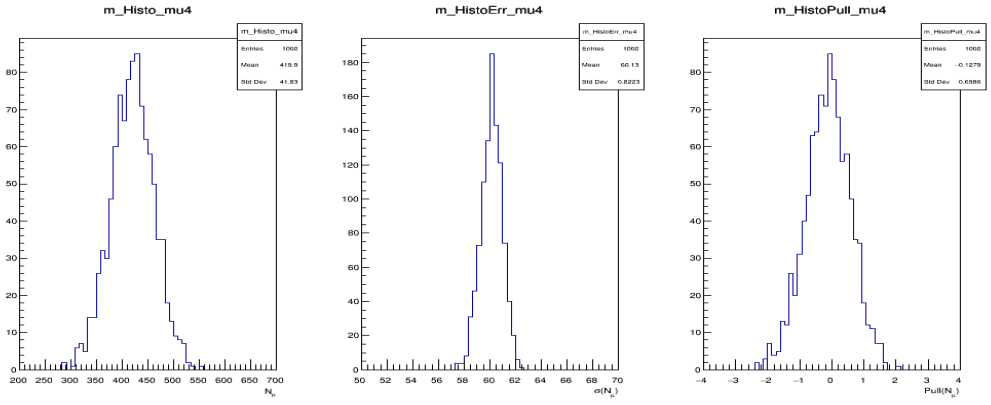

(k)

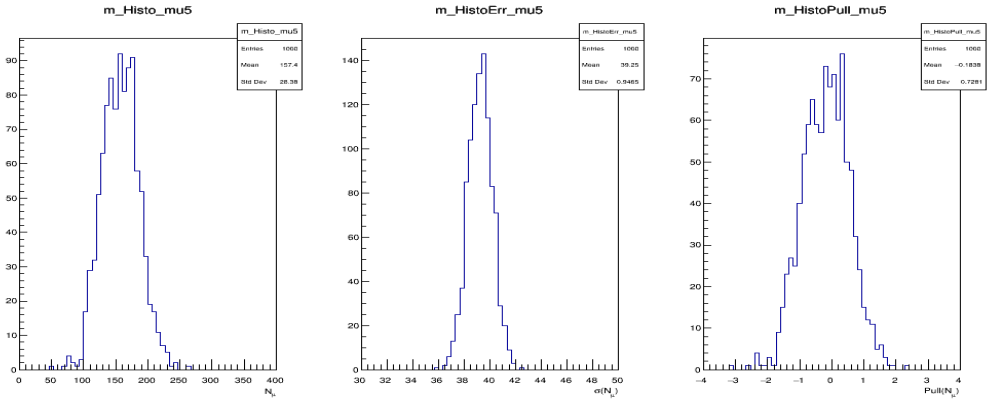

(l)

Figure 6.10: N_τ (a), N_{D_s} (b) and N_μ ((c-g): ISO $<$ 0.25, (h-l): ISO $\geq$ 0.25) mean value, error and pull distributions for toys results generated from Poissonian distribution around the correspondent nominal fit result.

fluctuations) and 0, 612, 1225 (nominal fit without statistical fluctuations) or 2450 double charmed decays. From the interpolation of the points obtained,

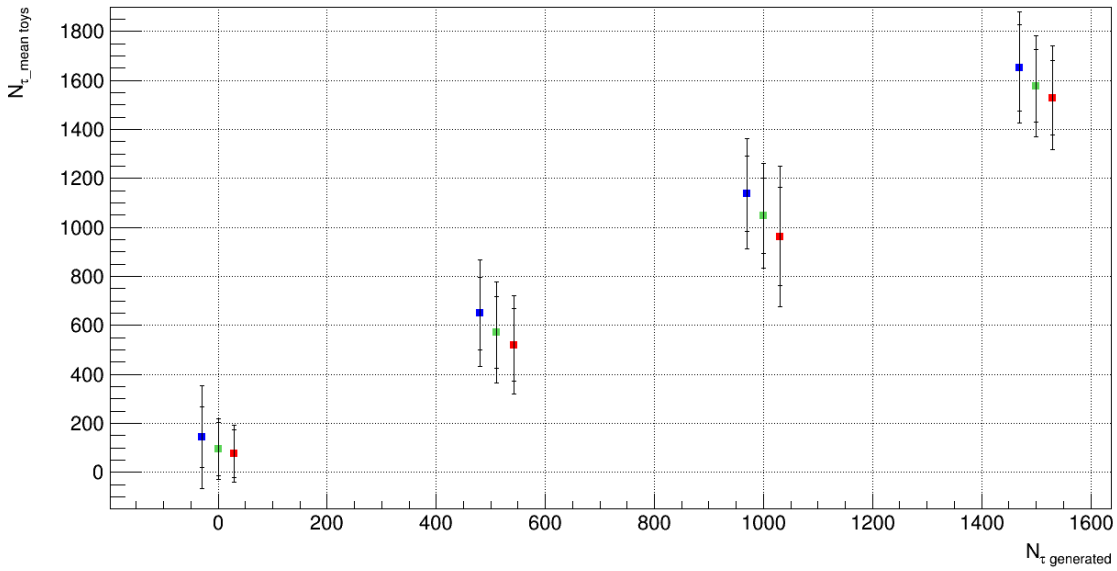

Figure 6.11: Number of fitted semitauonic Λ_b^0 decays as a function of generated one for different amount of generated double charmed events: nominal fitted number (green dots), the half (red dots) and the twice (blue dots).

we can quantify the number of double charmed decays that are exchanged for semitauonic one from the fit. The functional dependence is

$$\Delta\tau = N_{\langle\tau\rangle\ toys} - N_{\tau\ generated} = -25.753 + 0.068 N_{D_s\ generated} \tag{6.5}$$

and substituting the numbers of nominal fit we obtained a correction for the number of semitauonic decays fitted equal to 64. This number is consistent with the bias obtained in our toys. The correction is therefore applied to the fit results.

6.7 Systematic Uncertainties

The MLPBNN fit uses several assumptions and is affected by some limitations. Here the impact of these effects is evaluated, and a corresponding systematic uncertainty is assigned to the measurement $R_{RAW}(\Lambda_c^*) = N(\Lambda_b^0 \to \Lambda_c^{*+}\tau^-\bar{\nu}_\tau)/N(\Lambda_b^0 \to \Lambda_c^{*+}\mu^-\bar{\nu}_\mu)$. The sources of systematic uncertainties are expected to be uncorrelated. For this reason the single contributions are evaluated separately and the overall systematic error on the physics parameters of interest is obtained by means of sum in quadrature of the single

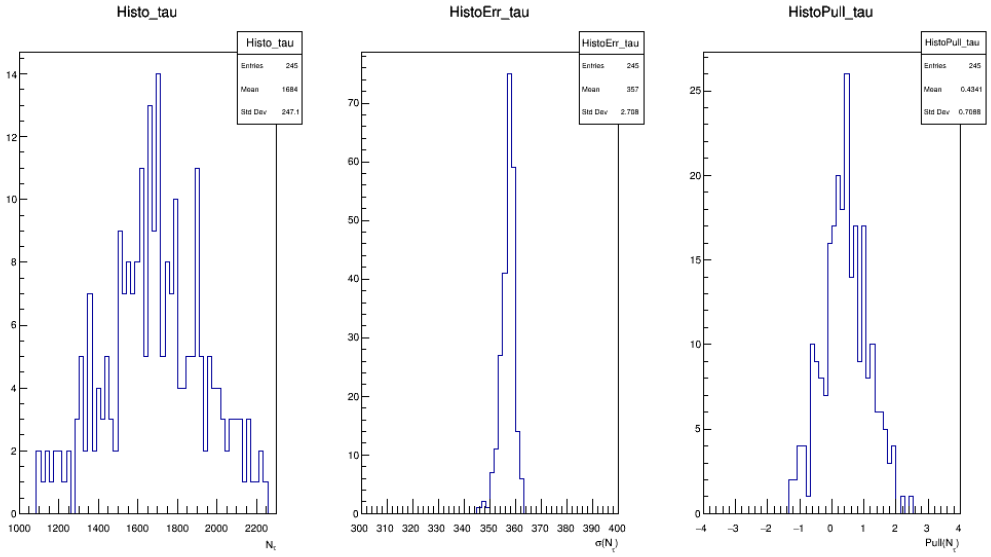

(a)

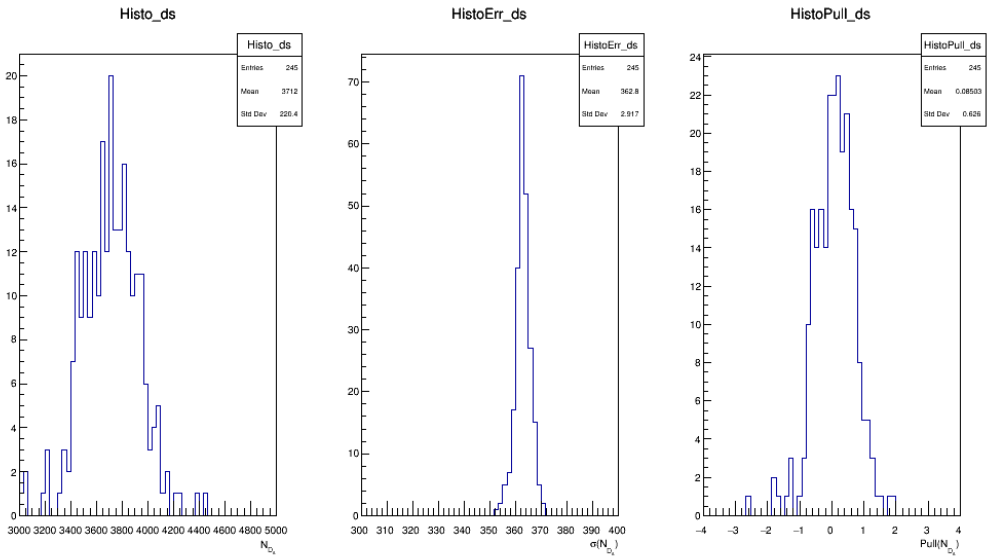

(b)

Figure 6.12: N_τ(a) and N_{D_s}(b) mean value, error and pull distributions for toys results generated from Poissionian distribution tripling (expectation run II data taking) the correspondent nominal fit result .

effects. In the Table 6.8, all systematic uncertainties, singularly described in the next sections, are listed.

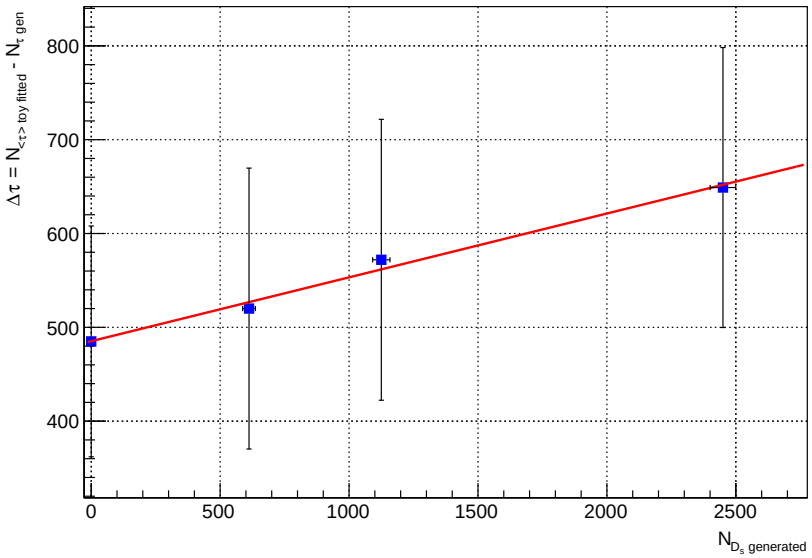

Figure 6.13: Variation of the toys mean of fitted semitauonic decays with respect to generated one as a function of number of double charmed generated decays.

Source of uncertainty	$R_{RAW}(\Lambda_c^*)$ relative uncertainty
MC statistics	0.179
PID corrections	0.046
Λ_c^* fake yields	0.057
Wrong-sign yields	0.064
Wrong-sign shape	0.078
double charmed composition	0.112
nSPD correction	0.021
Form Factor model	0.022
Quadratic sum	0.247

Table 6.8: Systematic uncertainties on $R_{RAW}(\Lambda_c^*)$

6.7.1 Systematic uncertainties due to MC Statistics

In this thesis we account for finite template statistics by use of the the Beeston-Barlow [56] "lite" method for the total fit PDF. To separate out the effect of template statistics in the total fit uncertainty from the statistical uncertainty in the data, we run the fit procedure with and without use of the Beeston-Barlow method. The quadrature difference is separated from the total fit uncertainty as the systematic uncertainty due to finite template statistics. In this way the reported statistical uncertainty refers only to the

statistics of the data and not the simulation.

6.7.2 Systematic uncertainty due to Particle Identification correction

Particle Identification is implemented in the fit templates by weighting each candidate by a PID efficiency as a function of its momentum and pseudo-rapidity. These efficiencies are determined using high-statistics control samples with the PIDCalib package. To determine this systematic contribute to the $R_{RAW}(\Lambda_c^*)$ a fit has been performed using MC template without PID weight.

6.7.3 Systematic uncertainties due to the description of the combinatorial Λ_c^* fake background

In the nominal fit the number of Λ_c^* fake events for each q^2 bin are fixed to the values listed in Table 6.3. To evalutate the systematic uncertainties on the $R_{RAW}(\Lambda_c^*)$ due to Λ_c^* fake background, a fit is performed changing one by one the fixed combinatorial contribution of ± 1 deviation standard. For each q^2, the $R_{RAW}(\Lambda_c^*)$ result which is mainly discrepant respect to nominal value between those one obtained adding or subtracting events for an amount of 1σ, is taken into account. The quadrature sum of the ten more discrepant result corresponds to value quoted in Table 6.8.

6.7.4 Systematic uncertainties due to the description of the wrong sign component

In the nominal fit the WS component is fixed for each q^2 to the values listed in Table 6.4. To evaluate the systematic uncertainties on the $R_{RAW}(\Lambda_c^*)$ due to this choice, a fit is performed changing one by one the fixed WS contribution of ± 1 deviation standard. For each q^2, the $R_{RAW}(\Lambda_c^*)$ results which is mainly discrepant respect to nominal value between those one obtained adding or subtracting events for an amount of 1σ, is taken into account. The quadrature sum of the ten more discrepant result corresponds to value quoted in Table 6.8.
In the nominal fit, the shapes concerning the WS component are derived

from the RooKeys created using the WS MLPBNN distributions for each q^2 bins. The technique allows to model the distribution of an arbitrary input dataset as a superposition of Gaussian kernels, one for each data point, each contributing 1/N to the total integral of the p.d.f. The Gaussian width used to extract nominal shapes is equal to 1.5. To evaluate the systematic uncertainties on the $R_{RAW}(\Lambda_c^*)$ a fit using WS shapes obtained from a superiposed of Gaussian Kernels characterized by a width equal to 2 has been performed. In Table 6.8, the discrepancy with respect to nominal fit is listed.

6.7.5 Systematic uncertainties due to different D_s and D_s^* shapes

As described in the Chapter 4, due to low size of available Monte Carlo sample, the analysis is performed considering only one double charmed Λ_b^0 decays template obtained adding the contribution of the MC($\Lambda_b^0 \to \Lambda_c^* D_s$) and of $\Lambda_b^0 \to \Lambda_c^* D_s^*$. To evaluate the systematic uncertainties on the $R_{RAW}(\Lambda_c^*)$ a fit using only D_s and another using only D_s^* are performed. That one which is resulted more discrepant with respect to nominal fit is quoted as double charmed shape systematical error and it is listed in Table 6.8.

6.7.6 nSPDHits correction

A systematic uncertainty arises from the incorrect description between data and Monte Carlo of nSPD (Scintillator Pad Detector) hits. The total number of hits in the SPD is used to provide a fast estimation of the charged track multiplicity in the event. All MC templates are therefore re-weighted keeping into account the Data-MC ratio for each sample, in each q^2 and isolation bins. The distributions have been fitted using second order polynomials. The discrepancy with respect to nominal fit is listed in Table 6.8.

6.7.7 Systematic uncertainties due to form factors model

The $\Lambda_c \to \Lambda_c^*$ form factors affect the shapes of semitauonic templates. In section 6.8 the unfolded differential decay rate for $\Lambda_b \to \Lambda_c^* \mu \bar{\nu}_\mu$ is extracted.The distribution differs from the model used to generate the signal events, as can be seen in Fig.6.19. The templates are reweighed to properly account for

the observed difference. To see the impact of a shape modification about the semitauonic decays, assuming the same variation that for the semimunic one, we have corrected the semitauonic templates keeping into account the Data-MC ratio for each q^2 bins as a function of q^2. The discrepancy with respect to nominal fit is listed in Table 6.8.

6.7.8 Systematic uncertainties due to trigger

The systematics due to the trigger requirements are evaluated repeating the analysis using different subsets of trigger lines (L0 Level). For the TOS sample the measured R(Λ_c^*) ratio results equal to $R(\Lambda_c^*)_{TOS} = 0.123 \pm 0.106$, while about the TIS trigger configuration we have obtained $R(\Lambda_c^*)_{TIS} = 0.372 \pm 0.227$. The two measurements are consistent within 1σ and are characterized by big statistical errors. Therefore, we have decided to not consider this contribution in the systematical error, since already incorporated in the statistical uncertainty.

6.7.9 Measurement of R(Λ_c^*) ratio

In the previous section the systematic uncertainties have been described as a function of $R_{RAW}(\Lambda_c^*)$. After having discorporated from the statistical uncertainty, the contribute due to the Monte Carlo available statistics, the following raw ratio has been obtained:

$$R_{RAW}(\Lambda_c^*) = 0.0128 \pm 0.0058(stat) \pm 0.0031(syst) \tag{6.6}$$

The ratio $R(\Lambda_c^*)$, can be then calculated as:

$$R(\Lambda_c^*) = R_{RAW}(\Lambda_c^*)\frac{\epsilon_\mu}{\epsilon_\tau}\frac{1}{\mathcal{B}(\tau^- \to \mu^-\bar{\nu}_\mu\nu_\tau)} \tag{6.7}$$

Therefore, it results equal to

$$R(\Lambda_c^*) = 0.238 \pm 0.108(stat) \pm 0.058(syst) \tag{6.8}$$

It is the first measurement of the R($\Lambda_c^+(2625)$) and also the first measurement which evaluates this kind of ratio using the baryons. The result, obtained

using the data collected from LHCb during 2012, is dominated by statistical error. However, as shown with toys studies in section 6.6, assuming to perform the measurement with same selection, triggers and fit technique on the full run II LHCb data (expected at least 5 fb^{-1} of data), the statistical error will be competitive with the systematic one. The result obtained is consistent with the Standard Model expectation, calculated on the basis of Pervin model et al., [21]:

$$R(\Lambda_c(2625)) = 0.151 \pm 0.014 \tag{6.9}$$

This calculation is described in Chapter 1.

6.8 Differential rate $(1/\Gamma)d\Gamma/dq^2(\Lambda_b \to \Lambda_c^*\mu\bar{\nu}_\mu)$

The numbers of $\Lambda_b \to \Lambda_c^*\mu\bar{\nu}_\mu$ extracted in bins of q^2 in the previous section, are used to determine the differential decay width $d\Gamma/dq^2$. In this section the unfolding of the raw spectrum for the q^2 resolution and the selection efficiency are described. The resolution on the q^2 obtained with the boost-approximation that we have used so far, is worst than the possible resolution we get using the two-fold solutions described in Chapter 3. Nevertheless it is enough to obtain an unfolded spectrum in 5 bins of q^2.

In general the unfolding can be viewed simply as the inverse of the folding of a distribution accounting for a finite resolution. Given a distribution of true $q^2_{true,j}$, the smeared distribution of reconstructed $q^2_{reco,i}$ is given by

$$q^2_{reco,i} = \sum_j M_{i,j} q^2_{true,j} \tag{6.10}$$

where the response matrix $M_{i,j}$ parametrizes the resolution effects: it gives the probability that an event in the unsmeared bin j, is reconstructed in the bin i. If we have the reconstructed data $q^2_{reco,i}$, principle we can obtain $q^2_{true,j}$ through a simple inversion of the matrix $M_{i,j}$. Unfortunately this approach in most of the cases does not work because of the statistical fluctuations associated with the determination of $M_{i,j}$, that tends to amplified by the matrix inversion with unsatisfactory results.

There are various *regularization* methods that are used to overcome this problem. One that is widely used is the so called Singular Value Decomposition (SVD) [57]. This algorithm is implemented in ROOT in the class `TSVDUnfold`. The needed input are the migration matrix that connects the true value of q^2_{true} to the reconstructed q^2_{reco}, and the effective rank parameter k, that gives the number of terms in the decomposition that are significant. This parameter has to be tuned according to the problem considered, usually reasonable results are obtained with k closes to half the numbers of bins.

The migration matrix $(M_{i,j})$ is graphically shown in Fig.6.14. for both a fine binning and for the binning actually used to extract the signal yields.

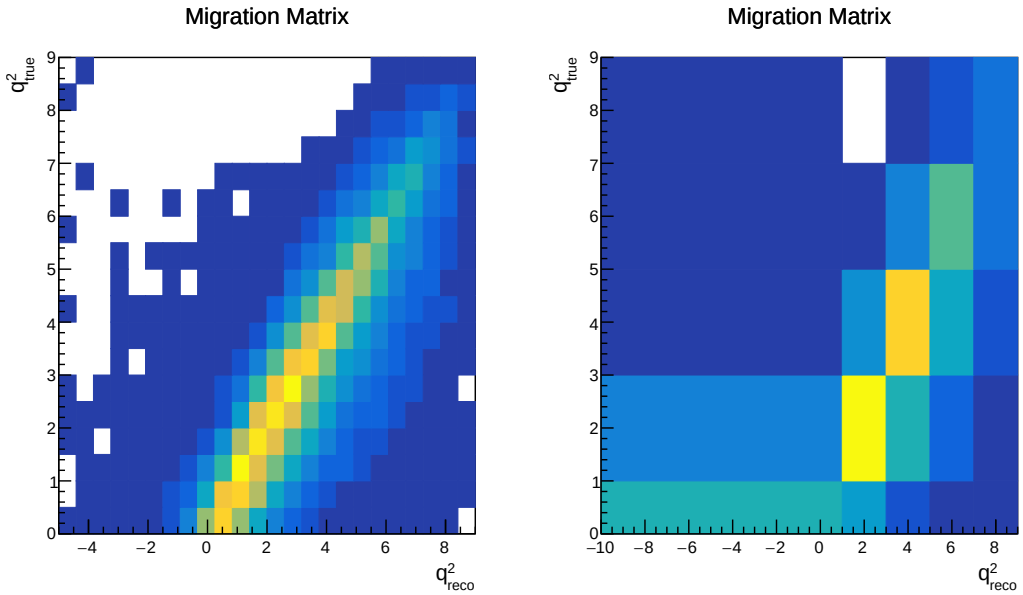

(a)

Figure 6.14: The migration matrix with a fine binning (left) and with the actual binning used in the analysis.

The tuning of k has been done with Monte Carlo. We divided the MC in two equal size samples, one used to extract $M_{i,j}$, and the other to perform the unfolding applying SVD. The value of k that allows to reproduce the true distribution is found to be $k = 2$. In Fig.6.15 and 6.16 we show, as an example, the results on the MC for $k = 2$ and 3. The ratio between the unfolded distribution and the expected one clearly shows a reduced bias in the $k = 2$ case. The residual bias will be added in the systematics for the

spectrum measurement.

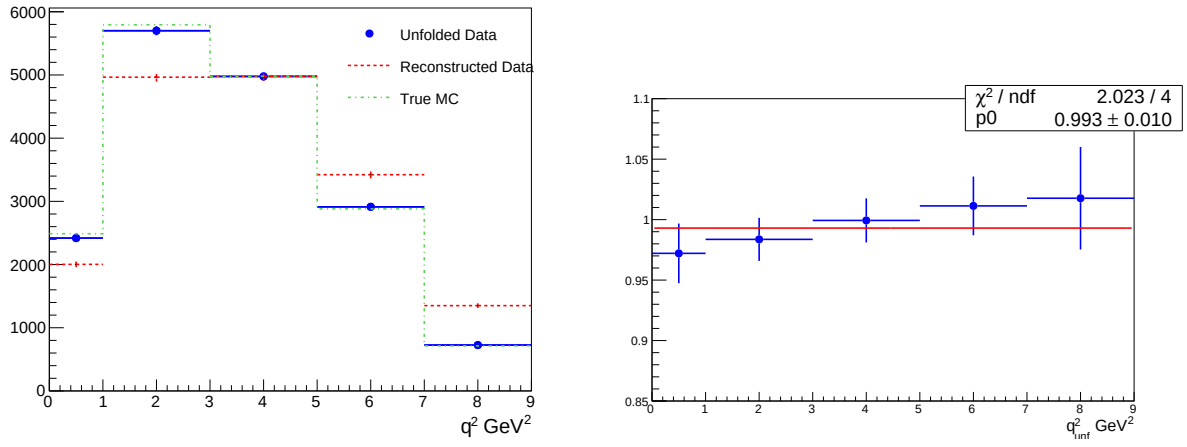

(a) (b)

Figure 6.15: The q^2 spectrum for MC $\Lambda_c^*\mu\bar{\nu}_\mu$: (red) distribution of the reconstructed q^2, (green) distribution of the true q^2, (black dots) unfolded distribution. Here $k = 2$ is considered. The ratio between unfolded and true spectrum, is reported on the right.

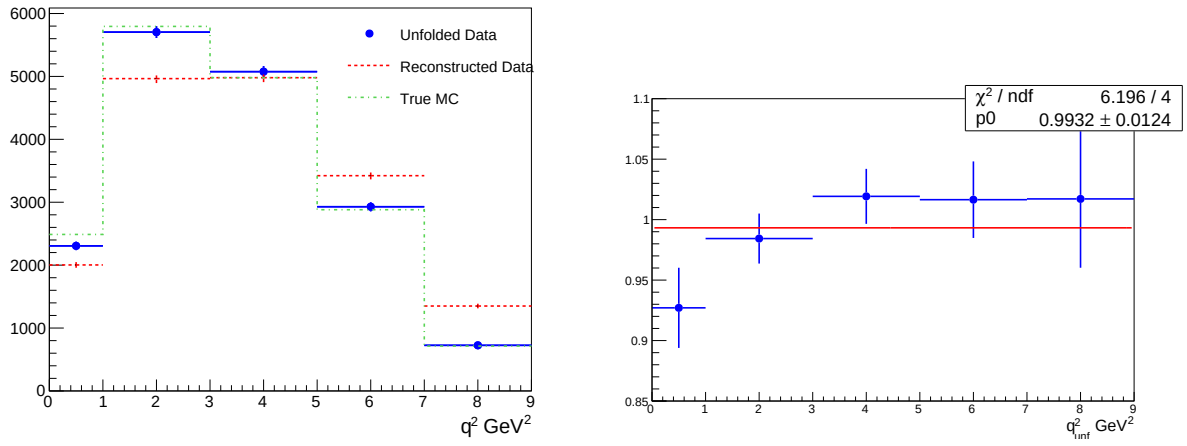

(a) (b)

Figure 6.16: The q^2 spectrum for MC $\Lambda_c^*\mu\bar{\nu}_\mu$: (red) distribution of the reconstructed q^2, (green) distribution of the true q^2, (black points) unfolded distribution. Here $k = 3$ is considered. The ratio between unfolded and true spectrum, is reported on the right.

6.8.1 The unfolded spectrum

The N_μ for $ISO < 0.25$ and $ISO \geq 0.25$ in each of the q^2 bins are summed together and the uncertainty propagated accounting for the small correlation

between the two bin in isolation. The distribution of the raw N_μ from the default fit are reported in figure 6.17 (red histogram). The first bin, $0 < q^2_{reco} < 1\ GeV$ includes all the $\Lambda_c^* \mu \bar{\nu}_\mu$ reconstructed in the wide range $-10 < q^2_{reco} < 1\ GeV$. In figure 6.17 it is also reported the unfolded distribution of the raw N_μ.

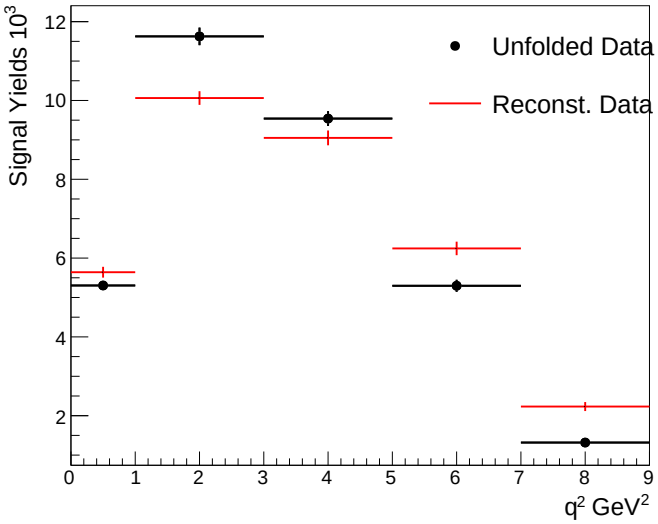

Figure 6.17: The q^2 spectrum for data $\Lambda_c^* \mu \bar{\nu}_\mu$ as obtained from the fit (red) and after the unfolding (black).

The unfolded spectrum has to be corrected for the signal efficiency in each q^2_{true} bin. The efficiency of the preselection as a function of the generated q^2_{true} is reported in Fig.6.18. The efficiency fall down at higher q^2, which is the region of zero-recoil: where the Λ_c^* is produced with small relative velocity in the Λ_b rest frame. As consequence at high q^2_{true}, the two pions emitted from the Λ_c^* decays have softer transverse momentum and are reconstructed with reduced efficiency. The efficiency of the trigger and signal selection, corrected for the PID and tracking, is shown in Fig.6.18. The selection efficiency is only slightly increasing with the q^2_{true}.

The efficiency corrected differential spectrum $d\Gamma(\Lambda_c^* \mu \bar{\nu}_\mu)/dq^2$, normalized to the total rate, is reported in table 6.9, together with the systematics uncertainties. It is shown in figure 6.19. The source of systematic uncertainties considered are the same reported in the previous section. The systematics associated with the unfolding procedure is given by the relative difference

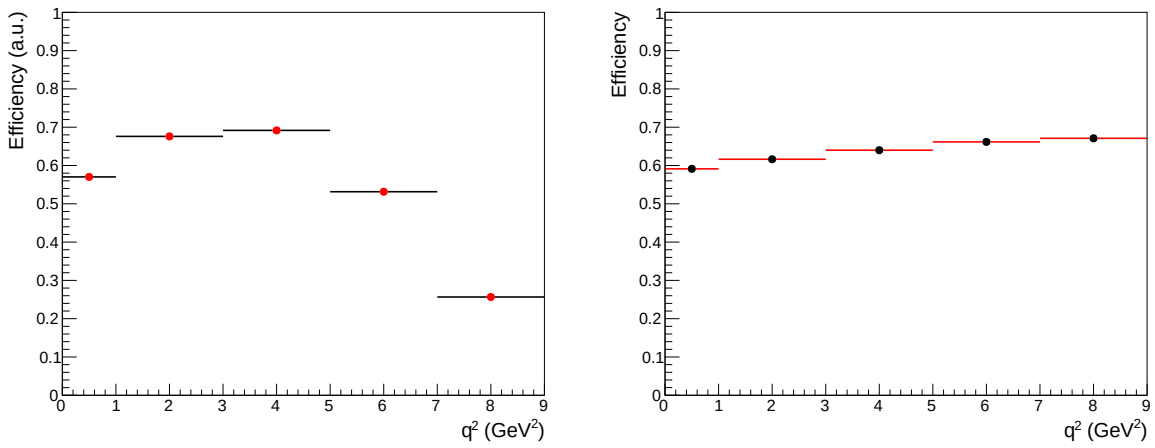

(a) (b)

Figure 6.18: Left: efficiency for the $\Lambda_c^*\mu\bar{\nu}_\mu$ signal preselection as a function of q^2_{true}. Right: efficiency of the signal selection, relative to the preselected events.

between the unfolded distribution with $k = 1$, and the true one. The statistical correlation coefficients for the unfolded vector, is reported in table 6.10.

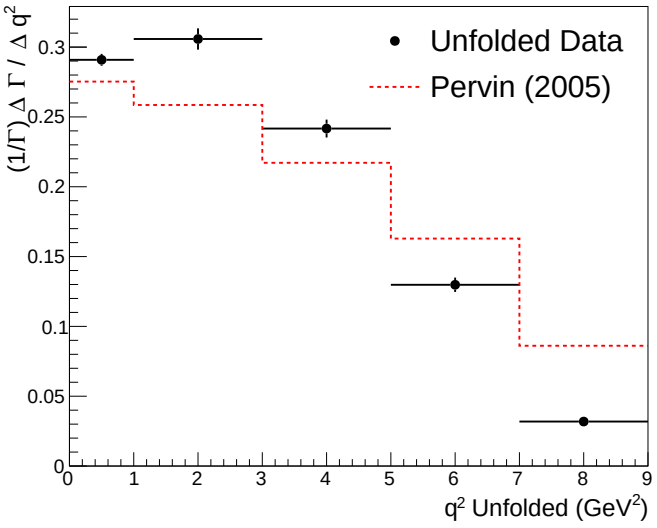

(a)

Figure 6.19: Efficiency corrected, differential $d\Gamma/dq^2$ spectrum for $\Lambda_c^*\mu\bar{\nu}_\mu$ decays, normalized to the total rate. On the same plot we reported also the spectrum predicted by the Pervin model [21]. Here we reported only the statistical uncertainties.

	$N_{\mu,1}$	$N_{\mu,2}$	$N_{\mu,3}$	$N_{\mu,4}$	$N_{\mu,5}$
$(1/\Gamma)d\Gamma/dq^2$	0.2912	0.3059	0.2415	0.1296	0.0318
σ_{stat}	0.0043	0.0076	0.0064	0.0051	0.0017
Systematics (%)					
MC statistics	0.05	0.01	0.04	0.06	0.07
PID corrections	0.09	0.04	0.05	0.14	0.20
Λ_c^* fake yields	1.6	0.5	1.2	1.9	2.2
Wrong-sign yields	0.03	0.01	0.02	0.04	0.05
Wrong-sign shape	0.15	0.04	0.10	0.20	0.25
double charmed composition	0.04	0.01	0.03	0.04	0.05
nSPD correction	0.29	0.17	0.14	0.58	0.88
Unfolding	2.1	1.0	0.9	2.2	3.2
Total Systematics	2.7	1.1	1.5	3.0	4.0

Table 6.9: Differential rate normalized to the total rate.

	$N_\mu, 1$	$N_\mu, 2$	$N_\mu, 3$	$N_\mu, 4$	$N_\mu, 5$
$N_\mu, 1$	1	0.946	0.467	0.008	-0139
$N_\mu, 2$		1	0.721	0.308	0.157
$N_\mu, 3$			1	0.873	0.780
$N_\mu, 4$				1	0.985
$N_\mu, 5$					1

Table 6.10: Correlations between the q^2 bins considered.

Chapter 7

Conclusion

This thesis reports the first measurement of the ratio

$$R(\Lambda_c^+(2625)) = \frac{\mathcal{B}(\Lambda_b^0 \to \Lambda_c^+(2625)\tau^-\bar{\nu}_\tau)}{\mathcal{B}(\Lambda_b^0 \to \Lambda_c^+(2625)\mu^-\bar{\nu}_\mu)}$$

where $\Lambda_c^+(2625) \to \Lambda_c^+(\to pK^-\pi^+)\pi^+\pi^-$ and $\tau^- \to \mu^-\bar{\nu}_\mu\nu_\tau$.
It is of great interest since there are new physics hints appearing as a consequence of flavour universality violation which can be probed using the R measurements. Several tests have been performed using the B mesons decays and many NP scenarios have been hypothesized to explain the found discrepancies with respect to SM predictions. The study of the analogue observables in the baryonic sector, characterized by different quarks and spin composition, is of great importance in order to confirm or disprove this highlighted discrepancy and to constrain the possible source.

The measurement presented in this thesis has been performed on proton-proton collision data at center-of-mass energies of 8 TeV collected by the LHCb detector during 2012, corresponding to an integrated luminosity of 2 fb^{-1}. The ratio is found to be

$$R(\Lambda_c^*) = 0.238 \pm 0.108(stat) \pm 0.058(syst)$$

It is only 2 sigma from zero, and it is consistent with the SM expectation based on the Pervin et al. model: $R_{exp}(\Lambda_c(2625)) = 0.151 \pm 0.014$. The statistical error dominates, but as shown in toys presented in chapter 6, assuming the same selection efficiency, and using the same fit strategy, with

the full data set available at the end of Run-II, it is expected a statistical error on R of 0.05, of the same order systematics uncertainties.

In this thesis a new approach has been implemented: the signal yields are extracted by fitting the output of a Neural Network built with the lepton energy, the missing mass square and the output of a Fisher discriminant that uses the Λ_b^0 vertex information. In order to increase the separation of the signal from the various source of backgrounds, the fit is performed simultaneously in five bins of q^2, and two bins in the isolation variable.

The $\Lambda_b \to \Lambda_c^* \mu \bar{\nu}_\mu$ yields extracted in bins of q^2 from the fit to the neural network, are used to determine the differential decay rate, $(1/\Gamma) d\Gamma/dq^2(\Lambda_b \to \Lambda_c^* \mu \bar{\nu}_\mu)$, considering the unfolding of the raw spectrum for the q^2 resolution and the selection efficiency. The shape appears different with respect the one extracted using the Pervin et al model [21]. A measurement of the Isgur-Wise slope may be done fitting this distribution.

Finally in chapter 3 of this thesis a new approach to estimate the momentum the b-hadron momentum in a semileptonic decays of this one at a hadron collider has been presented. In fact, in this environment, due to the presence of one or more neutrinos, to unknown parton-parton collision energy and the busy hadronic environment, is not possible to reconstruct the b-hadron momentum in the laboratory rest frame using final particles. As a consequence, the decays kinematics can be solved only up to a quadratic ambiguity. The method is based on a multivariate regression algorithm developed exploiting the informations that can be extracted by b-hadron flight vectors to infer its momentum and it is applied to the q^2 reconstruction in $\Lambda_b \to \Lambda_c^* \mu \bar{\nu}_\mu$. The algorithm described allows to improve the resolution in the determination of the decay kinematic variables for any semileptonic decays like $H_b \to H_c \mu \bar{\nu}_\mu$ or $H_b \to H_u \mu \bar{\nu}_\mu$. The improved resolutions may be exploited to measure the differential decay width $d\Gamma(H_b \to H \mu \bar{\nu}_\mu)/dq^2$ with good precision because of the reduced migrations between the q^2 bins.

Appendix A

Parameters of the fit to Δm LHCb 2012 data distributions in q^2 bins

Parameter	Fitted Value
$N_{\Lambda_c^+(2625)}$	6175 ± 231
$\Delta m_{\Lambda_c^+(2625)\_DG}$	341.72 ± 0.05
σ_1	1.86 ± 0.06
σ_2	5.99 ± 0.61
f_{2625}	0.66 ± 0.04
N_{comb}	25098 ± 351
α	-0.008 ± 0.002
p	2.08 ± 0.11
$N_{\Lambda_c^+(2595)}$	2183 ± 143
σ_L	3.05 ± 0.23
σ_R	11.00 ± 1.17
f_{2595}	4.02 ± 0.87

Parameter	Fitted Value
$N_{\Lambda_c^+(2625)}$	680 ± 62
$\Delta m_{\Lambda_c^+(2625)\_DG}$	341.97 ± 0.23
σ_1	2.32 ± 0.47
σ_2	4.19 ± 1.13
f_{2625}	0.54 ± 0.28
N_{comb}	6324 ± 116
α	-0.0049 ± 0.0005
p	1.83 ± 0.03
$N_{\Lambda_c^+(2595)}$	294 ± 45
σ_L	3.23 ± 0.45
σ_R	4.19 ± 1.13
f_{2595}	0.99 ± 0.61

Table A.1: $q^2 \in]-10, 1]$ $(GeV/c)^2$ - Parameters of the fit to Δm LHCb 2012 data distribution after applying the $\Lambda_b^0\_ISO\_BDT < 0.25$ (left), and $\Lambda_b^0\_ISO\_BDT \geq 0.25$ (right).

Parameter	Fitted Value
$N_{\Lambda_c^+(2625)}$	10421 ± 211
$\Delta m_{\Lambda_c^+(2625)\_DG}$	341.7 ± 0.03
σ_1	1.87 ± 0.05
σ_2	4.99 ± 0.18
f_{2625}	0.66 ± 0.03
N_{comb}	26532 ± 321
α	-0.162 ± 0.003
p	2.49 ± 0.16
$N_{\Lambda_c^+(2595)}$	5253 ± 168
σ_L	2.99 ± 0.14
σ_R	12.00 ± 0.24
f_{2595}	0.68 ± 0.03

Parameter	Fitted Value
$N_{\Lambda_c^+(2625)}$	1028 ± 103
$\Delta m_{\Lambda_c^+(2625)\_DG}$	341.68 ± 0.15
σ_1	2.15 ± 0.19
σ_2	5.99 ± 0.64
f_{2625}	0.81 ± 0.15
N_{comb}	10256 ± 172
α	-0.014 ± 0.002
p	2.04 ± 0.11
$N_{\Lambda_c^+(2595)}$	392 ± 61
σ_L	2.57 ± 0.36
σ_R	5.81 ± 1.07
f_{2595}	0.99 ± 0.63

Table A.2: $q^2 \in]1,3]$ $(GeV/c)^2$ - Parameters of the fit to Δm LHCb 2012 data distribution after applying the $\Lambda_b^0\_ISO\_BDT < 0.25$ (left), and $\Lambda_b^0\_ISO\_BDT \geq 0.25$ (right) .

Parameter	Fitted Value
$N_{\Lambda_c^+(2625)}$	9406 ± 205
$\Delta m_{\Lambda_c^+(2625)\_DG}$	341.67 ±0.04
σ_1	1.72 ± 0.14
σ_2	3.38 ± 0.39
f_{2625}	0.51 ±0.11
N_{comb}	34598 ± 386
α	-0.018 ± 0.002
p	2.32 ± 0.09
$N_{\Lambda_c^+(2595)}$	4656 ± 216
σ_L	1.76 ± 0.22
σ_R	10.99 ± 0.49
f_{2595}	0.75 ±0.04

Parameter	Fitted Value
$N_{\Lambda_c^+(2625)}$	1137 ± 118
$\Delta m_{\Lambda_c^+(2625)\_DG}$	341.40 ± 0.14
σ_1	2.21 ± 0.19
σ_2	5.96 ± 2.61
f_{2625}	0.82 ± 0.16
N_{comb}	12970 ± 198
α	-0.013 ± 0.002
p	1.96 ± 0.11
$N_{\Lambda_c^+(2595)}$	543 ± 74
σ_L	3.37 ± 0.51
σ_R	9.99 ±0.86
f_{2595}	0.79 ± 0.14

Table A.3: $q^2 \in]3,5]$ $(GeV/c)^2$ - Parameters of the fit to Δm LHCb 2012 data distribution after applying the $\Lambda_b^0\_ISO\_BDT < 0.25$ (left), and $\Lambda_b^0\_ISO\_BDT \geq 0.25$ (right) .

Parameter	Fitted Value
$PN_{\Lambda_c^+(2625)}$	6618±168
$\Delta m_{\Lambda_c^+(2625)\_DG}$	341.69 ± 0.04
σ_1	3.04 ± 0.26
σ_2	1.31 ± 0.17
f_{2625}	0.67 ± 0.09
N_{comb}	33910 ± 299
α	-0.017 ± 0.001
p	2.23 ± 0.91
$N_{\Lambda_c^+(2595)}$	3825 ± 182
σ_L	1.57 ±0.28
σ_R	11.00 ± 0.43
f_{2595}	0.76 ± 0.05

Parameter	Fitted Value
$N_{\Lambda_c^+(2625)}$	738± 80
$\Delta m_{\Lambda_c^+(2625)\_DG}$	341.78 ±0.19
σ_1	1.67 ± 0.93
σ_2	2.83 ± 1.24
f_{2625}	0.36 ± 0.66
N_{comb}	12913 ± 171
α	0.015 ±0.002
p	2.04 ± 0.10
$N_{\Lambda_c^+(2595)}$	519 ± 78
σ_L	2.99 ± 0.54
σ_R	9.99 ± 1.80
f_{2595}	0.80 ± 0.14

Table A.4: $q^2 \in]5,7]$ $(GeV/c)^2$ - Parameters of the fit to Δm LHCb 2012 data distribution after applying the $\Lambda_b^0\_ISO\_BDT < 0.25$ (left), and $\Lambda_b^0\_ISO\_BDT \geq 0.25$ (right) .

Parameter	Fitted Value
$N_{\Lambda_c^+(2625)}$	2380 ± 99
$\Delta m_{\Lambda_c^+(2625)\_DG}$	341.43 ±0.07
σ_1	1.02 ± 0.23
σ_2	2.67 ± 0.22
f_{2625}	0.24 ± 0.06
N_{comb}	18302 ± 214
α	-0.023 ±0.002
p	2.206 ± 0.098
$N_{\Lambda_c^+(2595)}$	1919 ± 123
σ_L	2.97 ± 0.39
σ_R	11.00 ± 3.83
f_{2595}	0.46 ± 0.08

Parameter	Fitted Value
$N_{\Lambda_c^+(2625)}$	380 ± 109
$\Delta m_{\Lambda_c^+(2625)\_DG}$	341.57 ± 0.25
σ_1	1.72 ± 0.27
σ_2	5.99 ± 3.99
f_{2625}	0.76 ± 0.31
N_{comb}	8150±246
α	-0.018 ±0.002
p	1.76 ±0.11
$N_{\Lambda_c^+(2595)}$	222 ± 143
σ_L	2.52 ± 0.86
σ_R	6.44 ± 6.24
f_{2595}	0.71 ± 0.85

Table A.5: $q^2 \in]7, 10]$ $(GeV/c)^2$ - Parameters of the fit to Δm LHCb 2012 data distribution after applying the $\Lambda_b^0\_ISO\_BDT < 0.25$ (left), and $\Lambda_b^0\_ISO\_BDT \geq 0.25$ (right) .

Appendix B

Parameters of the fit to Δm wrong sign sample distributions in q^2 bins

Parameter	Fitted Value
$N_{\Lambda_c^+(2625)}$	60 ± 17
N_{comb}	14748 ± 43
α	-0.007 ± 0.005
p	1.96 ± 0.28
$N_{\Lambda_c^+(2595)}$	2 ± 15

Parameter	Fitted Value
$N_{\Lambda_c^+(2625)}$	42 ± 13
N_{comb}	771 ± 31
α	-0.0005 ± 0.006
p	1.61 ± 0.35
$N_{\Lambda_c^+(2595)}$	18 ± 7

Table B.1: $q^2 \in]-10, 1]$ $(GeV/c)^2$ - Parameters of the fit to Δm LHCb 2012 data distribution after applying the $ISO < 0.25$ (left), and $ISO \geq 0.25$ (right).

Parameter	Fitted Value
$N_{\Lambda_c^+(2625)}$	8 ± 11
N_{comb}	77 ± 30
α	-0.016 ± 0.007
p	2.49 ± 0.45
$N_{\Lambda_c^+(2595)}$	0 ± 15

Parameter	Fitted Value
$N_{\Lambda_c^+(2625)}$	17 ± 10
N_{comb}	584 ± 27
α	-0.006 ± 0.007
p	1.61 ± 0.36
$N_{\Lambda_c^+(2595)}$	10 ± 7

Table B.2: $q^2 \in]1, 3]$ $(GeV/c)^2$ - Parameters of the fit to Δm LHCb 2012 data distribution after applying the $ISO < 0.25$ (left), and $ISO \geq 0.25$ (right) .

Parameter	Fitted Value
$N_{\Lambda_c^+(2625)}$	24 ± 13
N_{comb}	93 ± 33
α	-0.009 ± 0.006
p	1.91 ± 0.32
$N_{\Lambda_c^+(2595)}$	0 ± 5

Parameter	Fitted Value
$N_{\Lambda_c^+(2625)}$	246 ± 13
N_{comb}	835 ± 32
α	0.001 ± 0.006
p	1.41 ± 0.31
$N_{\Lambda_c^+(2595)}$	15 ± 8

Table B.3: $q^2 \in]3, 5]$ $(GeV/c)^2$ - Parameters of the fit to Δm LHCb 2012 data distribution after applying the $ISO < 0.25$ (left), and $ISO \geq 0.25$ (right .

Parameter	Fitted Value
$N_{\Lambda_c^+(2625)}$	26 ± 13
N_{comb}	1095 ± 36
α	0.002 ± 0.005
p	1.31 ± 0.25
$N_{\Lambda_c^+(2595)}$	3 ± 8

Parameter	Fitted Value
$N_{\Lambda_c^+(2625)}$	26 ± 15
N_{comb}	1440 ± 42
α	0.005 ± 0.005
p	1.80 ± 0.28
$N_{\Lambda_c^+(2595)}$	15 ± 10

Table B.4: $q^2 \in]5,7]$ $(GeV/c)^2$ - Parameters of the fit to Δm LHCb 2012 data distribution after applying the $ISO < 0.25$ (left), and $ISO \geq 0.25$ (right) .

Parameter	Fitted Value
$N_{\Lambda_c^+(2625)}$	23 ± 13
N_{comb}	974 ± 35
α	-0.023 ± 0.005
p	2.19 ± 0.29
$N_{\Lambda_c^+(2595)}$	3 ± 8

Parameter	Fitted Value
$N_{\Lambda_c^+(2625)}$	38± 17
N_{comb}	1795 ± 47
α	-0.015 ± 0.003
p	1.83 ± 0.20
$N_{\Lambda_c^+(2595)}$	6 ± 12

Table B.5: $q^2 \in]7,10]$ $(GeV/c)^2$ - Parameters of the fit to Δm LHCb 2012 data distribution after applying the $ISO < 0.25$ (left), and $ISO \geq 0.25$ (right) .

Bibliography

[1] C.S.Wu et al. Experimental test of parity conservation in beta decay. *Phys. Rev.Lett*, (105,1413-1415), 1957.

[2] P.W.Higgs. Broken symmetries and the masses of gauge bosons. *Phys. Rev.Lett*, (13,508-509), 1964.

[3] N.Cabibbo. Unitary symmetry and leptonic decays. *Phys.Rev.Lett*, (10,531-533), 1963.

[4] T. Maskawa M. Kobayashi. CP - violation in the renormalizable theory of weak interaction. *Progress of Theoretical Physics*, (49-2,652-657), 1973.

[5] L.Wolfenstein. Parametrisation of the kobayashi-maskawa matrix. *Phys.Rev.Lett.*, (51,1945), 1983.

[6] C.Patrignani et al. Particle data group. *Chin.Phys.C.*, (40,100001), 2016.

[7] L. Maiani S. L. Glashow, J. Iliopoulos. Weak interactions with lepton-hadron symmetry. *Phys.Rev.Lett*, (1285-12), 1970.

[8] Ulrich Haisch Rhorry Gauld, Florian Goertz. An explicit $Z\prime$ -boson explanation of the $B^+ \to K^*\mu^+\mu^-$ anomaly. *JHEP*, (69), 2014.

[9] LHCb collaboration. Test of lepton universality using $B^+ \to K^+\ell^+\ell^-$ decays. *Phys.Rev.Lett.*, (113,151601), 1998.

[10] BaBar collaboration. Measurement of branching fractions and rate asymmetries in the rare decays $b \to K^{(*)}\ell^+\ell^-$. *Phys.Rev.D*, (86,032012), 2012.

[11] BaBar collaboration. Measurement of the differential branching fraction and forward-backward asymmetry for $b \to K^{(*)}l^+l^-$. *Phys.Rev.Lett*, (86,032012), 2012.

[12] LHCb collaboration. Search for new physics with $b \to sl^+l^-$ decay at lhcb. *LHC seminar*, 2017.

[13] M. Tanaka. Charged higgs effects on exclusive semitauonic B decays. *Z.Phys.C*, (67,321), 1995.

[14] I.Nisandzic S.Fajfer, J.F.Kamenik. On the $B \to D^{(*)}\tau\overline{\nu}$ sensitivity to new physics. *Phys.Rev.D*, (85,094025), 2012.

[15] Babar collaboration. Evidence for an excess of $\overline{B} \to D^{(*)}\tau^-\overline{\nu}_\tau$ decays. *Phys.Rev.Lett*, (109,101802), 2012.

[16] Belle collaboration. Measurement of the branching ratio of $\overline{B} \to D^{(*)}\tau^-\overline{\nu}_\tau$ relative to $\overline{B} \to D^{(*)}\ell^-\overline{\nu}_\ell$ decays with hadronic tagging at belle. *Phys.Rev.D*, (92,072014), 2015.

[17] Belle collaboration. Measurement of the branching ratio of $\overline{B} \to D^{(*)}\tau^-\overline{\nu}_\tau$ relative to $\overline{B} \to D^{(*)}\ell^-\overline{\nu}_\ell$ decays with a semileptonic tagging at belle. *Phys.Rev.D*, (94,072007), 2016.

[18] Belle collaboration. Measurement of the τ lepton polarization and $R(D*)$ in the decay $\overline{B} \to D^{(*)}\tau^-\overline{\nu}_\tau$. *Phys.Rev.D*, (103,17181), 2009.

[19] Wise Isgur. Heavy quark symmetry. *Phys.Lett.B*, (237,527), 1990.

[20] M.Neubert. Heavy quark symmetry. *Phys.Rept*, (245,259-39), 1994.

[21] Capstick Pervin, Roberts. Semileptonic decays of heavy Λ baryon in a quark model. *CERN-LHCC*, (98-004), 1998.

[22] Capstick Isgur. Baryons in a relativized quark model with chromodynamics. *Phys.Lett.D*, (34,2890(9186)), 1986.

[23] William Detmold, Christoph Lehner, and Stefan Meinel. $\Lambda_b \to p\ell^-\overline{\nu}_\ell$. *Phys. Rev. D*, (92, 034503), 2015.

[24] LHCb collaboration. Lhcb technical proposal. *CERN-LHCC*, (-98-004), 1998.

[25] LHCb collaboration. Measurement of $\sigma(pp \to \bar{b}\ X)$ at $\sqrt{s} = 7TeV$ in the forward region. *Phys. Lett. B*, (694,209-216), 2010.

[26] LHCb collaboration. Lhcb velo: Technical design report. *CERN-LHCC*, (2001-0011), 2001.

[27] LHCb collaboration. Lhcb rich: Technical design report. *CERN-LHCC*, (2000-037), 2000.

[28] LHCb collaboration. Lhcb magnet: Technical design report. *CERN-LHCC*, (2000-007), 2000.

[29] LHCb collaboration. Lhcb inner tracker: Technical design report. *CERN-LHCC*, (2003-009), 2003.

[30] LHCb collaboration. Lhcb calorimeters: Technical design report. *CERN-LHCC*, (2000-0036), 2000.

[31] LHCb collaboration. Lhcb muon system: Technical design report. *CERN-LHCC*, (2005-0012), 2005.

[32] LHCb collaboration. Lhcb trigger system: Technical design report. *CERN-LHCC*, (2003-031), 2003.

[33] LHCb Collaboration. Lhcb detector performance. *International Journal of Modern Physics*, (A 30), 2015.

[34] LHCb collaboration. Muon triggers in the high level trigger of lhcb. *CERN-LHCC*, (2005-0012), 2005.

[35] SLD Collaboration. A measurement of R_b using a vertex mass tag. *Phys.Rev.Lett*, (80:660-665), 1997.

[36] A.Puig. The *LHC*b trigger in 2011 and 2012. *CERN-LHCb-PUB*, (046), 2014.

[37] P. Skands T. Sjostrand, S. Mrenna. Pythia 6.4 physics and manual. *JHEP*, (05-026), 2006.

[38] D. J. Lange. The *E*vt*G*en particle decay simulation package. *Nucl. Instrum. Meth.*, (A462 152), 2001.

[39] Geant4 collaboration. Geant4 developments and applications. *IEEE Trans. Nucl. Sci.*, (53-270), 2006.

[40] Anderlini et al. The pidcalib package. *CERN-LHCb-PUB*, (021), 2016.

[41] LHCb Collaboration. Measurement of the ratio of branching fractions $\mathcal{B}(\bar{B}^0 \to D^{*+}\tau^-\bar{\nu}_\tau)/\mathcal{B}(\bar{B}^0 \to D^{*+}\mu^-\bar{\nu}_\mu)$. *Phys.Rev.Lett*, (115-11-111803), 2015.

[42] LHCb Collaboration. Observation of mixing and measurement of mixing frequencies using semileptonic B decays. *Eur.Phys. J.C*, (73 2655), 2013.

[43] Sheldon Stone and Liming Zhang. Method of studying Λ_b^0 decays with one missing particle. *Adv. High Energy Phys.*, (931257), 2014.

[44] Lupato A. Rotondo M. Vesterinen M Ciezarek, G. Reconstruction of semileptonically decaying beauty hadrons produced in high energy pp collisions. *Journal of High Energy Physics*, (2,21), 2017.

[45] F. Pedregosa, G. Varoquaux, A. Gramfort, V. Michel, B. Thirion, O. Grisel, M. Blondel, P. Prettenhofer, R. Weiss, V. Dubourg, J. Vanderplas, A. Passos, D. Cournapeau, M. Brucher, M. Perrot, and E. Duchesnay. scikit-learn. *Journal of Machine Learning Research*, (2825-2830), 2011.

[46] Muriel Pivk and Francois R. Le Diberder. Splot: A statistical tool to unfold data distributions. *Nucl. Instrum. Meth.*, (A555), 2005.

[47] Andreas Hoecker, Peter Speckmayer, Joerg Stelzer, Jan Therhaag, Eckhard von Toerne, and Helge Voss. Tmva: Toolkit for multivariate data analysis. *PoS A CAT*, (040), 2007.

[48] R. A. Fisher. Use of mulitple measurements in taxonomic problems. *Annals of Eugenics*, (7-179-188), 1936.

[49] C.M.Bishop. Pattern recognition and machine learning. *Springer*, (9th edition), 2006.

[50] C. G. Broyden. The convergence of a class of double-rank minimization algorithms 1. general consideration. *IMA J Appl Math*, (6, 76-90), 1970.

[51] R.Fletcher. A new approach to variable metric algorithms. *The Computer Journal*, (13, 317-322), 1970.

[52] D.Goldfarb. A family of variable-metric methods derived by variational means. *Mathematics of Computation*, (24, 23-26), 1970.

[53] D.F.Shanno. Conditioning of quasi-newton methods for function minimization. *Mathematics of Computation*, (24, 647-656), 1970.

[54] Kyle Cranmer, George Lewis, Lorenzo Moneta, Akira Shibata, and Wouter Verkerke. Histfactory: A tool for creating statistical models for use with roofit and roostats. *CERN-OPEN-2012*, (016), 2012.

[55] Kyle S. Cranmer. Kernel estimation in high-energy physics. *Comput. Phys. Commun.*, (136, 198-207), 2001.

[56] R. Barlow and C. BEESTON. Fitting using finite monte-carlo samples. *Computer Physics Communications*, (77,19), 1993.

[57] A. Horn. On the singular values of a product of completely continuous operators. *Proc. Nat. Acad. Sci. USA*, (36:374–375), 1951.

Ringraziamenti

Desidero ringraziare di cuore il Dottor Marcello Rotondo per avermi guidata in questo percorso. Ringrazio per le tante cose che mi ha insegnato, per l'infinita disponibilità e la pazienza che ha avuto nel risolvere i miei dubbi.

Desidero poi ringraziare il Professor Gabriele Simi per la disponibilità, il prezioso sostegno e l'aiuto.

Ad entrambi, la mia riconoscenza per avere sempre dato credito alle mie idee.

Ringrazio poi l'intero gruppo di LHCb di Padova che mi ha sostenuto in questo stupendo percorso.
Lavorare con voi, è stato, ed è un onore per me.